

Towards combined x-ray and optical mammography

Benjamin David Price



Department of Medical Physics & Bioengineering

A thesis submitted to University College London for
the degree of Doctor of Philosophy

I, Benjamin David Price, confirm that the work presented in this thesis is my own. Where information has been derived from other sources, I confirm that this has been indicated in the thesis.

Signed.....

Abstract

Optical contrast, dependent upon haemodynamics and thus providing physiological information, is complementary to radiographic contrast. Combined x-ray and optical mammography screening could provide increased specificity over either system alone. Medical imaging equipment is routinely characterised and tested using tissue equivalent phantoms. A novel phantom material is presented: a solution of polyvinyl alcohol in ethanol and water freeze-thawed to produce a solid yet elastically compressible gel. The x-ray attenuation, mechanical and optical properties of these gels can be accurately adjusted over appropriate ranges so as to mimic cancerous or healthy breast tissues.

Modulated imaging in both optical and x-ray acquisitions is also considered. An x-ray system capable of optimising dose distribution has previously been developed at UCL. Overall images are obtained by aligning multiple images from smaller sensors. The effects that this type of acquisition has on spatial resolution are discussed. Two considerations are made: (i) is there a minimum size sensor whose modulation transfer function (MTF) can accurately be determined? (ii) does the MTF of an overall image differ significantly from those of its constituent images? The smaller a sensor becomes, the harder it is to determine its MTF accurately, and the resolution of overall images is slightly poorer than those of individual sensor images. Nonetheless these effects are small and should not hinder the development of such systems.

Whilst similar dose considerations do not apply to optical tomography, modulated imaging still presents potential benefits. A method of visualising intensity data in order to localise regions of heterogeneous absorption is presented using both simulated and experimental data. Objective functions designed to quantify the visibility of these heterogeneities are proposed and it is shown that optimal distributions of source power, that maximise these, can be found. It is proposed that such techniques might allow optical acquisitions to be performed more rapidly.

Table of contents

Abstract	3
List of figures	8
List of tables	11
List of abbreviations.....	12
Acknowledgements.....	13
Chapter One.....	14
The purpose and considerations of performing combined x-ray and optical mammography	
1.1. Chapter overview	14
1.2. Current status and limitations of x-ray mammography	14
1.3. Increasing the specificity of mammography	15
1.4. Possible adjuncts to x-ray mammography.....	16
1.5. Novelty and scope of this thesis	19
1.6. Advanced x-ray techniques	20
1.6.1. Summary of techniques.....	20
1.6.2. The I-Imas	21
1.7. Diffuse optical imaging of the breast	23
1.7.1. Principles of diffuse optical imaging	23
1.7.2. Possible approaches to acquisition.....	25
1.7.2.1. Time domain systems.....	25
1.7.2.2. Frequency domain systems	25
1.7.2.3. Continuous wave systems	26
1.7.2.4. Modulated imaging	27
1.7.3. Systems developed at UCL	29
1.7.3.1. MONSTIR.....	30
1.7.3.2. CW system	31
1.8. Combined optical and x-ray mammography	32
1.8.1. Current status	32
1.8.2. Specific considerations of combined systems	34

1.8.2.1. Tomography versus topography	34
1.8.2.2. Breast compression	36
1.8.2.3. Inter-modality image registration and compression modelling.....	37
1.8.2.4. Maximisation of optical contrast.....	38
1.9. X-ray and optical phantoms	40
1.10. Summary of thesis research.....	43
Chapter Two	44
Assessing the validity of modulation transfer function evaluation techniques with application to small area and scanned digital detectors	
2.1 Chapter Overview	45
2.2. Introduction.....	45
2.3. Method	48
2.3.1. Edge or slit?.....	48
2.3.2. Calculation of edge position and angle	49
2.3.3. Oversampling the ESF	50
2.3.4. Processing the ESF.....	50
2.3.5. Investigating the effect of sensor size and scanning	51
2.4. Results	53
2.4.1. Method of MTF determination.....	53
2.4.2. MTFs obtained	54
2.4.2.1. MTFs of separate sensors.....	54
2.4.2.2. Effect of sensor area.....	55
2.4.2.3. Effect of scanning	55
2.5. Discussion	56
2.5.1. Single over multi sampling	56
2.5.2. Variation between individual sensor MTFs	57
2.5.3. Effects of reducing sensor area and scanning	57
2.6. Conclusions	58
Chapter Three	60
Optimisation of illumination in diffuse optical imaging	
3.1. Chapter Overview	60
3.2. Introduction.....	61
3.2.1. Maximisation of distinguishability.....	64
3.3. Method	69
3.3.1. Choice and justification of novel objective functions	69
3.3.1.1. SNR based objective functions	71
3.3.1.2. CNR based objective functions	76

3.3.2. Finding optimal solutions of objective functions	77
3.3.3. Testing minimisation codes.....	78
3.3.4. Generating modelled data.....	79
3.3.5. Acquisition of experimental data	80
3.3.5.1. Design and manufacture of slab phantom/interface	80
3.3.5.1.1. Slab phantom.....	82
3.3.5.1.2. Interface plates	83
3.3.5.2. Data acquisition.....	84
3.3.5.3. Data processing	86
3.4. Results	89
3.4.1. Un-optimised simulated and experimental profiles.....	89
3.4.2. SNR_{equal}	92
3.4.3. CNR_{equal}	92
3.4.4. SNR_{max}	94
3.4.5. CNR_{max}	96
3.5. Discussion	98
3.6. Conclusions	100

Chapter Four 102

An elastically compressible phantom material with mechanical, x-ray attenuation and optical properties equivalent to breast tissue

4.1. Chapter overview	102
4.2. Introduction.....	103
4.3. X-ray, optical and mechanical properties of breast tissue	105
4.3.1. X-ray attenuation.....	105
4.3.2. Optical properties	105
4.3.3. Mechanical properties	106
4.3.4. Summary of required phantom properties.....	108
4.4. Method	109
4.4.1. Manufacture of gels.....	109
4.4.1.1. DMSO based gels.....	109
4.4.1.2. Ethanol based gels.....	110
4.4.2. Measurement of linear x-ray attenuation coefficient	111
4.4.3. Characterisation of optical properties.....	112
4.4.4. Mechanical testing.....	113
4.4.4.1. Effect of sample geometry and compression speed	114
4.4.4.2. Testing of pork tissue	114
4.4.4.3. Testing ethanol based gels of varying PVAL concentration	115
4.5. Results	116

4.5.1. Linear x-ray attenuation coefficients.....	116
4.5.2. Optical Properties.....	117
4.5.3. Mechanical testing.....	117
4.5.3.1. Effect of sample geometry and speed of compression	117
4.5.3.2. Pork tissue	119
4.5.3.3. Effect of PVAL concentration in ethanol based gels	119
4.6. Discussion	120
4.6.1. X-ray attenuation of gels	120
4.6.2. Optical properties	121
4.6.3. Mechanical measurements	121
4.6.3.1. Effects of sample dimensions and rate of compression	121
4.6.3.2. Pork tissue	122
4.6.3.3. PVAL gels.....	122
4.6.4. Summary of properties achieved.....	123
4.7. Conclusion.....	124
Chapter Five	125
Summary of key contributions and suggestions for further work	
5.1. Key contributions made to field.....	125
5.1.1. Investigating the effects of slot scanning on spatial resolution in radiography....	125
5.1.2. Optimisation of illumination in optical imaging	125
5.1.3. Development of a compressible dual-modality phantom material.....	126
5.2. Future work	126
Appendix One	129
Proof of percentage error minimisation	
Appendix Two.....	131
Generating N random integers whose sum is N	
Appendix Three	134
Production and characterisation of Pro-jet concentrate	
References	137

List of figures

Figure 1.1. Schematic of the I-Imas system developed at UCL. A low intensity scout image is acquired and the level of filtration utilised in the second, main, exposure adjusted accordingly.....	23
Figure 1.2. The absorption spectra of oxy and deoxyhaemoglobin in the wavelength range 650-1050 nm (Cope 1991)	24
Figure 1.3. Turbid media act as low pass filters. The amplitude of a low frequency modulation pattern is preserved for a longer time (and to greater depth) than that of a higher frequency.....	28
Figure 1.4. MONSTIR. As well as being used for breast imaging MONSTIR can be used to image the neonatal brain, as seen here on the neonatal unit.	30
Figure 1.5. The CW system developed at UCL. Note that this system is much smaller than MONSTIR and is readily portable.	31
Figure 1.6. The combined x-ray tomosynthesis and frequency domain imaging system developed at Massachusetts General Hospital	33
Figure 1.7. The CIRS tissue equivalent mammography phantom (Model 011A) is a typical x-ray mammography phantom	41
Figure 1.8. Examples of the solid resin optical phantoms that have been developed at UCL.....	42
Figure 2.1. The schematic of the I-Imas system developed at UCL (as originally shown in chapter one but reproduced here for the reader's benefit)	47
Figure 2.2. The way in which 14 individual images are stitched to create a larger image.	53
Figure 2.3. MTFs of the highest and lowest performance sensors as well as the mean MTF of all seven sensors.	54

Figure 2.4. MTFs obtained when sampling the ESF of a particular sensor from its full area and one sixteenth of this.	55
Figure 2.5. Average MTFs obtained from the individual images of a sensor and from larger, scanned, images acquired using the same sensor.....	56
Figure 3.1. a) The modelled slab geometry. The three absorbing inhomogeneity positions simulated are shown. b-d) The optimal source intensity distribution found in each case (central, left and right).....	68
Figure 3.2. Profile obtained simulating a 1 cm^2 absorbing region ($\mu_a = 0.015 \text{ mm}^{-1}$) central to the optode arrays. The background absorption of the slab is 3 times lower, 0.005 mm^{-1}	70
Figure 3.3. The slab phantom sandwiched between the two optode interfaces	81
Figure 3.4. The five positions that the absorbing region can assume relative to the source and detector optodes.....	81
Figure 3.5. The iterative process used to determine the appropriate optical density (OD) filter for each source to detector acquisition	85
Figure 3.6. a) An example of a TPSF with background noise. The average background noise of each TPSF was calculated over a region in the extreme tail (marked red) b) following subtraction the TPSF has a zero baseline.	87
Figure 3.7 a) Profile obtained simulating two 1 cm^2 decentralised heterogeneities of equal absorption ($\mu_a = 0.015 \text{ mm}^{-1}$). b) Profile obtained simulating two heterogeneities of differing absorption to one another. One to the left ($\mu_a = 0.015 \text{ mm}^{-1}$) and one to the right ($\mu_a = 0.03 \text{ mm}^{-1}$). The background absorption coefficient of the slab was taken to be 0.005 mm^{-1} in both simulations.....	90
Figure 3.8. a-e) The experimentally obtained profile obtained with the absorbing region in each of the five possible positions.....	91
Figure 3.9. An example of the result of optimisation using SNR_{equal}	93
Figure 3.10. A typical example of the result of optimisation using SNR_{max}	95
Figure 3.11. A typical example of the result of optimisation using CNR_{max}	97

Figure 3.12. Results shown pertain to experimental data acquired with the heterogeneity positioned to the far right (position R2 in figure 3.4). a) The optimal patterns found upon maximisation of SNR_{max} and CNR_{max} . b) The differences between the errors, at each detector, of the optimised profiles obtained using the two optimal patterns shown in a).	100
Figure 4.1. The Instron testing device with one of the gels positioned between the compression plates.	113
Figure 4.2. Linear x-ray attenuation coefficient increases with PVAL concentration...	116
Figure 4.3. Transport scatter coefficient of the initially non-scattering gels can be increased through the addition of titanium dioxide.....	117
Figure 4.4. Young's modulus shows some dependence on sample geometry	118
Figure 4.5. Four different samples of pork tissue demonstrate similar mechanical properties under compression.....	119
Figure 4.6. At a given strain Young's modulus increases with PVAL concentration ...	120
Figure A3.1. The dependence of absorption coefficient upon the concentration of Pro-jet suspension at 780, 800 and 815 nm	136

List of tables

Table 1.1. Widely utilised breast imaging modalities.....	17
Table 1.2. Comparison of the two optical imaging systems developed within the biomedical optics reseach laboratory at UCL.	29
Table 3.1. The source detector map for three sources and detectors as obtained from a reference measurement is a 3×3 matrix	71
Table 3.2. The scaling factors applied to the measured intensity values as calculated from mean power meter readings at each OD.....	88
Table 3.3. The % improvement in the value of SNR_{max} upon optimal illumination seen for each of the simulated and experimental profiles.....	94
Table 3.4. The % improvement in the value of CNR_{max} seen for each of the simulated and experimental profiles upon optimal illumination.....	96
Table 4.1. The desired properties of the phantom material.....	109
Table 4.2. The dimensions of the seven DMSO based 9% w/v PVAL gel samples.....	110
Table 4.3. The properties of the characterised PVAL gels in comparison with those originally desired.....	123

List of abbreviations

CMOS	Complementary Metal Oxide Semiconductor
CNR	Contrast to Noise Ratio
CW	Continuous Wave
ERF	Error Function
ESF	Edge Spread Function
I-IMAS	Intelligent Imaging System
LSF	Line Spread Function
MONSTIR	Multi-Channel Opto-electronic Near-Infrared System for Time-resolved Image Reconstruction
MTF	Modulation Transfer Function
OD	Optical Density
PMT	Photomultiplier Tube
PVAL	Polyvinyl Alcohol
SNR	Signal to Noise Ratio
TPSF	Temporal Point Spread Function
VOA	Variable Optical Attenuator

Acknowledgements

Without the ongoing support, patience and humour of my supervisors, Drs Adam Gibson and Gary Royle, this work would have been impossible. During times of difficulty and frustration I could always rely on them for the support I needed. Thank you very much.

Whilst working toward this thesis I have been surrounded by a team of colleagues and fantastic friends – thank you to you all. In particular I would like to thank Professors Jem Hebden and Robert Speller for all of their help, encouragement and advice. Drs Sandro Olivo and Jennifer Griffiths have also been an inspiration, encouraging me to the end. When in need Drs Jan Laufer and Ben Cox have also provided much needed advice and light-hearted discussion. Colin Esbrand, who recently finished his PhD, and Kate Ricketts have been good friends.

I also owe thanks to Joe Evans, of the implanted devices group, for his willing advice and workshop assistance. James Hales and Sandra Bond, from the Institute of Archaeology at UCL, have also been fantastic. On many occasions they have gone out of their way to provide me with numerous resources as well as invaluable advice.

Last, but certainly not least, I would like to thank both my family and girlfriend, Kate Russell-Hobbs. Without their constant love and support I could not have started such a task – let alone finish it!

Chapter One

The purpose and considerations of performing combined x-ray and optical mammography

1.1. Chapter overview

In this chapter the current status of x-ray mammography is reviewed and its inability to provide physiological information is identified as a limitation. Possible adjuncts to x-ray mammography capable of providing physiological information are discussed. Of these diffuse optical imaging is identified to be the most promising. At this point the work presented in this thesis, and its novelty, is outlined. After this the possible approaches to optical breast imaging are summarised and two systems developed at UCL are described in more detail. Following this, work which has already been performed involving combined x-ray and optical mammography is reviewed and some specific considerations of this approach are discussed. The phantoms which have been developed to test and evaluate optical and x-ray mammography systems are also summarised.

1.2. Current status and limitations of x-ray mammography

Female breast cancer is the most commonly diagnosed cancer within the UK: 44,400 cases were diagnosed in 2004, representing 31% of all female cancers (Westlake and Cooper 2008). One in nine women suffer from breast cancer in their lifetime (Phillips et al 1999). Since the publication of the Forrest report (Forrest 1986), and the subsequent implementation of the NHS Breast Screening Programme (NHSBSP), mammographic screening has become widespread both in the UK and abroad. In the 12 months from April 2007 just under 2 million women were screened by the NHSBSP, 16,449 cancers being detected (Patnick 2009). Unfortunately it is difficult to precisely evaluate the benefit of breast screening due to a number of biases (Reddy and Given-Wilson 2004). Nonetheless it is estimated that the early diagnosis of breast cancer, through screening, saves 1400 lives a year in England equating to a reduction in mortality from breast cancer

of 35% (Beral et al 2006). Similar Swedish programmes have been found to reduce mortality by up to 45% (Duffy et al 2002).

As with any screening technique a balance between sensitivity and specificity must be found. Findings from the Million Women Study suggest that the overall sensitivity and specificity of the NHSBSP are 86.6% and 96.8% respectively (Banks et al 2004). Both the sensitivity and specificity achieved depend upon many factors including the characteristics of the women screened (Banks et al 2004, Carney et al 2003) and the experience of the film readers (Esserman et al 2002). In the US, where mass screening is not performed, the difference in performance between radiologists has been compared (Beam et al 2003). The mean sensitivity and specificity was found to be 91 and 62% respectively. This increase in sensitivity and decrease in specificity is attributed to several factors. These include the lesser experience of the radiologists at interpreting mammograms (Beam et al 2003) as well as the different cultural approach towards litigation, US radiologists being cautious not to miss any cancers (Elmore et al 2005).

The fact that the sensitivity and specificity achieved in mammography is so variable remains its largest limitation. Increasing the specificity achieved would reduce the costs of identifying false positive screenings through further assessment or surgical biopsy (Burnside et al 2001). Even in the NHSBSP, which has a relatively high specificity, approximately 4% of screenings currently result in recall for follow up assessment (Patnick 2009). Only 1 in 5 of these recalls end with a diagnosis of cancer (Waldron 2010). An increased specificity would also reduce the number of patients subjected to unnecessary psychological distress whilst awaiting test results that eventually prove to be negative.

1.3. Increasing the specificity of mammography

Digital mammography is beginning to supersede film-screen systems, having demonstrated a number of advantages. These include the easier storage, transmission and viewing of mammograms as well as the elimination of film-processing costs. The NHSBSP plans to have replaced all film-screen systems with digital ones by 2012 (Department of Health 2007). The sensitivity and specificity of digital mammography is very similar to that of film-screen in the general screening population. Nonetheless it has demonstrated significantly better performance when imaging women with dense breast

tissue or those below 50 years of age (Pisano et al 2005). As the NHSBSP is lowering the age at which routine breast screening commences, from 50 to 47 (Department of Health 2007), the introduction of digital systems may be particularly relevant. In the future it is likely that advanced digital imaging techniques, that were not possible using film-screen systems, capable of further increasing specificity will emerge. These are discussed in more detail shortly (§1.6).

Despite any improvements afforded by digital imaging x-ray mammography will still suffer a fundamental limitation: it is unable to provide any physiological information about identified lesions. It is well established that the physiology, particularly blood volume and oxygenation, of malignant tumours is often different to that of benign abnormalities and healthy breast tissue. Performing x-ray mammography simultaneously with another imaging modality capable of providing physiological, as opposed to anatomical, contrast has the potential to improve the specificity of screening. Ideally images would be acquired simultaneously, with the breast held in an identical position, using both modalities. In this way the complexity of image registration problems would be reduced. If the adjunctive technique chosen could provide three dimensional images then this would be of additional benefit. X-ray mammograms represent the three dimensional anatomy of the breast in a two dimensional image. As such lesions are often obscured or overlaying healthy tissues can appear abnormal.

1.4. Possible adjuncts to x-ray mammography

A number of breast imaging modalities have become clinically established. These are summarised in table 1.1 along with optical tomography which currently remains a research technique. Both tomosynthesis and ultrasound provide depth resolution as well as being more capable of imaging dense breast tissues than standard mammography. Unfortunately they still lack physiological contrast and are unable to measure oxygenation levels. As well as providing three dimensional resolution and readily imaging dense breasts magnetic resonance imaging (MRI), positron emission tomography and optical tomography are all capable of providing physiological information.

Modality	Spatial resolution	Specific considerations
Standard x-ray mammography	At least 40 μm	<ul style="list-style-type: none"> • Gold standard for screening of general, asymptomatic population • Capable of detecting very fine detail – i.e. microcalcifications indicative of ductal carcinoma <i>in situ</i> • Mean glandular dose not in excess of 2.5 mGy per film (Cush et al 2006) • 2D representation of anatomy can obscure lesions • Of limited use imaging dense breast tissues
Ultrasound	~ millimetre	<ul style="list-style-type: none"> • Useful for imaging dense breast tissue and in follow up studies following x-ray mammography • Used to guide needle biopsy • Unable to detect microcalcifications
MRI	~ millimetre	<ul style="list-style-type: none"> • Useful for imaging dense breast tissue • Too expensive for use as a screening tool in general population • Particularly unpleasant for claustrophobic patients • Unable to detect microcalcifications
CT/tomosynthesis	~ 100 μm in plane ~ 1 mm vertical (Wu et al 2003)	<ul style="list-style-type: none"> • Performable at total doses similar to those of mammography (Niklason et al 1997) • Less compression required • Dedicated CT machines avoid exposure of the thoracic cavity and thus dose inefficiency (Boone et al 2001)
Scintimammography	2-3 millimetre (Scopinaro and Massa 2003)	<ul style="list-style-type: none"> • Cost, duration, relatively high dose and low sensitivity to small/deep tumours make this procedure unsuitable for general screening • Useful for evaluating axillary node involvement and multi focal disease • Whole body radiation dose ~3 mGy (Cutrone et al 1999) – too high for use in asymptomatic screening
Optical tomography	~ centimetre	<ul style="list-style-type: none"> • No radiation dose • Able to non-invasively determine oxygenation levels • Not yet commercially available but relatively cheap and portable

Table 1.1. Widely utilised breast imaging modalities.

Should cancer be diagnosed then any information gained about a tumour's level of oxygenation could have further clinical benefits. The level of oxygenation within a tumour is a significant prognostic indicator that can be an important consideration in treatment planning (Vaupel et al 2002). It is widely accepted that poorly oxygenated tumours often have a poor response to both radiotherapy (Wouters and Brown 1997) and chemotherapy (Harrison and Blackwell 2004). Hypoxic tumours also have a tendency to be more aggressive and malignant (Evans and Koch 2003). Over recent years these observations have driven a widespread interest in hypoxia imaging (Krohn et al 2008, Vaupel and Mayer 2007).

Blood oxygen level dependent MRI is sensitive to changes in blood oxygenation. Oxyhaemoglobin is diamagnetic and isomagnetic to surrounding tissue whilst deoxyhaemoglobin is paramagnetic. Consequently any reduction in the level of deoxyhaemoglobin causes the difference in magnetic susceptibility between the blood and surrounding tissues to reduce, leading to an increase in the T2* signal (Krohn et al 2008, McRobbie et al 2007). Unfortunately T2* is sensitive to changes in blood flow and volume as well as changes in oxygenation. As such only relative, rather than quantitative, measurements of blood oxygenation can be made. Furthermore the expense of MRI prevents its use in general screening. Nonetheless it is sometimes used to image younger women, whose breasts are typically denser, or those whose breasts contain scar tissue following surgery (Heywang-Kobrunner et al 1997). Aside from expense the large magnetic fields involved would make it very difficult to perform MRI simultaneously to x-ray mammography, thus preventing co-registration of the images.

Positron emission tomography has also been used to determine tissue oxygenation (Chapman et al 1998, Gupta et al 2002, Krohn et al 2008). Whilst a commonly used technique in patients that have already been diagnosed with cancer, the associated radiation dose, far greater than that of standard mammography (Cutrone et al 1999), precludes its use in the screening of an asymptomatic population. Other more invasive methods of measuring oxygenation using needle electrodes have also been considered (Evans and Koch 2003) but these are equally unattractive.

Optical tomography is unique in its ability to non-invasively visualise blood volume and oxygenation relatively cheaply and without potentially harmful radiation exposure (Hebden et al 2004). Though this currently remains a research technique breast tumours

have already been visualised successfully (Choe et al 2009, Enfield et al 2007). Furthermore optical tomography has been performed at the same time as x-ray mammography, aiding image registration (Zhang et al 2005). For these reasons optical tomography makes a promising adjunct to x-ray mammography at screening.

1.5. Novelty and scope of this thesis

This thesis presents three pieces of work concerning the assessment or improvement of image quality. Interest in performing combined x-ray and optical mammography is growing. As such both modalities, and their combination, are considered.

Firstly the effects of slot scanning on the overall spatial resolution of images was considered. Slot scanning systems rely upon a unique mode of acquisition in which a large overall image is obtained by aligning multiple images acquired by smaller sensors. This leads to two specific considerations. Firstly whether there is a minimum size sensor whose modulation transfer function (MTF) can accurately be determined and secondly whether the MTF of the large overall image differs from those of its constituents. Most studies to date have only considered the characterisation of digital plates with relatively large pixel arrays. For the purposes of this work the spatial resolution of a novel step and shoot x-ray imaging system developed within the radiation physics group at UCL, the I-Imas (Griffiths et al 2006, Schulerud et al 2007), was characterised. Nonetheless the considerations made and results found are not unique to the I-Imas but also applicable to other scanning systems.

Secondly methods of optimising optical acquisition, performed between two parallel plates as would occur in a dual-modality system, are discussed. Various constraints must be considered in the performance of such optical measurements (length of acquisition, instrumentation-based, etc). The feasibility of improving image quality, by optimising the distribution of light intensity between a fixed number of sources so as to overcome the restrictions of one or more of these constraints, was considered. The proof of concept work performed demonstrates that distributing the total source power in an optimal manner has the potential to increase the visibility of optical heterogeneities. Such techniques could allow acquisitions to be made more rapidly. If optical images are to be acquired under full mammographic compression then rapid acquisition will be essential.

Finally the development of a compressible phantom material with mechanical, x-ray and optical properties equivalent to breast tissue is described. Though many phantoms have been developed with x-ray or optical properties equivalent to breast tissue very few of these have possessed both simultaneously. The availability of such phantoms will be critical to the characterisation and evaluation of future dual-modality systems. Furthermore none of the phantoms developed to date has been realistically compressible. Such phantoms would be of use in the development of tissue deformation models as well as dynamic imaging techniques studying the time course of changes in blood flow and oxygenation during compression.

The rest of this chapter discusses the current literature concerning topics of relevance to the above areas of work.

1.6. Advanced x-ray techniques

1.6.1. Summary of techniques

In the future digital imaging could allow a number of advanced acquisition and image processing techniques to be used during screening that were not possible using film-screen systems. A few techniques that are not commonly used but could become so are

- Limited angle tomography. Standard mammography represents the three dimensional anatomy of the breast in a two dimensional image. As such lesions are often obscured or overlaying healthy tissues can appear abnormal. This problem is particularly prominent in women with dense breasts (Carney et al 2003). Limited angle tomography involves the acquisition of between 10 and 50 projection images over a small angular range (Wu et al 2003). These images are then used to reconstruct the appearance of different planes parallel to the detector. In this way the overlap of tissue and lesion obscurity can, to some degree, be overcome. As the individual images are acquired at a low dose the overall dose to the breast remains similar to that of single view mammography (Niklason et al 1997).

- Phase contrast imaging. Contrast observed in radiographs is attributable to the varying levels of attenuation within the sample imaged. In mammography the differences in attenuation, and therefore contrast, between different tissue types and regions are very subtle. Whilst passing through a sample the x-rays are not only partially absorbed but also refracted due to variations in refractive index between different regions. At low (mammographic) energies in the region of 15-25 keV this effect is much more pronounced than that of absorption (Olivo and Speller 2007). The visibility of boundaries between different regions of breast tissue can be enhanced by imaging these differences in refraction. Though phase contrast imaging currently remains a research technique it undoubtedly has a promising clinical future.
- Intelligent imaging. Modern digital mammography systems have automatic exposure control mechanisms to minimise patient dose and ensure optimal exposure. The required exposure can be calculated from measured parameters such as breast thickness or by determining the levels of attenuation present from an initial, low dose, acquisition. Either way the exposure level selected for the main acquisition is the same over the entire area of the image. Intelligent imaging extends this concept to vary the exposure used between different regions of the image. In this way the dose can be further reduced without a reduction in image quality (Schulerud et al 2007). A prototype intelligent imaging system, the I-Imas, has been developed within the radiation physics laboratories of UCL (Griffiths et al 2006, Schulerud et al 2007). As this system was used to investigate the effects of scanning on spatial resolution, as presented in this thesis, it is now described in more detail.

1.6.2. The I-Imas

This scanning system was built so that methods of intelligently distributing the dose used in radiography could be investigated. The radiation dose utilised in screening mammography should be minimised as much as possible. Whilst maximum allowable doses that must not be exceeded have been set (Cush et al 2006) significantly reduced doses remain ideal. This is reflected by the ALARA (as low as reasonably achievable) principle. The concept of the I-Imas is to obtain a low dose scout image and analyse this in order to determine an optimal distribution of exposure for the acquisition of a second, higher dose, image. During the second acquisition the exposure of different regions is

varied by means of moveable filters located between the source and object. In this way regions showing little or no variation in contrast are spared further dose whilst other more “interesting” regions are exposed more heavily.

A schematic diagram of the I-Imas is shown in figure 1.1. The system acquires overall images through the alignment of many smaller sensor images acquired as an object is stepped through adjacent positions, each step less than the width of a sensor. This mode of operation makes the system ideal for investigating the effects of scanning upon spatial resolution. The system consists of two columns of narrow scintillator coated CMOS active pixel sensors. Each sensor is 512 by 40 pixels in size, each pixel being 32 μm square. The sensors in the second row are each aligned with a moveable filter that lies between the source and object being imaged. Each filter varies in thickness in steps such that the x-ray beam can be attenuated by between 0 and 100% in 20% steps. Two separate images of the object are acquired one after the other. A low exposure is used in the first acquisition, the parameters of which are then used to determine the appropriate exposure, as modified by the dynamic filters, to be used in the second. Only areas of diagnostic interest identified in the original image need be fully exposed. It has been shown that the system can produce images with similar or improved diagnostic quality (contrast to noise ratio), at lower overall dose levels, to those typical of large area digital plates (Esbrand 2009, Griffiths et al 2008). In this proof of concept system the object was moved rather than the sensors but this would be reversed in a clinical system.

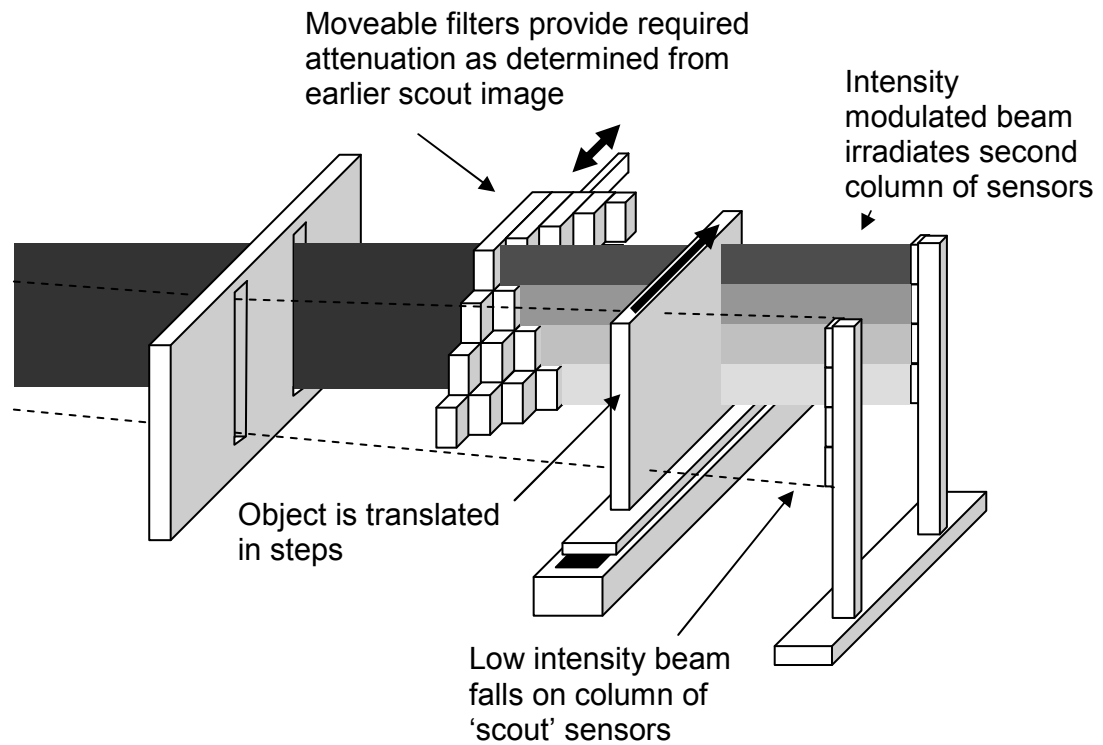


Figure 1.1. Schematic of the I-Mas system developed at UCL. A low intensity scout image is acquired and the level of filtration utilised in the second, main, exposure adjusted accordingly.

1.7. Diffuse optical imaging of the breast

1.7.1. Principles of diffuse optical imaging

Near infra-red light can penetrate several centimetres of tissue before being absorbed. Significant transmission thus occurs across relatively small volumes of tissue such as the female breast. Optical tomography relies upon the detection of these transmitted signals.

Oxy and deoxyhaemoglobin have significantly different absorptions in the near infra-red though they have an isosbestic point at approximately 800nm, at which their molar extinction coefficients are identical. Above this isosbestic point oxyhaemoglobin is the higher absorber whilst deoxyhaemoglobin is the more absorbing below (figure 1.2). Considering the relative transmission of two wavelengths of light allows not only the total quantity of haemoglobin present but also the relative quantities of oxy and deoxyhaemoglobin to be determined. In this way maps of absorption can be reconstructed and processed to provide three dimensional functional images of blood oxygenation and volume.

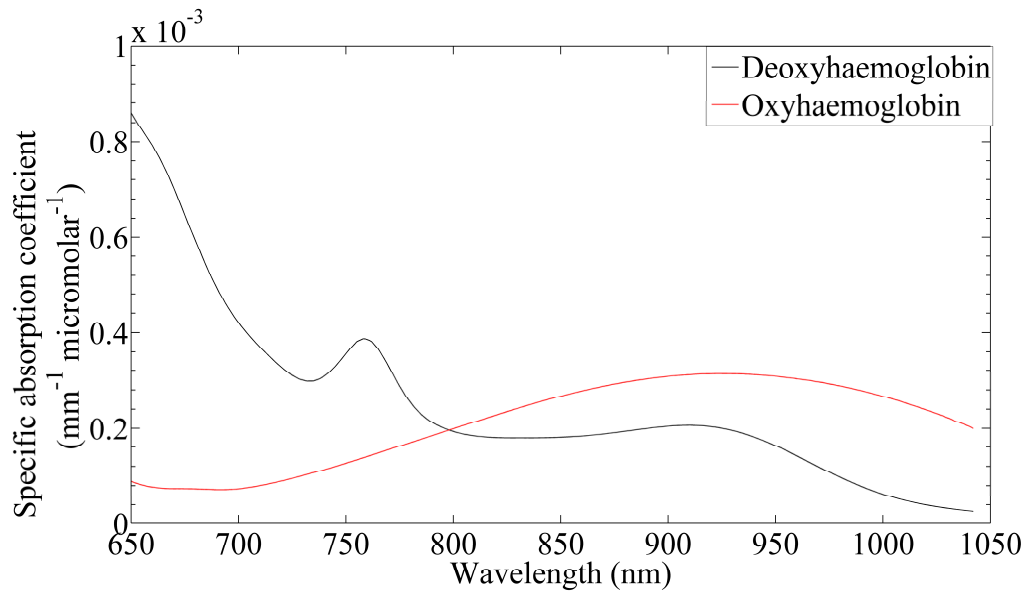


Figure 1.2. The absorption spectra of oxy and deoxyhaemoglobin in the wavelength range 650-1050 nm (Cope 1991)

Unfortunately the reconstruction of such images is challenging. The probing light is very highly scattered by the tissue through which it penetrates. As a result its path is very complex and impossible to accurately determine. This scattering is caused by the many small refractive index changes that occur at cell and organelle boundaries. This problem is reduced by illuminating the tissue at different points using a pulsed or intensity modulated light source and detecting the transmitted signals at a large number of positions. Measuring the time of flight of the detected photons allows the distance which they have travelled to be inferred. In this way their probabilistic route through the tissue can be determined. Even using this information the spatial resolution of optical tomography is still severely limited due to scatter.

Breast lesions may be significantly more or less scattering than the surrounding tissue. Fluid filled cysts, which present few refractive index changes, often appear as lower scattering regions (Enfield et al 2007). In addition tumour growth tends to be more chaotic and unstructured than that of surrounding healthy tissue. For this reason tumours also tend to scatter the light differently to their surrounding tissues. Whilst scattering is problematic in one respect it has been suggested that its variability between different tissues may be of benefit in the detection and differentiation of lesions (Pogue et al 2004).

1.7.2. Possible approaches to acquisition

Increased scattering causes a reduction in detected intensity. Because this causes light to travel a greater distance through the absorbing medium a greater proportion is absorbed. It is necessary to measure not only intensity but also time of flight in order to separately determine the absorption and scattering coefficients of a medium. Two types of system, time and frequency domain, can be utilised to acquire simultaneous measurements of intensity and time of flight. A third type of system, continuous wave, can be used to acquire solely intensity data. All three of these approaches, now described, rely upon measurements being made between large numbers of source and detector fibres. The way in which these source and detector fibres should be placed is discussed as a separate issue in §1.8.2.1.

1.7.2.1. Time domain systems

In these systems picosecond pulses of light are repeatedly emitted from each of a number of sources for a period of several seconds. The relative arrival times of individual photons are then recorded at a number of different detectors. Crucially only one source is activated at a time. In this way the origin of the light detected at each detector is known. Due to scattering the photons emitted during the picosecond pulse take different random paths. As a result those travelling to a given detector will arrive at different times with a distribution referred to as the temporal point spread function (TPSF). If light has passed through a significant thickness of tissue (several centimetres) then this distribution spreads over several nanoseconds. The total detected intensity and the mean time of flight can be calculated across each source detector pair from the measured TPSF.

1.7.2.2. Frequency domain systems

Instead of emitting discrete pulses of light these systems use sources that ‘continuously’ emit light whose amplitude is modulated at a high (few hundred MHz) frequency. As with time domain systems only one source is activated at a time. In these systems the relative phase shift and amplitude of the detected signal is measured at a number of detectors. In these systems it is the relative phase shift that allows the average time of flight between each source and detector to be calculated.

1.7.2.3. Continuous wave systems

A limitation of both time and frequency domain systems is that sources must be time multiplexed so that the source of detected light is known. The time taken to acquire a single image using a time domain system with a reasonable number of sources is typically several minutes (Gibson et al 2006). Whilst some very fast frequency domain systems have recently been developed a similar problem often faces these, even though the period of illumination of each source can be much reduced. Frequency domain systems with image acquisition times in the range of 160 ms (Franceschini et al 2000) to minutes (Nissilä et al 2006) have been reported. In general these relatively slow acquisition rates make it difficult, if not impossible, to perform real time functional imaging.

An alternative approach, generally used so that all sources can be illuminated simultaneously, is that of continuous wave (CW) imaging. In such CW systems all the sources continuously emit light but the intensity of each is modulated at a slightly different frequency to that of all the others. The range of modulation frequencies used is relatively low (typically a few kHz). The intensity of light reaching each detector is then rapidly sampled at intervals, typically by means of an avalanche photodiode. Through hardware demodulation (Yamashita et al 1999) or Fourier transformation (Everdell et al 2005) of the signal detected over a period of time the relative intensity contribution of each source, at each detector, can be determined. Because all of the sources can be illuminated simultaneously CW systems are capable of real time functional imaging with frame rates of up to 80 Hz reported (Everdell et al 2005).

CW systems have the further advantage that their relative simplicity leads to significant reductions in hardware costs relative to time and frequency domain systems. Unfortunately CW systems also have a major disadvantage. In these systems only intensity, no time of flight, information is acquired. This makes it impossible to establish separate values of absorption and scattering (Arridge and Lionheart 1998). Phase measurement techniques cannot be applied because the low frequency of modulations used are associated with too great a wavelength. The phase shift caused by scattering would be far too small to measure. In theory the sources could all be modulated at different, higher, frequencies but this would require the signal at each detector to be sampled very quickly. This has not been performed to date.

1.7.2.4. Modulated imaging

So far all the techniques described have relied upon the placement of a finite number of source and detector fibres upon the surface of the volume to be imaged. Recently an entirely different approach has been proposed – that of modulated imaging. Instead of using a finite number of sources a modified computer projector or digital micromirror device is used. This projects a continuous standing field, sinusoidally modulated in intensity, onto the surface of the volume to be imaged. The field of diffusely back-reflected or transmitted light is detected using a CCD camera.

This technique depends upon the fact that scattering media act as low pass filters (Bassi et al 2008). On propagation the modulation of low frequency patterns is preserved for longer periods of time, and thus to greater depths, than those of high frequency whose peaks and troughs are more readily blurred together by scattering (figure 1.3). This phenomenon allows the depth sensitivity of reflectance images to be varied by changing the spatial frequency of the projected illumination pattern used. This has been demonstrated experimentally by acquiring images of a turbid phantom containing absorbing inclusions buried at different depths (Cuccia et al 2005). This was imaged several times using a number of different modulation frequencies. In each case a phase demodulation technique was used to obtain an image of the ac modulated reflectance signal with the same frequency as the original illumination pattern. The images acquired at higher frequencies (~ 0.6 rad/mm) only showed the superficial heterogeneity on the surface. In contrast the image acquired with a flat field of illumination (0 rad/mm) showed both the superficial and deep heterogeneity.

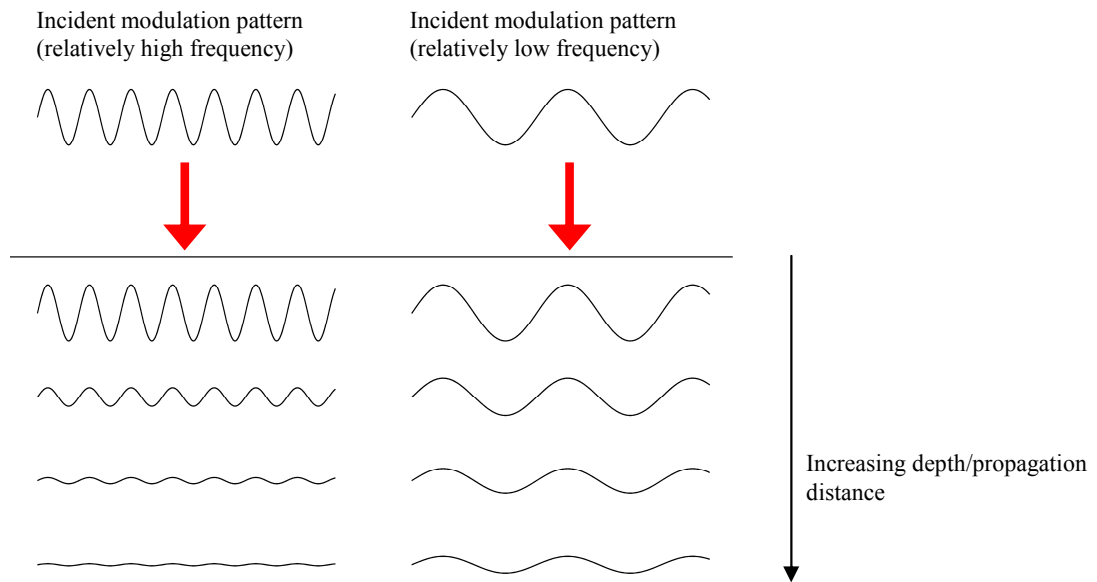


Figure 1.3. Turbid media act as low pass filters. The amplitude of a low frequency modulation pattern is preserved for a longer time (and to greater depth) than that of a higher frequency.

Modulated imaging can also be used to differentiate and separately map absorption and scattering coefficients in diffuse reflectance images (Abookasis et al 2009, Cuccia et al 2009). The size of the ac modulated reflectance signal is strongly dependent upon absorption coefficient at low frequencies of modulation but very little at higher frequencies (the signal at higher frequencies is quickly lost through scattering even if not absorbed). In contrast the change in reflectance signal seen with changes in the transport scatter coefficient is relatively constant over all frequencies. As a result the acquisition and comparison of two images acquired using different modulation frequencies (one high and one low) allows the coefficients to be found through the use of a pre-determined look-up table.

In the transmission geometry it has been demonstrated, both theoretically and experimentally, that the contrast and resolution of images increases the higher the frequency of spatial modulation used (Bassi et al 2009). As the size of the ac modulated signal transmitted reduces with increasing frequency a balance must be met; a high enough frequency used that the contrast and resolution are improved but low enough that a significant modulated component is still transmitted. It has also been shown that the phase of the modulation pattern is altered by the presence of inhomogeneities, presenting a zero crossing at the location of their centre (Bassi et al 2009, D'Andrea et al 2009). Detecting such changes in phase might allow the position of heterogeneities to be more accurately determined.

1.7.3. Systems developed at UCL

Over the past ten years two diffuse optical imaging systems have been developed within the biomedical optics research laboratory at UCL. Table 1.2 compares their most important features. MONSTIR (the Multi-channel Opto-electronic Near-infrared System for Time-resolved Image Reconstruction) is a time domain system (Schmidt et al 2000) whilst the other is a CW system (Everdell et al 2005). The important features of these systems are now described.

	MONSTIR	CW system
Domain	Time domain	Continuous wave
Wavelengths used	780 and 815 nm	670 and 850 nm
Power of each source	15 mW	2 mW
Detector type	Photomultiplier tube	Avalanche photodiode
Number of sources and detectors	32 (dual wavelength) sources and detectors	Up to 16 (dual wavelength) sources and 16 detectors simultaneously utilised
Temporal resolution	> 3 minutes/image	20 images/second with 16 detectors down to 40 images/second with just 4 detectors
Absorption and scattering coefficients separable?	Yes	No
Maximum transmission depth through which signal detectable	~ 10 cm	~ 5 cm
Approximate size of system (volume)	~ 2 m ³	~ 0.2 m ³

Table 1.2. Comparison of the two optical imaging systems developed within the biomedical optics research laboratory at UCL.

1.7.3.1. MONSTIR

MONSTIR is a time domain system (§1.7.2.1) and is pictured in figure 1.4. The system has 32 ‘optodes’, each consisting of a central source fibre surrounded by a larger detector fibre bundle, that are positioned over the surface to be imaged. Picosecond pulses of light are sequentially coupled into one of the 32 source fibres whilst the light reaching the other 31 optodes is detected. Determining the TPSF at each detector is not entirely straightforward. The arrival time of individual photons must be recorded one by one using a time correlated single photon counting detector. This is achieved by coupling each detector fibre to the photocathode of a highly sensitive photomultiplier tube (PMT). After the detection of a photon the PMT has a dead time during which it will be insensitive to the arrival of further photons. In order to collect an undistorted TPSF it is necessary to ensure that the probability of a single photon arriving at a given detector, from a particular source pulse, is significantly less than one. The method by which this is achieved is discussed in a moment. By repeatedly emitting picosecond pulses of light from each source over a period of several seconds, and detecting a single photon at each detector from a number of these pulses, a histogram of photon flight times (the TPSF) can be built up.



Figure 1.4. MONSTIR. As well as being used for breast imaging MONSTIR can be used to image the neonatal brain, as seen here on the neonatal unit.

The dynamic range of intensities incident on the detectors is typically very large, detectors close to a given source being exposed to orders of magnitude more light than those further away. In order to avoid damage to the PMTs, and ensure that the probability of photon detection from a given pulse is significantly less than one, it is necessary to introduce an appropriate level of attenuation between each optode and its PMT. This is achieved by means of a variable optical attenuator (VOA). Each VOA consists of a number of variably sized pinhole apertures mounted on a stepper motor. As different sources are sequentially illuminated the appropriate level of attenuation can be selected at each detector, for that source.

It is important to note that MONSTIR acquires data at two wavelengths (780 and 815 nm) so that both blood volume and oxygenation can be determined (§1.7.1). Whilst ‘on’ each source emits pulses of light at alternating wavelengths and two TPSFs are built up at each detector, one per wavelength.

1.7.3.2. CW system

This system, pictured in figure 1.5, currently operates with 16 source and up to 16 detector fibres. Each source fibre simultaneously emits two wavelengths of light with different frequencies of intensity modulation to one another, and those of all the other sources, within the frequency range 2 to 4 kHz. The frame rate obtainable is inversely proportional to the number of detectors used. The slowest acquisition rate, when using all 16 detectors, is 20 frames/second.



Figure 1.5. The CW system developed at UCL. Note that this system is much smaller than MONSTIR and is readily portable.

1.8. Combined optical and x-ray mammography

1.8.1. Current status

Over a decade ago optical and x-ray mammograms, though acquired at different times and probably under different levels of compression, were compared with one another (Franceschini et al 1997). The breasts imaged were compressed between two transparent plastic plates, a single source fibre positioned on one side and a detector fibre the other, such that transmission measurements could be made. The optical images were acquired by raster scanning these two fibres in tandem with one another, a frequency domain (FD) measurement acquired at each position. The contrast of these images was enhanced using an edge effect correction algorithm. This attempted to account for the varying thicknesses of breast tissue toward the edges of the image, estimating these from the measured change in phase at each position. Despite the relatively simplistic nature of the measurements lesions identified within the x-ray mammograms could also be identified in the optical images. This major step beyond simple illumination, facilitated by technological developments, helped to revive interest in optical mammography. Whilst a huge body of work concerning diffuse optical imaging has been performed over the last decade only one research group has developed a system designed to acquire co-registered optical and x-ray images of the breast – that of Boas based at Massachusetts General Hospital.

Initially this group demonstrated, using simulated data, that it was possible to improve the resolution and contrast of reconstructed optical tomography images using spatial priors as might be obtained from x-ray tomograms (Li et al 2003). The approach used was novel as it assumed correlation between the contrasts of the two modalities. As such, an area of contrast in the x-ray image was taken to indicate an increased probability of contrast occurring within the same area of the reconstructed optical image. Others have used anatomical priors (typically from MRI) to define boundaries between different tissue types, for example glandular and adipose. Li argues that such approaches tend to force the reconstruction of contrast at these boundaries too heavily. The study concludes by presenting experimentally acquired images of one breast containing an invasive carcinoma. Images reconstructed both with and without spatial priors, from x-ray tomosynthesis, were presented. The benefit of the prior was clear.

Since this work the group has published several papers detailing the results of pilot studies using a combined x-ray and optical mammography system (Zhang et al 2005). This is an x-ray tomosynthesis system whose compression plates have been modified (figure 1.6). An array of 40 optical source fibres can quickly be attached to one plate whilst an array of 9 detector fibres attaches to the other. These arrays are fixed in a known position and can be attached and removed without the position of the compression plates being disturbed. Following breast compression the system acquires frequency domain data at two wavelengths, 785 and 830 nm, within 60 seconds. The optical interfaces are then removed, without altering the compression or position of the breast, and the x-ray images are acquired. The entire sequence takes approximately 90 seconds. In this study the x-ray images were only used to define the outer boundary of the breast in the optical reconstruction, not to segment it into different regions or utilise the internal contrast information as before. 18 patients with suspicious lesions were imaged prior to biopsy. Whilst some of the lesions imaged were too small to detect in the optical images (typically microcalcification clusters < 1 mm in diameter) results were encouraging, tumours slightly less than 1cm in diameter being detected. Nonetheless it was concluded that further work to improve the reconstructed images was needed. Many of the lesions seen were misplaced by a couple of centimetres in the optical image and artefacts were common.

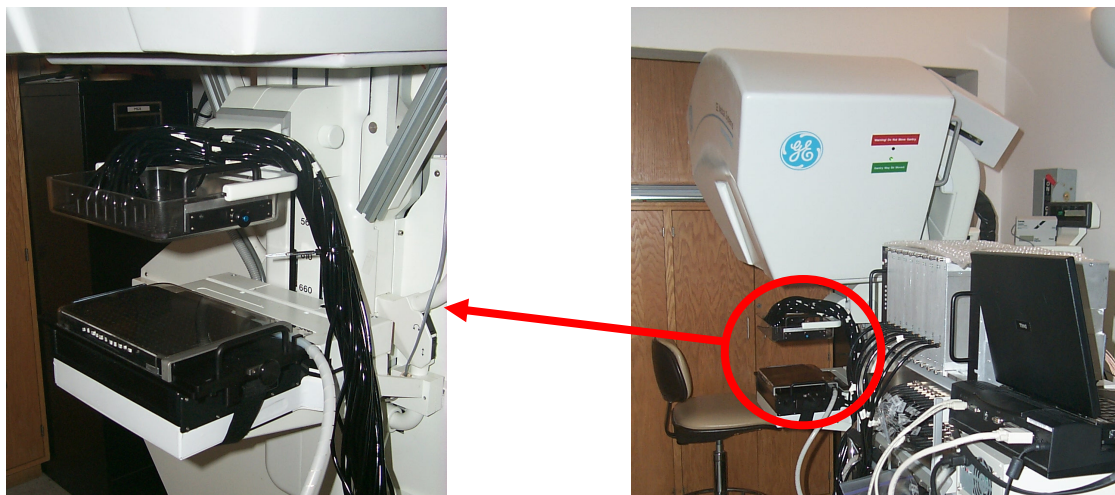


Figure 1.6. The combined x-ray tomosynthesis and frequency domain imaging system developed at Massachusetts General Hospital (images courtesy of Q Zhang).

In a more recent embodiment the system was modified to acquire both CW and FD measurements simultaneously (Fang et al 2008). The original FD system remains (though the 785 nm source is replaced with one at 685 nm) but two CW systems are also introduced. The first consists of 26 frequency encoded sources (13 at 685 nm and 13 at 830 nm). A second system operates at 3 wavelengths (685, 810 and 830 nm). In this instance the encoding allows the signal from each of the wavelengths to be separated rather than the source locations. The 3 wavelengths are time-multiplexed between 28 source locations. 32 avalanche photodiodes are introduced to detect the signals from these CW sources. It is hoped that the increased spatial sampling achieved by these systems may improve the resolution of reconstructed images. Since its development this system has been used to acquire images of 63 healthy breasts (Fang et al 2009). Each of these were classified according to their fibroglandular fraction (fraction of entire volume that is fibroglandular tissue) as determined from the x-ray tomogram. In this way the average concentration of haemoglobin, and its oxygen saturation, in breasts with different fibroglandular fractions were reported. As might be expected breasts containing more fibroglandular tissue contained a higher concentration of haemoglobin but this was less oxygenated (as fibroglandular tissue is more metabolically active than adipose). In a continuation of this study 97 subjects were imaged (51 healthy, 23 malignant tumours, 15 solid benign and 8 cysts). The different types of tissue and pathologies were segmented within each breast and the concentration of haemoglobin and oxygen saturation within each of these areas determined. In each case these were normalised relative to that measured in a region of adipose tissue to remove inter-subject variability. Significant differences in haemoglobin concentration were found between many different tissue types and pathologies but most importantly between the 23 malignant and 15 benign lesions. This is the strongest evidence to date that optical tomography has the potential to increase the specificity of screening mammography.

1.8.2. Specific considerations of combined systems

1.8.2.1. Tomography versus topography

The terms optical ‘topography’ and ‘tomography’ are often used interchangeably in the literature. In this thesis optical topography is taken to differ from tomography in that light diffusely reflected by a volume of tissue, rather than that transmitted through the volume, is detected. Topography is achieved by positioning all of a system’s source and

detector optodes in close proximity to one another on the same side of the object to be imaged (remission geometry). In contrast, tomography requires source and detector optodes to be placed on opposite sides of the volume so that transmission measurements can be made (transmission geometry).

The remission geometry is unable to provide sufficient depth information for full three dimensional reconstruction. Nonetheless it has been used successfully in the measurement of breast optical properties (Cerussi et al 2001, Suzuki et al 1996). An advantage of this geometry is that the intensities detected are much larger than those in the transmission geometry where sources and detectors are typically much further apart. CW systems are often used in the remission geometry as their main purpose is to maximise acquisition speed. If a large signal is incident on the detectors then this avoids the need to sample for a long period of time to obtain a reasonable signal to noise ratio in each frame. Topography is better suited to the measurement of fast haemodynamic responses close to the surface such as those of the outer cortex in the neonatal brain (Isobe et al 2001).

In order for a full three dimensional reconstruction of a breast's optical properties to be performed it is necessary to perform optical tomography using either a time or frequency domain system. This has been performed on both uncompressed and compressed breasts. In the uncompressed case optodes have been built into either annular structures (McBride et al 1999, Yates et al 2005) or cups (Enfield et al 2007). One group has developed a system incorporating two cups such that simultaneous measurements can be made on both breasts and compared (Schmitz et al 2005). Initial trials using the system show that comparing these measurements might help to highlight the presence of cancer in one of the two breasts. In the compressed geometry the breast is held between two parallel plates, the source and detector optodes positioned on the outer surfaces of these. This geometry was used in Boas' combined system, the source fibres placed on one plate and the detector fibres on the other (§1.8.1). In the work presented in this thesis it is assumed that the compressed geometry would be used so as to maintain a constant, or at least similar, breast positioning between the two modes of acquisition. In this way the registration and comparison of the x-ray and optical image data would be as straightforward as possible.

It is of note that more primitive transmission measurements can be made, in the compressed geometry, by positioning one source and one detector on opposite sides of the breast and scanning these in a rectilinear path. This cannot provide sufficient data for three dimensional reconstructions. Nonetheless such systems have been used to establish the optical properties of breast tissue (Grosenick et al 2003, Grosenick et al 1999) and successfully identify tumours and cysts (Taroni et al 2005).

1.8.2.2. Breast compression

During x-ray mammography the breast is held under compression. This reduces the breast thickness to lower the radiation dose received whilst increasing contrast and bringing lesions closer to the detector to increase their definition. Compression also minimises motion artefacts and ensures that the breast is of constant thickness in all but the peripheries of the image, leading to an even background film density.

Whilst breast compression is clearly essential it can cause some women pain. The percentage of women reported to experience discomfort during mammography varies between studies but this can be as high as 35% (Miller et al 2008). Certainly unnecessarily high compression should be avoided. At this point the pain experienced is increased with no gain in image quality (Poulos et al 2003). It has been found that the experience of discomfort can deter women from attending further screenings (Elwood et al 1998). There is some evidence that compressive stress may cause the collapse of blood vessels within tumours and the resultant formation of hypoxic regions (Sarntinoranont et al 2003). As hypoxic regions are less responsive to radiotherapy and chemotherapy such compression could potentially worsen prognosis. Overall it is clear that a balance must be sought in determining the level of compression applied. The maximum compression force allowed within the NHSBSP is 200 N (Lawinski and Dunne 2003).

Optical mammography, in contrast to x-ray mammography, does not require breast compression and a variety of breast and source detector geometries have been investigated (§1.8.2.1). Applying some compression can be beneficial. This reduces the thickness of tissue and decreases the acquisition time required as fewer photons are attenuated and a significant signal is collected in a shorter time. In a combined x-ray and optical system the breast would ideally be held under the same level of compression throughout both acquisitions. In this way image registration would be as straightforward

as possible. Currently a typical optical acquisition takes approximately one minute (Zhang et al 2005). Unfortunately compressing the breast as firmly as in x-ray mammography for this length of time would be unacceptable during routine screening. Unless acquisition time could be reduced significantly the level of compression would have to be partially released following the x-ray mammogram and prior to the longer optical acquisition. In this way the x-ray and optical images would at least be made with the breast held in positions as similar as possible. A balance between compression level and acquisition length must be sought. In this thesis it is proposed that methods of optimising the optical acquisition, allowing it to be performed more quickly, should be found. In this way it should be possible to acquire an optical image under full mammographic compression.

1.8.2.3. Inter-modality image registration and compression modelling

The ability to compare different images, both inter and intra-modality, has clear diagnostic benefits in breast imaging and many different image registration techniques have been proposed (Guo et al 2006). Though work has been done to allow the registration, and thus comparison, of x-ray mammograms acquired at different times and levels of compression (Hipwell et al 2007) the problems presented by combined x-ray and optical mammography are much more complex. Not only is it possible that some systems might acquire the images at different levels of compression but the observed contrast in each is dependent upon different parameters. Furthermore optical images acquired are typically three dimensional whilst x-ray mammograms are only two.

The modelling of breast compression has previously been considered with application to magnetic resonance (MR) images. The observation of lesions in such images, acquired without compression, can result in needle biopsy which is performed under compression. Attempts to warp MR images of the uncompressed breast to those that might be expected if the breast had been compressed, in order to aid tumour localisation during biopsy, have been made (Azar et al 2002). Similar models have been developed to warp MR (Pathmanathan et al 2004, Ruiter et al 2006) and CT (Kellner et al 2007) images to those expected at mammographic compression so as to allow better comparison with x-ray mammograms. Many of these models require segmentation of the images into different tissue types, each of which are assumed to have characteristic mechanical properties. Methods of measuring the elastic properties of tissue are advancing (Greenleaf et al 2003)

and further work in this field may prove beneficial to the performance of deformation models. Though much work remains there is no reason that these or similar methods should not be applied to the registration of optical and x-ray images.

1.8.2.4. Maximisation of optical contrast

It has been suggested that acquiring dynamic optical images of the breast as compression is applied and released may aid the detection of cancerous regions by increasing their contrast (Carp et al 2006). This would be particularly easy to implement in a combined x-ray and optical system in which mammographic compression must be applied and released anyway. This approach was first proposed when a spectroscopic study of 5 asymptomatic volunteers showed that the blood volume and oxygenation of the breast both increased by approximately 10% upon application of very gentle and prolonged compression (Jiang et al 2003b). This was attributed to tissue relaxation and the compression triggering a vasodilatory response, increasing blood volume and oxygenation within the tissue. Furthermore the size of the response was found to be larger in patients with a low body mass index. This suggests that the changes seen depend upon tissue composition, being larger in primarily fibroglandular (blood and water containing) as opposed to fatty tissues. As cancerous tissue is often stiffer and less compressible than healthy tissue (Wellman et al 1999), as well as having a significantly different metabolism, it seems likely that imaging changes in blood volume and oxygenation during compression could increase the contrast of such regions.

Since this initial study the same group have published the results of a slightly larger study of 17 asymptomatic volunteers (Jiang et al 2010, Jiang et al 2009). The system used was very similar to that used in the previous study but a much firmer compression was generally applied. The breast was compressed by a ring of source and detector fibres that were gradually brought closer together to reduce the diameter of the pendulant breast. Interestingly the results of this study were significantly different from that originally performed. On this occasion the blood volume was seen to decrease (as opposed to increase) upon compression whilst the level of oxygenation was not seen to change significantly. At higher levels of compression it appears that any increase in blood volume due to vasodilation is overwhelmed by the reduction in volume caused by the compression forcing blood out of the breast.

An even larger study of 56 healthy volunteers has been performed by Boas' group (Carp et al 2006). This study has two significant differences to those of Jiang. Firstly compression was applied between two parallel plates. As such it is much easier to compare the level of compression applied to that typical of mammography. Though the compression applied was reported in pounds these values were converted to the nearest Newton for the sake of this discussion, 1 lb taken to exert a downward force of 4.45 N. Secondly Boas' system used a single source fibre and acquired remission measurements as opposed to using multiple source fibres and a transmission geometry. As a result the temporal resolution of the system was much better (80 ms as opposed to 15 s) but image reconstruction could not be performed, only bulk properties being determined. For each volunteer baseline optical properties were acquired before the application of a 13 N compression force. Optical properties were then recorded for 30 seconds before this was increased to 27 N and recordings taken for a further 30 seconds. After this compression was either increased to 53 N (and optical properties recorded) or released. With 27 N compression blood volume and oxygenation decreased by approximately 15 and 5 % respectively relative to that at zero compression. Through extrapolation the authors estimate that between 50 and 70 % of the original blood volume would typically remain under a compression force of 89 N, which they equate with full mammographic compression. This indicates that it should be possible to obtain useful optical measurements at full compression irrespective of the associated depletion in blood volume. Though others have reported somewhat larger compression forces of approximately 120 N to be typical (Sullivan et al 1991) this remains a useful observation. As well as these findings the authors also present an algorithm allowing the bulk volumetric blood flow and oxygen consumption rates (per unit volume of tissue) to be calculated from the transient changes in blood volume and oxygenation measured. In the future the extension of such techniques might allow differing levels of metabolic activity within the breast to be mapped, thus providing further diagnostic information.

Boas' group have also performed a dynamic optical imaging study using their combined optical and x-ray system (§1.8.1). This was very limited as they imaged just one, healthy, volunteer (Boverman et al 2007). Optical images of the blood volume and oxygenation were acquired, over a period of 45 seconds, once mammographic compression had been applied. As the breast tissue relaxed following the compression its blood volume was observed to increase a little. These increases were found to be smaller in areas of the breast identified as being fibroglandular from the x-ray image. As fibroglandular tissue is

relatively stiff this was hypothesised to be because these areas were least affected by the compression and thus underwent the least recovery. In addition blood oxygenation was seen to decrease during the period following compression, the largest changes seen in regions of fibroglandular tissue. This was likely because oxygen consumption exceeded supply, due to restricted blood flow, and the fibroglandular regions are the most metabolically active.

Whilst the results of these studies are a little varied all have demonstrated that breast compression causes measurable changes in blood flow and oxygenation. To date none of the dynamic studies performed have included patients with cancerous lesions but it has been hypothesised that these will respond to compression differently to surrounding healthy tissue. Combined with their different metabolism it seems very plausible that the visibility of cancerous lesions in optical images could be improved through the performance of dynamic imaging whilst compression is applied and released. This increases the demand for rapid optical acquisition as several separate images would need to be acquired within the period over which compression was applied or released.

1.9. X-ray and optical phantoms

In order to ensure that x-ray mammography equipment is operating as expected and produces images of acceptable quality, stringent testing is vital. Within the NHSBSP a variety of quality control tests which must be performed at varying time intervals have been implemented (Cush et al 2007). These tests rely upon the imaging of phantoms which allow various performance parameters to be quantitatively assessed. In this way it can be verified that a system's performance has not deteriorated since its previous assessment and that it is within acceptable limits.

Though a number of mammographic phantoms are commercially available virtually all are designed to enable testing of the same two parameters: spatial and contrast resolution. These phantoms are typically made from solid plastic, having an attenuation coefficient equal to a specified thickness of breast tissue, and contain a number of image details (figure 1.7). Spatial resolution is commonly assessed by imaging several bar patterns containing alternating lines of attenuating and transmitting material. Each pattern contains lines of a different width and each thus has a different spatial frequency. The highest frequency pattern whose lines can be resolved determines the spatial resolution,

commonly quoted in line pairs/millimetre. Separate details test the contrast resolution. These consist of details of varying attenuation, becoming closer and closer to that of the background material in which they are embedded. In this way the minimum discernible difference in contrast is determined.

In order that different thicknesses of breast tissue (and therefore different levels of attenuation and scatter) can be mimicked some phantoms consist of stackable plastic sheets (for example the TOR MAM and TOR MAX made by Leeds Test Objects, Boroughbridge). Only one of these sheets contains the test details and the others can be added or removed as required. A small number of phantoms have also been designed to produce images with a randomly structured, rather than homogeneous, background more realistic of that seen in real mammograms (for example the BR3D phantom made by CIRS, Virginia).

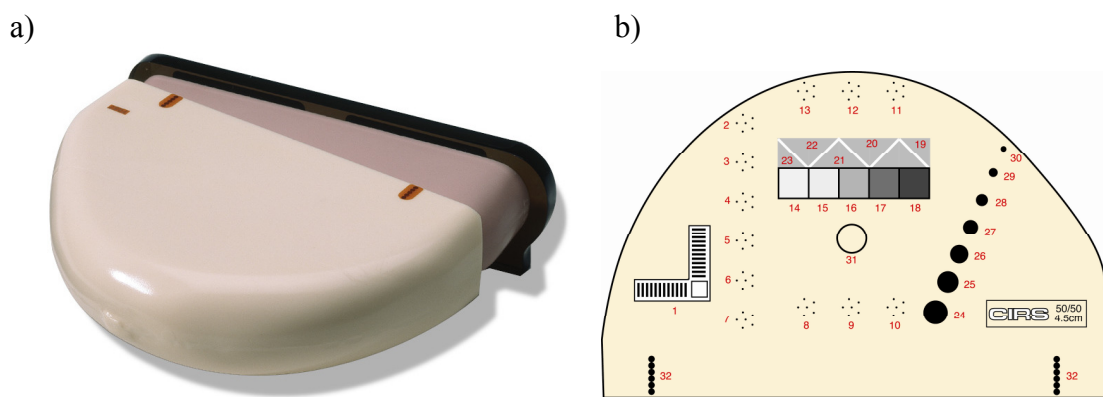


Figure 1.7. a) The CIRS tissue equivalent mammography phantom (Model 011A) is a typical x-ray mammography phantom. b) A diagram of the details within the phantom. Note the bar patterns for testing spatial resolution (labelled 1) and the details of varying attenuation to test contrast (labelled 24-30 amongst others). Images courtesy of Computerized Imaging Reference Systems Inc.

As with x-ray mammography optical phantoms are required to characterise the performance of optical tomography systems. Whilst a number of such phantoms have been developed (Pogue and Patterson 2006) very few are currently produced on a commercial scale. A number of solid, optically tissue equivalent, phantoms have previously been developed at UCL (Firbank et al 1995, Firbank and Delpy 1993). These are made using polyester or epoxy resins to which scattering and absorbing media can be added (figure 1.8). Regions of contrast are typically introduced by drilling a hole within a previously cast homogeneous block and filling this using resin with different scatter and

absorption coefficients. Very similar phantoms made from polyurethane resin have recently become commercially available ('BioMimic' phantoms made by INO, Quebec). A small number of phantoms have also been produced using silicone rubber. An advantage of this material is that it is slightly pliable and more uniform contact can be achieved with source and detector fibres, potentially reducing image artifacts (Jiang et al 2003a).

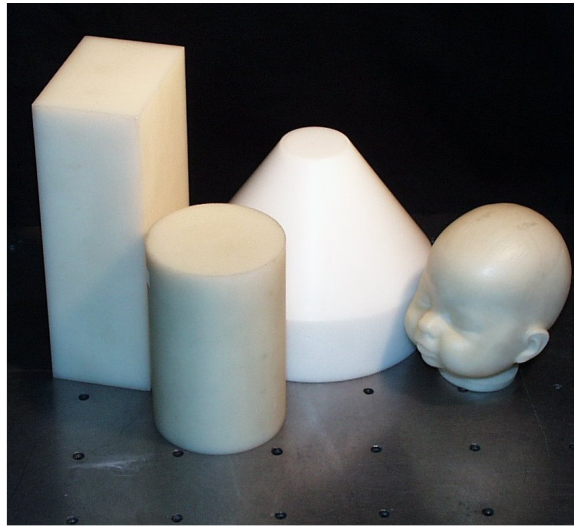


Figure 1.8. Examples of the solid resin optical phantoms that have been developed at UCL

A number of phantoms capable of demonstrating dynamic changes have been developed. Recently resin based phantoms containing very small electrical resistors such that regions can be gently heated have been developed (Hebden et al 2008). The presence of a thermochromic powder within the resin, whose optical absorption changes at a low transition temperature, allows the absorption of different regions to be altered in time. Dynamic changes in absorption can be produced as typical of, for example, functional brain activation. Similar phantoms have been produced by others using electrochromic materials (Barbour 2006). Previously dynamic phantoms had relied upon the movement of a region of contrast within a solution of intralipid (a fat emulsion) (Everdell et al 2005, Schmitz et al 2002, Yamashita et al 1999). Such fluid based phantoms are rarely stable over time and are difficult to store. An optical phantom utilising real blood whose level of oxygenation could be increased or decreased (through the perfusion of oxygen and activation of yeast respectively) has also been made (Wolf et al 1999).

1.10. Summary of thesis research

In the context of the literature described above, the research undertaken in this thesis falls into three areas:

- Investigation of the effects of step and shoot acquisition, as employed by the I-Imas, on spatial resolution (chapter two).
- Exploring the feasibility of optimising the acquisition of optical data in the planar transmission geometry (chapter three).
- The development of a compressible phantom material with mechanical, x-ray and optical properties equivalent to breast tissue (chapter four).

Chapter five summarises the key contributions of this thesis and proposes a number of avenues for future work.

Chapter Two

Assessing the validity of modulation transfer function evaluation techniques with application to small area and scanned digital detectors

This chapter is reproduced from a paper published in the Review of Scientific Instruments (Price et al 2008). It presents work which was performed to characterise the resolution of the I-Imas system, thereby investigating the effects of scanning on spatial resolution.

All the data presented within this paper was acquired jointly by myself and C.J. Esbrand, another PhD student within the radiation physics group at the time. At each stage many decisions had to be made as to the best methods of acquisition or data processing. I made all of these informed decisions, reviewing the relevant literature and analysing the various results of different approaches as required. A large number of significant Matlab codes had to be written in order to process the data produced and extract the necessary results. These were written entirely from first principles by me. Finally I authored the entire paper under the guidance of my supervisors, G.J. Royle and A.P. Gibson, as well as A. Olivo. Useful advice and discussion was also sought from J.C. Hebden and R.D. Speller. The idea of extensively investigating the effects of sensor area and scanning on resolution developed as the work progressed and following many discussions resulting from my decisions and observations. The author list was as follows:

B.D. Price, C.J. Esbrand, A. Olivo, A.P. Gibson, J.C. Hebden, R.D. Speller and G.J. Royle

2.1 Chapter Overview

Clinical radiology requires very high quality images to be obtained whilst utilising the minimum possible dose. This requirement drives the development of phantoms and the routine testing of mammography equipment. Image quality is typically assessed through evaluation of a system's spatial and contrast resolution. Spatial resolution is typically characterised by means of the system's modulation transfer function (MTF). In this work the spatial resolution of a novel system developed within the radiation physics laboratories at UCL, the Intelligent Imaging System (I-Imas), is characterised.

The I-Imas is a novel prototype step and shoot x-ray system. The system's mode of acquisition means that large overall images are obtained by aligning many smaller images. This chapter investigates the effects that this acquisition modality has on the overall spatial resolution of the system. Different modulation transfer function (MTF) evaluation techniques are reviewed and those shown to be optimal are used in the investigation of two considerations key to such a system: (i) whether there is a minimum size sensor whose MTF can accurately be determined using these techniques and (ii) whether the MTF of the large overall image differs significantly from those of the many constituent images. As the use of step and shoot systems is becoming more and more widespread, both are important considerations. It was found that, for a fixed pixel pitch, the MTF is determined marginally less accurately the smaller the sensor area, with the perceived resolution varying by up to 0.1 lp/mm (line pairs/millimetre). It was also found that use of such a step and shoot technique does cause a very small overall degradation in resolution. The resolution of overall images was calculated to be 0.1 lp/mm lower than that of the individual images acquired.

2.2. Introduction

Digital detectors are widespread and typically have a spatial resolution of between 5 and 10 lp/mm. Much work has been undertaken to allow comparison of different systems' spatial resolutions with one another and screen-film techniques. Typically the MTF, the ratio of output to input modulation expressed as a function of spatial frequency, of each system is used. Determining the MTF of digital detectors has become a well recognised process. Broadly the steps required are considered to be:

- a) Acquisition of an appropriate edge or slit image
- b) Determination of the position and orientation of this feature
- c) Appropriate oversampling of the pixel data
- d) Processing of the resulting edge spread function (ESF) to obtain a line spread function (LSF)
- e) Fourier transformation of the measured LSF to obtain the MTF

Many different means of performing each step have been cited and the relative advantages of each must be considered in determining an overall method (Samei et al 2006, Samei et al 2005).

The I-Imas was developed at UCL to allow methods of intelligently distributing the dose utilised in radiography to be investigated. This is achieved through the acquisition of two consecutive images, as summarised in §1.6.2. The system uses collimators to split the x-ray beam in two: the first, “scout beam”, strongly attenuated, is used to acquire a low exposure scout image and identify regions of interest. Rapid analysis of the parameters from this scout image then allows the intensity of the second beam to be modulated appropriately. In this way the exposure of different regions within the second image can be optimised – i.e. “interesting” regions of the sample receive a higher dose whereas other regions receive a lower one. Such systems may be capable of improved diagnostic capability at the same overall patient dose levels as typical when using large area digital plates. The I-Imas operates on a step and shoot basis (Griffiths et al 2006, Schulerud et al 2007). For simplicity this step and shoot approach is also referred to as “scanning”. A large overall scanned image is generated through the alignment of many smaller images consecutively acquired by an array of small sensors while the sample is stepped through adjacent positions. With such a mode of operation two separate images of the subject are acquired, one after the other, using two separate columns of sensors. The first is taken at a low exposure and the parameters from this used to adjust the exposure of different regions in the latter image. The exposure of each region is controlled by the motion of a step filter, allowing the beam to be attenuated by between 0 and 100 percent in 20 percent intervals, aligned with each of the sensors in the second column (figure 2.1). This way the dose can be redistributed or reduced without degrading the image quality obtained (Schulerud et al 2007). Each column consists of 10 scintillator coated CMOS active pixel sensors. Each sensor is 512 by 40 pixels in size, each pixel being 32µm square. The scintillator is a 100µm layer of structured CsI(Tl).

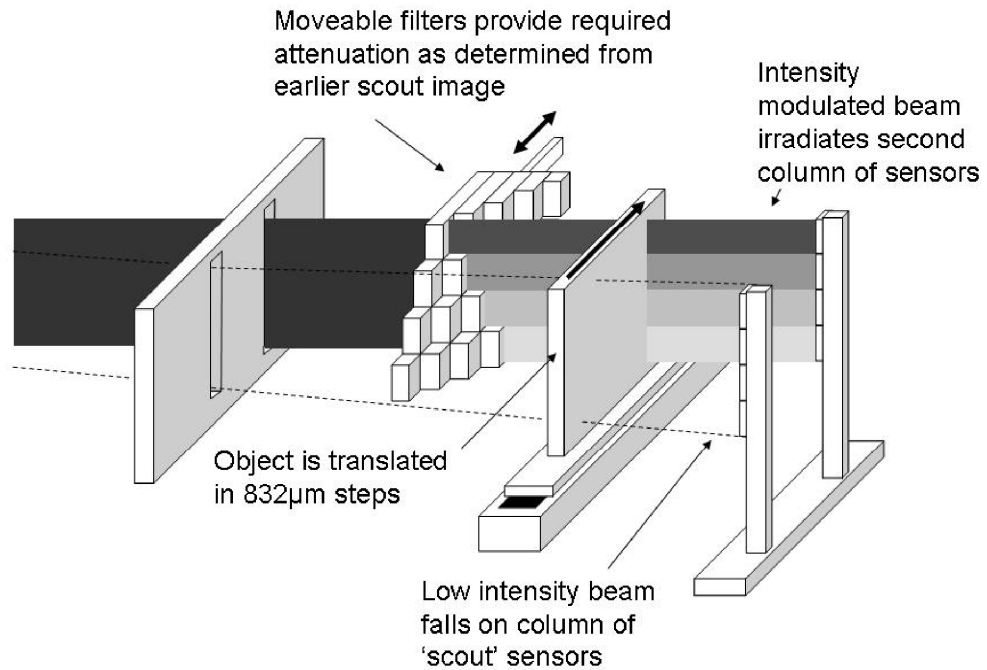


Figure 2.1. The schematic of the I-Imas system developed at UCL (as originally shown in chapter one but reproduced here for the reader's benefit). A low intensity scout image is acquired and the level of filtration utilised in the latter exposure adjusted accordingly. For simplicity only four sensors are shown per column (and four step filters aligned with second column). Each column actually has 10 sensors (and 10 step filters are aligned with the second column). The implication of the 832μm translation step size is discussed further in §2.3.5.

The nature of this technique raises two considerations to MTF determination, unique to such a system, that have so far been overlooked. Firstly is there a minimum size sensor whose MTF can accurately be determined? To date mostly digital plates with large pixel arrays have been considered. Secondly does the MTF of an overall scanned image differ significantly from those of the many smaller constituent images?

Whilst the work presented was performed on the I-Imas it should be noted that these considerations apply more generically to other scanning systems such as Fischer's SenoScan® (Besson et al 2002). This system uses a slot detector just 10 mm wide but 220 mm long. The x-ray source is collimated so as to irradiate an area just larger than this. Scanning the source and detector simultaneously, acquiring an image at each position and aligning these with one another, allows a large area image to be acquired (typically 300 by 220 mm). This approach to acquisition inherently reduces the amount of scattered radiation detected without using an anti-scatter grid. This is advantageous as anti-scatter grids also attenuate primary radiation, thus increasing the patient dose required to maintain optimal exposure (Lai et al 2004).

In the following work the methods that can be used at each stage of MTF determination are considered and what is argued to be the best overall technique established. This technique is then used to determine MTFs from progressively smaller digital images (in terms of array, not pixel, size) in order to investigate whether the MTF as measured by this technique is dependent upon the image size (effectively that of a sensor). In addition the average MTF of four scanned images acquired by a sensor are calculated and compared to the average MTF of four individual images acquired by the same sensor. This allows observation of the effect of scanning upon the MTF.

2.3. Method

2.3.1. Edge or slit?

Use of both edge and slit images in determination of the MTF is common (Buhr et al 2003, Fujita et al 1992, Greer and van Doorn 2000, Samei et al 1998). The edge method requires a much lower level of exposure for sufficient irradiation of the detector and is theoretically less sensitive to any physical defects of the test device (Samei et al 1998). Further theoretical advantages are that neither finite width correction (Boone and Seibert 1994, Dobbins et al 1995) of the LSF obtained, nor the interpolation of its tails to estimate the low frequency responses (Cunningham and Reid 1992, Fujita et al 1992), are necessary as with the slit method. Though the slit method is theoretically more accurate than the edge in determining responses at high frequencies the reverse is true for low frequencies (Cunningham and Reid 1992). It is these low frequencies (below the Nyquist) that are of interest if determining the detective quantum efficiency or noise power spectrum (Fetterly et al 2002). An opaque edge method is that recognised by international standard IEC 62220-1 (Samei et al 2006). For these reasons the edge method is used in this work.

Using an opaque edge minimises scatter which otherwise causes blurring of the ESF obtained and leads to over estimate of the MTF (Neitzel et al 2004). Conversely complete opacity leads to MTF distortion by reducing the level of quantum noise in one tail of the ESF relative to that in the other whilst too high a transmission reduces edge contrast and results in an unacceptably small signal to noise ratio. Overall a transmission of around 10% is recommended (Samei et al 1998). This work was performed using a finely polished 250 μm thick metallic steel edge and a tungsten source operated at 31 kV

and 5 mA. This was measured to give a 10% transmission. All images acquired were flat field corrected.

2.3.2. Calculation of edge position and angle

The position and angulation of an edge within an image are commonly found by either of two methods - Hough transformation (Samei et al 1998) or linear regression (Greer and van Doorn 2000). This regression technique considers each line of pixels approximately perpendicular to the edge in turn. The location of the edge within each line is determined to sub-pixel accuracy and the linear fit to these locations, by regression, gives the edge position.

In this work a further simplified method of regression was used. Whilst it was originally intended to work to sub-pixel accuracy this was found to be unnecessary. The technique employed still found the edge position in each line of pixels but not to sub-pixel accuracy. Within each line a mean value was calculated from each of two pixel groups - from the 10 pixels furthest from either side of the edge. The mid-value between these two extremes was calculated and the pixel having the closest value to this taken as that at the position of the edge within that line. Linear regression to these points was then performed.

Though more straightforward this method gives no less accurate a determination than Hough transformation. In many of the acquisitions performed the edge was aligned approximately parallel to the sensor's longer (512 pixel) side (§2.3.5). The largest possible error in angle determination would result with the edge angled so as to rise the height of one pixel whilst traversing 512. The true angle would be $\tan^{-1}(1/512) = 0.1^\circ$ (to 1 decimal place) whilst the simplified regression technique would return 0° . This maximum error of 0.1° has proven acceptable when using the Hough transformation (Samei et al 1998). In practice the error is very much lower; the edge is generally orientated at a steeper angle than this, rising the height of approximately two pixels whilst traversing the image even at 'shallow' orientations.

2.3.3. Oversampling the ESF

The simplest method of oversampling the ESF, ‘single sampling’, is to calculate the perpendicular distance from the edge to the centre of each pixel in the image. The value of each pixel is then plotted against its distance from the edge, resulting in an ESF with as many data points as pixels in the image.

If the orientation of the edge is sufficiently steep that it rises the height of several pixels in traversing the image then ‘multi sampling’ is viable. A number of ESFs are obtained by separately ‘single sampling’ strips, each N pixels wide, of the image. N , rounded to the nearest integer, is determined from the gradient, g , of the edge.

$$N = \frac{1}{g} \quad (2.1)$$

The ESFs obtained are superposed upon one another and an average taken. The technique employed is that of Buhr et al except that the points lying between the 35% and 65% levels were used in aligning the ESFs rather than those between 30% and 70% (Buhr et al 2003): this was to ensure that only the linear regions of the ESFs were considered, as is required. The results of the two sampling techniques were considered in order to establish the best method (see §2.4.1).

2.3.4. Processing the ESF

If the sampled ESF is too noisy this can mask the signal upon differentiation to obtain the LSF: the gradient between consecutive points should be much smaller than that of the overall step and a smooth ESF is thus desirable. Many smoothing filters, for example moving average, inherently alter the shape of the function they act upon and are thus unsuitable. Though median filters do not necessarily alter the shape of a signal they are best suited to the removal of distinct outliers rather than overall smoothing operations. Fourier filtering can be used as a method of smoothing and the extent to which this alters a function’s shape is more readily controlled.

An alternative to smoothing the ESF is to fit a known mathematical function which is then processed analytically. This has two theoretical advantages. Firstly when the fast Fourier transform of the LSF is taken, to obtain the MTF, this requires even sample

spacing. Working analytically with a known function avoids the interpolation of sampled data points to obtain this. Secondly calculating the gradient between all consecutive points of the ESF in order to determine the LSF, which requires multiplication of the MTF with a correctional sinc term (Cunningham and Fenster 1987), is also avoided. The sensors of the I-Imas system were all found to have an LSF that can to good approximation be represented by a Gaussian curve. In this case the error function (ERF), the integral of a Gaussian, can be fitted to the ESF (Bentzen 1983, Greer and van Doorn 2000). Bentzen fitted an inverse polynomial approximation of the ERF (Bentzen 1983),

$$ERF(x) = C_1 \times P\left(\frac{x-m}{\sigma}\right) + C_2 \quad (2.2)$$

where

$$P(z) = 1 - \frac{1}{2} \left[\sum_{n=0}^4 a_n z^n \right]^{-4} \quad 0 \leq z < \infty \quad (2.3)$$

and

$$a_0 = 1, a_1 = 0.196854, a_2 = 0.115194, a_3 = 0.000344 \text{ and } a_4 = 0.019527 \quad (2.4)$$

For negative z values the relationship

$$P(-z) = 1 - P(z) \quad (2.5)$$

is used.

This polynomial is fitted to the ESF through least squares regression, thus determining the values of the four variables C_1 , C_2 , m and σ ; the contrast step, value to the low side of the edge, mean position of the distribution and the standard deviation respectively. Both Fourier filtering and fitting of the ERF were attempted (§2.4.1).

2.3.5. Investigating the effect of sensor size and scanning

Having decided the optimal method by which to obtain the MTF through consideration of initial results two considerations were made. Whether: a) The MTF obtained for a particular sensor is dependent upon the size of the region sampled, and b) The MTF of a scanned image is different from that of the sensor from which it originated.

The first consideration was addressed in two stages as there are two reasons the MTF may vary with sensor size. Firstly fewer pixels are sampled so there is a statistical consideration – the ESF obtained is based on fewer data points. Secondly the accuracy to which the edge angle is calculated will vary. To separate these two effects progressively smaller regions were sampled using a fixed edge angle and position as calculated from consideration of the entire sensor area. After this each region was sampled a second time but using edge positions and angles recalculated solely from this region. In both cases the areas considered were generated by repeatedly halving a particular sensor image. As a result the regions considered were 40*512, 40*256, 40*128, 40*64 and 40*32 pixels in size. There is little gain investigating smaller sizes as sensors this small are unlikely to be useful. Two edge images, one with the edge orientated steeply and one more shallowly, were acquired with each of seven sensors. ‘Steeply’ was defined as $N \leq 50$ and ‘shallowly’ as $N \geq 200$ (recall $N = 1/\text{gradient}$). Acquiring images at both gradients was necessary to evaluate the two possible sampling methods (§2.4.1). The method of angle determination is described in §2.3.2.

The second consideration was addressed by acquiring eight separate images using the same sensor. Half of these were scanned images and half were individual full sensor images. Each individual sensor image was acquired with the edge aligned approximately parallel to the longest (512 pixel) side of the sensor. For each scanned image the edge was aligned approximately perpendicular to the longest side of the sensor and then moved a minimum of ten 832 (± 0.5) μm steps, an image acquired at each position. Each step is a movement equivalent to the width of 26 pixels and, as the sensor is 40 pixels wide, overlapping images were obtained. These were ‘stitched’ together with care taken to remove the overlap regions (7 pixels width removed from each side of individual images). A band 40 pixels in width approximately parallel to and centred over the position of the edge was selected from each scanned image for processing. This way the stitched images processed were the same width as the individual sensor images acquired with the edge in the opposite orientation (figure 2.2). In all cases the edge was positioned such that the angles calculated from the resulting images were shallow, $N \geq 200$. An MTF was calculated from each of these images and two average MTFs found – one from the four individual sensor MTFs and one from the four scanned image MTFs. Though the individual and scanned images were acquired with the edge at different orientations to the sensor the differences between the average MTFs can be attributed to the scanning

process if the sensor is assumed to be isotropic: this is a reasonable assumption as the sensor pixels are square and the scintillator was mounted as flatly as possible.

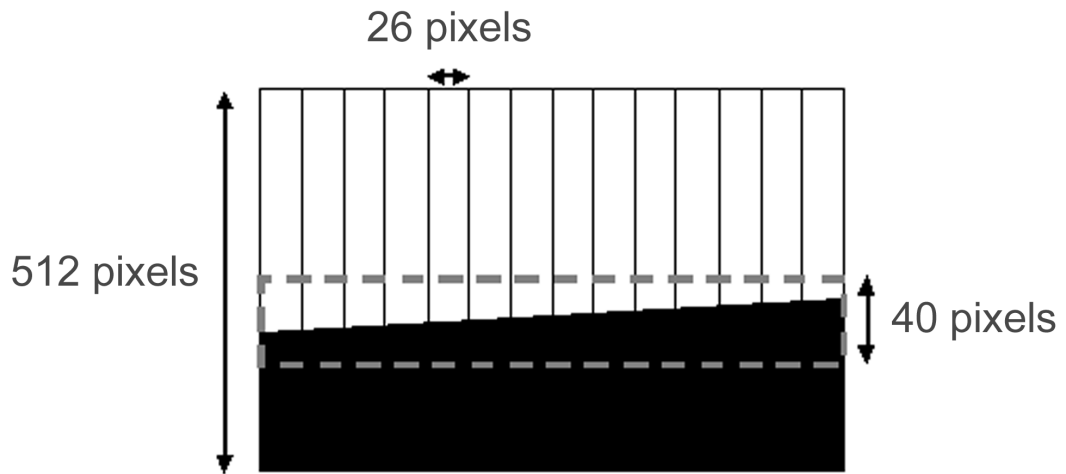


Figure 2.2. The way in which 14 individual images are stitched to create a larger image. The grey dotted line encloses the region of interest used in MTF calculation. Each individual image (originally 40 pixels wide) has had seven pixels width cropped from each side and has a total width of 26 pixels after overlap removal.

2.4. Results

2.4.1. Method of MTF determination

Comparing the single and multi sampled ESFs of a particular sensor showed that multi sampling generates a smoother ESF. The standard deviation of the differences in counts between consecutive points in the multi sampled ESF was nearly 6 times smaller than that of the single sampled ESF. Processing as smooth an ESF as possible would be advantageous if applying a smoothing filter but has a lesser influence on the outcome of ERF fitting. Though Fourier filtering was partially successful in smoothing the ESFs a certain level of low frequency sinusoidal fluctuation always remained in the outputs. For this reason ERF fitting as performed by Bentzen was chosen (Bentzen 1983). As multi sampling has several other disadvantages over single sampling (§2.5.1) and ERF fitting had been chosen single sampling was used. Fits were accepted once the minimum least squares value had been determined to at least 2 decimal places – several orders of magnitude more precise than the size of the values themselves. Having determined these variables the analytical MTF was readily derived.

The expression for the LSF is

$$LSF(x) = \frac{C_1}{\sigma\sqrt{2\pi}} \exp\left[-\frac{(x-m)^2}{2\sigma^2}\right] \quad (2.6)$$

and the absolute value of the Fourier transform of the LSF is the MTF

$$MTF(\omega) = C_1 \times \exp(-\sigma^2\omega^2/2) \quad (2.7)$$

This result is normalised to attain a maximum value of unity.

2.4.2. MTFs obtained

2.4.2.1. MTFs of separate sensors

The MTF of both the highest and lowest performing of the seven sensors tested as well as the average MTF of all is shown in figure 2.3.

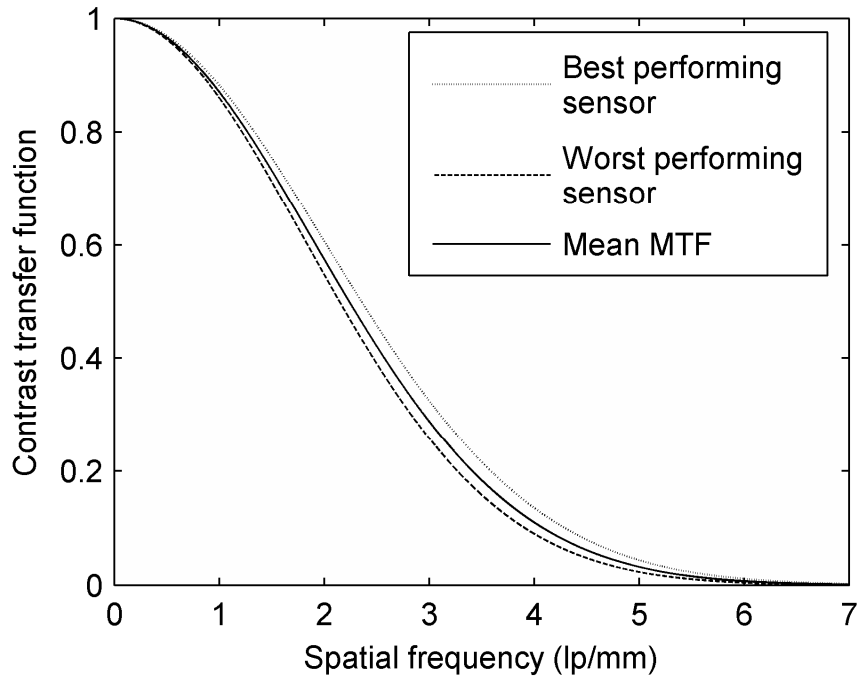


Figure 2.3. MTFs of the highest and lowest performance sensors as well as the mean MTF of all seven sensors.

2.4.2.2. Effect of sensor area

The effect of reducing the sensor area used in determining the MTF without recalculating the edge angle can be seen in figure 2.4. Though only the full and sixteenth area MTFs of one sensor are shown it was found without exception that the smaller the sensor area, the worse the estimated system performance, albeit the difference being very small. At the 10% level, that at which the measured spatial resolution is often taken as a system's maximum, there is approximately a 2% reduction in resolution. Comparable results were found when the edge angle was recalculated for each area considered.

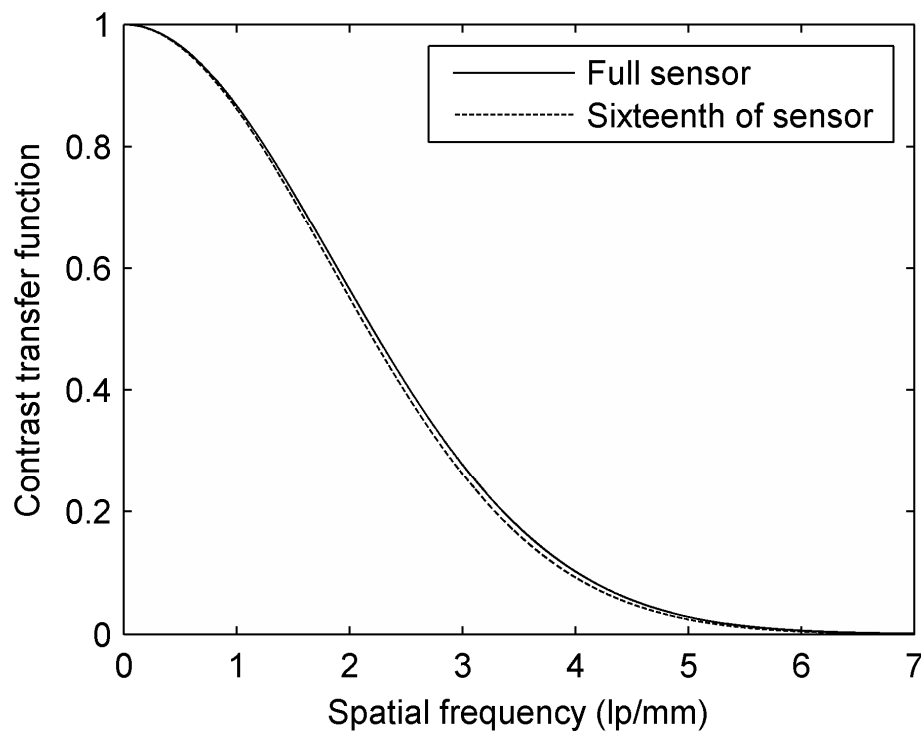


Figure 2.4. MTFs obtained when sampling the ESF of a particular sensor from its full area and one sixteenth of this.

2.4.2.3. Effect of scanning

The average MTFs calculated from the four scanned and un-scanned images are shown in figure 2.5. All the MTFs calculated from the scanned images showed slightly lower performance than all those calculated from the un-scanned sensor images. At the 10% level the difference in resolution between the two average MTFs is 0.11 ± 0.04 lp/mm.

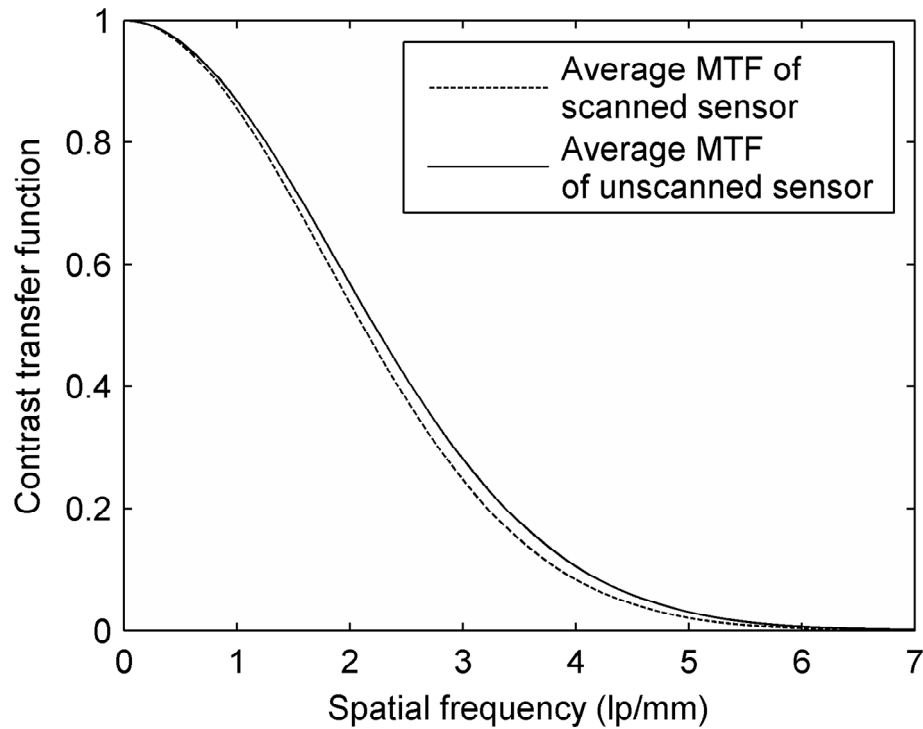


Figure 2.5. Average MTFs obtained from the individual images of a sensor and from larger, scanned, images acquired using the same sensor.

2.5. Discussion

2.5.1. Single over multi sampling

There are two reasons that multi sampling was considered to be inferior to single sampling. Firstly multi sampling requires a steeper edge angle and because of this the sampled distances from the edge do not change in such small increments. As their range of possible values is not evenly represented the extent of oversampling is reduced. Secondly, and more significantly, only the range of distances occurring within all of the individual ESFs can be represented in the average ESF. Due to the angulation of the edge the extreme distances to either side appear only in the first and last ESFs sampled. Particularly at larger angles this loss of information becomes noticeable, resulting in a significant cropping of the ESF tails. This reduces the accuracy with which the tails of the LSF can be determined and could ultimately necessitate interpolation as would be required if sampling a slit.

2.5.2. Variation between individual sensor MTFs

The maximum spatial resolution of a system is often taken as that at which the contrast transfer function drops to 10%. Between the highest and lowest performing sensors there is a difference in resolution of nearly 0.5 lp/mm at this level. As all of the sensors are identically built this variation is likely due to differing levels in the quality of scintillator coupling. In well coupled cases the layer of optical gel between the scintillator and sensor will be very thin whilst in poorer couplings this will be thicker. The resolution achieved is worse the thicker this diffuse layer becomes. In a brief experiment a slit image was acquired using a sensor whose scintillator was deliberately set at an angle. The slit image grew broader along the image, as the coupling layer became thicker. In order to acquire a large two dimensional image an array of small sensors is used (Griffiths et al 2006). In order to maintain a constant resolution across all regions of such an image the coupling across all sensors would have to be identical. It should be noted that the effect of the scintillator itself, let alone the diffuse coupling layer, is very marked – theoretically a sensor with a 32 μm pixel pitch could achieve a resolution a little under 30 lp/mm at the 10% level if this were not degraded by the scintillator. When considering the effects of sensor area or scanning it should be noted that the same sensor was used throughout in order to exclude the scintillator or its coupling as possible causes of the observations made.

2.5.3. Effects of reducing sensor area and scanning

Reducing the area of the sensor used in calculating its MTF caused a very slight reduction in the perceived performance. The difference in observed resolution at the 10% level is approximately 0.1 lp/mm between the MTF obtained using the full area of a sensor and one sixteenth of it. This represents a reduction in resolution from approximately 124 to 127 μm . Though this effect is small the consistency of this reduction strongly suggests that it is not coincidental and furthermore it can be explained theoretically. Use of a smaller area means that fewer pixels are sampled and the extent of oversampling is reduced. A high level of oversampling is critical to the accurate calculation of the MTF and as this becomes poorer the accuracy of the determination is reduced (Dobbins 1995). As fewer pixels are sampled the determination also becomes more susceptible to the effect of noisy or abnormal pixels as the ERF fit is performed to fewer points. This also reduces the calculated resolution. As the degradation seen was of similar magnitude

when the edge position was recalculated for each area it appears that the reduced oversampling is much more significant than any reduction in the accuracy to which the edge position is determined when based upon smaller areas. If one wished this oversampling problem could be overcome by acquiring multiple images, each with the edge orientated slightly differently, though this could be very time consuming. It is also worth noting that if the number of pixels in the other direction (40 pixel width) had been reduced difficulties would have been encountered in determining the edge position. In order for this to be found accurately there must be a number of pixels to either side of the edge whose intensities are unaffected by its presence.

It is also clear that the overall resolution of step and shoot images is very slightly poorer than that of the sensor with which they are acquired. On average there is a difference of approximately 0.1 lp/mm, at the 10% level, between the spatial resolution of the sensor itself and an overall step and shoot image acquired by it. This reduction in resolution is almost certainly due to 'blurring' as consecutive images cannot be perfectly aligned. The sensor movements were by micro controllers whose error in positioning is estimated to be 0.5 μm per step. This uncertainty should be made as small as possible to reduce this effect.

It is important to clarify that the differences between MTFs calculated from different size areas of the same sensor are almost certainly due to the poor level of sampling. As the sensor pixels are square and the scintillator construction and coupling techniques ensured as flat a mounting as possible there is no reason to believe that certain regions of a given sensor should have a significantly different spatial resolution to others. The resolution of the sensor regions considered does not change: rather the accuracy to which this resolution is calculated. In the case of scanning the resolution of the obtained image is actually reduced. The change seen is not due to different levels of accuracy in determination of the MTF.

2.6. Conclusions

It has been shown that, using the edge method, it is harder to accurately determine the MTF of a sensor the smaller it is. This is primarily due to the reduced level of oversampling achieved. For sensor sizes down to those of clinical use this effect is unlikely to have major implications. The spatial resolution can still be found to around

0.1 lp/mm in sensors as small as 32*40 pixels in size. As pixels become increasingly smaller a greater number will need to be sampled in order to obtain as accurate a determination; one must ensure to sample in the tails of the ESF, well away from the edge as well as close to it.

The effects of stepping are potentially more significant. The resolution of step and shoot images will see a small degradation compared to that of the acquiring sensor unless the consecutive images can be perfectly aligned. Any step and shoot systems will thus require very precise engineering to ensure that the stepping of the sensors is as accurate as possible. In systems such as the I-Imas where a number of small sensors are positioned one above the other it would also be important to ensure that these were all parallel with one another. One would have to align the images of independent sensors with one another as well as the images from each one. It is also worth noting that, in the I-Imas, overlap of the images allowed their edges to be discarded. In other circumstances edge effects could play a role. If edge effects occurred and entire sensor images were aligned with one another then these could also affect the overall image resolution. A balance must be struck as too great an overlap leads to more acquisition positions and increased dose whilst too small an overlap could lead to these edge effect problems. Similarly post-processing of step and shoot images can be performed to increase their resolution (Olivo et al 2000) but these may require smaller step sizes than dose considerations allow. Whilst both sensor area and scanning have an effect on the observed resolution the cause of this differs between the two cases. In the case of reduced sensor area the small reduction in resolution is likely perceived due to inaccuracy in determination. In the case of scanning a true reduction occurs due to 'blurring' caused by slight misalignment of consecutive images.

It should be noted that the differences seen between MTFs caused through reduced area sampling or scanning are small relative to the variations seen between different sensors' MTFs. This indicates that, in the current system, the spatial resolution achievable is limited by the scintillator and its coupling rather than the sensor setup and scanning. In future systems it would be very important to manufacture all the sensors to very exacting specifications so as to avoid variations in their performance due to scintillator quality or coupling. Despite the effects observed in this work there is no reason that they should present a barrier to the development of step and shoot systems like the I-Imas or Senoscan. These effects are typically very small and, to some extent, can be overcome.

Chapter Three

Optimisation of illumination in diffuse optical imaging

3.1. Chapter Overview

In this thesis it has been proposed that a dual modality mammography system would ideally perform both acquisitions as rapidly as possible under full mammographic compression (§1.8.2.2). Though only providing intensity, and no temporal, information continuous wave (CW) imaging is very rapid (§1.7.3.2). This work investigates the feasibility of detecting heterogenous regions of absorption by visualising intensity data acquired in the parallel plate geometry. The ratios of the intensities detected during a reference measurement on a homogeneous phantom to those obtained imaging an object of interest (i.e. reference/object) are plotted as a function of detector position. In this way a ‘profile’ is obtained which highlights regions of the object with significantly different absorption to those of the homogeneous reference. Profiles obtained from both simulated and experimental data sets are presented.

The minimum change in absorption detectable through the analysis of these profiles will depend upon the accuracy to which each detector’s ratio value can be determined. For this reason methods of optimising these profiles are investigated. Initially four objective functions designed to quantify the clarity of the profiles are defined. Proof of concept work is performed to demonstrate that, subject to certain constraints, particular source power distributions can be found to optimise these objective functions.

3.2. Introduction

A number of practical limitations would have to be considered in order to develop a clinically acceptable x-ray and optical mammography system. These would include

- **Geometry.** In order to aid the registration and comparison of optical and x-ray images the breast would ideally be held in exactly the same position throughout both acquisitions (§1.8.2.2). For this reason the optical acquisition would have to be performed in the compression geometry, between two parallel plates. This is the geometry used in Boas' combined system (§1.8.1).
- **Duration of compression.** In order for an optical acquisition to be performed under such a high level of compression it would have to be performed very rapidly so as not to cause unacceptable discomfort to the woman being screened. In a typical x-ray mammogram compression is only applied for a matter of seconds.
- **Frame rate.** Simply acquiring one image over a period of 10 seconds at full compression would not allow dynamic imaging of blood volume and oxygenation to be performed. Ideally a number of much faster acquisitions would be made whilst compression was applied, held and then released. Dynamic imaging of this nature has been proposed as a possible way of increasing the contrast of breast lesions (§1.8.2.4).
- **Cost.** Clearly the cost of any imaging system should be kept as low as possible whilst maintaining the necessary level of performance.

These practical limitations would play a very significant role when making more technical decisions about the system's approach to optical acquisition. In an optode based system, using a finite number of source and detector fibres, some of the key parameters affected by the above limitations might be

- **Acquisition mode (time domain, frequency domain or CW).** The acquisition speed of time or frequency domain systems, whose sources must be activated sequentially, is typically slower than that of CW systems whose sources are all activated simultaneously (§1.7.3.2). Using a CW type system would ensure that the duration of compression could be minimised and allow dynamic imaging to be performed. In addition the hardware costs associated with CW imaging tend to be significantly lower than those of time or frequency domain systems.
- **Number and positioning of optodes.** Very little work has been done to determine how best a finite number of source and detector optodes should be arranged on two parallel plates in order to maximise image quality. Whilst the obtainable image resolution increases the smaller the spacing between optodes (Culver et al 2001) no studies seem to suggest placing a finite number of optodes in any manner but evenly over the required surfaces. This is logical as it ensures that the volume of interest is sampled as uniformly as possible. Using a greater number of optodes could increase both resolution and the amount of light collected but this would lead to longer acquisition times in time and frequency domain systems. In addition the use of a larger number of optodes would increase the cost of a system. A balance must be made.
- **Selection of wavelength(s).** In many systems two wavelengths are utilised such that the concentrations of oxy and deoxyhaemoglobin can be established (§1.7.1). The accuracy to which these concentrations can be determined depends upon the pair of wavelengths utilised (Yamashita et al 2001). Systems using a greater number of wavelengths can also determine the concentrations of further chromophores such as water and lipid, potentially improving specificity (Taroni et al 2005). Unfortunately the use of an increased number of wavelengths in time and frequency domain systems would increase acquisition time. In addition the cost of sources could rise if more lasers were required. In CW systems where relatively cheap laser diodes are used, and all wavelengths can be acquired simultaneously, these problems would still be a concern even if somewhat reduced.

- **Source power.** In modulated imaging systems the use of certain patterns of illumination have been shown to produce higher quality images than others (§1.7.2.4). In the limit of an infinitely large number of very small source and detector optodes similar effects would be seen in optode based systems if the intensity data was acquired in the correct manner. Nonetheless it is not clear that similar techniques can be applied to find optimal patterns of illumination across a relatively small number of source optodes. In modulated imaging the frequencies of modulation used typically range from 0 to 0.9 radians/millimetre. Some of these higher frequency patterns could not be generated using typical optodes (each MONSTIR optode has an external diameter of 8.5 mm). Furthermore work on modulated imaging has so far demonstrated its potential, using simple sinusoidal patterns, rather than seeking to find optimal patterns of illumination. Despite these observations investigating whether or not optimal patterns of illumination that maximise image quality can be found for optode based systems remains an interesting problem.

With the exception of acquisition mode the above parameters can, at least theoretically, be varied in numerous ways. This requires the development of mathematical approaches in order to determine the optimal conditions for acquisition within certain constraints (for example finding optimal wavelengths within a certain bandwidth and given that only a certain number can be used).

In this work source power is considered. The feasibility of visualising transmitted intensity data, as could be acquired by a CW system operating in the parallel plate geometry, in order to localise regions of heterogenous absorption is investigated. A ‘profile’ is obtained by plotting the ratios of the intensities detected during a reference measurement to those obtained imaging an object of interest as a function of detector position. Experimentally acquired data is used to demonstrate that such profiles are capable of highlighting regions of an object with significantly different absorption to those of a homogeneous reference. In this proof of concept work a very simple source detector layout was used: a one dimensional array of sources positioned opposite an opposing one dimensional array of detectors. This work is a pre-cursor to the development of a full imaging system. In a real system two dimensional arrays of sources and detectors would have to be used in order that two dimensional contour maps, as opposed to line profiles, could be generated.

As outlined previously the minimum change in absorption detectable through analysis of the profiles presented is likely to depend upon the accuracy to which each of the ratio values can be determined. For this reason methods of optimising these profiles, by varying the relative intensity of light emitted from each of the finite number of sources, are investigated. So far as the author is aware only one previous study, of relevance to the above considerations, has been performed. This study is now discussed in some detail as its findings seem to be incorrect. The reasons for this assertion and proof by counter example are presented.

3.2.1. Maximisation of distinguishability

The study in question considered varying the intensity of light emitted from each source whilst assuming a fixed set of optode positions (Serdaroglu et al 2006). The study's objective was to calculate the source power distribution that would maximise the distinguishability of two different optical property distributions from one another. The technique utilised was virtually identical to one used in electrical impedance tomography (EIT) (Cheney et al 1999, Gisser et al 1988). For this reason this technique is described before the work presented by the study is discussed.

In EIT currents are applied across a number of electrodes and the voltages resulting at these electrodes are simultaneously measured. An optimal current pattern is commonly determined as that which maximises the distinguishability, δ_k , of a change in the distribution of resistivity, from γ to τ , within a body (Eq. 3.1). V_l and I_l denote the voltage and current on the l th of L electrodes and k denotes the application of a particular current pattern.

$$\delta_k = \frac{\left[\sum_{l=1}^L (V_l^k(\gamma) - V_l^k(\tau))^2 \right]^{1/2}}{\left[\sum_{l=1}^L (I_l^k)^2 \right]^{1/2}} \quad (3.1)$$

If a matrix M is defined as the ‘resistive’ map which translates the currents applied to the voltages recorded then Eq. 3.1 can be expressed as

$$\delta_k = \frac{\|M(\gamma)I - M(\tau)I\|^2}{\|I\|^2} = \frac{\|\Delta M I\|^2}{\|I\|^2} \quad (3.2)$$

where $\|x\|^2$ denotes the vector norm, $\|x\|^2 = \sqrt{\langle x, x \rangle} = \sqrt{x^T x}$. Note that x^T denotes the transpose of x . It is critical to appreciate the importance of the denominator in Eq. 3.2. This has the effect of normalising the expression by the total power input (because Power = $I^2 R$, resistance being a fixed property of the body). Without this term the distinguishability can be made larger and larger by increasing the total current applied.

Now consider the definition of the Rayleigh-Ritz quotient of a vector x (Trefethen et al 1997). This is the scalar

$$r(x) = \frac{x^T A x}{x^T x} \quad (3.3)$$

where A is a matrix that is both real and symmetric. It can be shown that the gradient of $r(x)$,

$$\nabla r(x) = \frac{2}{x^T x} (A x - r(x) x) \quad (3.4)$$

The distinguishability function takes a very similar form to the Rayleigh-Ritz quotient. Expanding Eq. 3.2 gives

$$\delta_k = \frac{\|\Delta M I\|^2}{\|I\|^2} = \sqrt{\frac{I^T \Delta M^T \Delta M I}{I^T I}} \quad (3.5)$$

Now if A is defined as

$$A = \Delta M^T \Delta M \quad (3.6)$$

then it follows that

$$r(I) = \frac{I^T \Delta M^T \Delta M I}{I^T I} \quad (3.7)$$

The only difference between expressions 3.5 and 3.7 is a square root but this is not of significance as it is applied to the entire expression. The distinguishability, $\sqrt{r(I)}$, is maximised when $r(I)$ takes its largest possible value. Suppose that I is an eigenvector of $\Delta M^T \Delta M$ and λ is the associated eigenvalue. Then by definition

$$\Delta M^T \Delta M I = \lambda I \quad (3.8)$$

Substituting this relationship into Eq. 3.7 gives

$$r(I) = \frac{I^T \lambda I}{I^T I} = \lambda \quad (3.9)$$

Furthermore substituting Eqs. 3.6 and 3.9 into Eq. 3.4 gives

$$\nabla r(I) = \frac{2}{I^T I} (\Delta M^T \Delta M I - \lambda I) = 0 \quad (3.10)$$

So the eigenvectors of $\Delta M^T \Delta M$ represent the stationary points of the distinguishability function. The distinguishability is maximised when the current pattern applied is equal to the eigenvector associated with the largest eigenvalue of the matrix $\Delta M^T \Delta M$. Now that the principle of the optimisation is clear the optical study can be considered in detail.

In Serdaroglu's study data was simulated using the diffusion approximation to the radiation transport equation, a widely used model of light transport in scattering media (Boas et al 2001). A slab geometry was simulated in which a one dimensional array of sources was positioned opposite an opposing one dimensional array of detectors. In one case the slab was simulated to have homogeneous optical properties. In three other cases the slab was simulated to contain an absorbing region, within the same homogeneous background, at three different lateral positions as shown in figure 3.1a (to either end and in the middle of the source and detector arrays). For each of the four cases a source detector map was generated. These matrices defined the proportion of light from each source reaching each detector. They are analogous to the resistive maps used in EIT.

The source detector maps for any one of the absorption containing slabs and the homogeneous slab are denoted as $\Lambda(\mu_{a1})$ and $\Lambda(\mu_{a0})$ respectively. The matrix representing the difference between these maps can be denoted $\Delta\Lambda = \Lambda(\mu_{a1}) - \Lambda(\mu_{a0})$. S is defined as the source vector to be found (equivalent to I in EIT). C represents the covariance matrix of the noise vector describing each detector's noise level. For simplicity Serdaroglu appears to assume that the noise between different detectors is uncorrelated, setting C as the identity matrix. Serdaroglu's study attempts to maximise the value of D

$$D = \left\| [\Lambda(\mu_{a1}) - \Lambda(\mu_{a0})] S \right\|_{C^{-1}}^2 = \sqrt{S^T \Delta\Lambda^T C^{-1} \Delta\Lambda S} \quad (3.11)$$

which they define as the signal to noise ratio, given the constraint that $\|S\|^2 = 1$. This is exactly the same as the constraint applied in EIT in which the distinguishability is normalised by $\|I\|^2$ (Eq. 3.2). Serdaroglu states that the source vector, S , that maximises this expression is equal to the eigenvector associated with the largest eigenvalue of the matrix

$$\Psi = \Delta\Lambda^T C^{-1} \Delta\Lambda \quad (3.12)$$

This is only the case given that D is normalised by $\|S\|^2$ so as Eq. 3.11 can be expressed as

$$D = \frac{\left\| \Delta\Lambda S \right\|_{C^{-1}}^2}{\|S\|^2} = \sqrt{\frac{S^T \Delta\Lambda^T C^{-1} \Delta\Lambda S}{S^T S}} \quad (3.13)$$

This gives the expression the same form as the Rayleigh-Ritz quotient (Eq. 3.3). However this constraint is not valid. In EIT the source power, by which the distinguishability must be normalised, is proportional to I^2 . In contrast the optical power is directly proportional to the number of photons, not the number of photons squared. As such D should be normalised by ΣS , not $\|S\|^2$. Without this incorrect constraint the expression is no longer analogous to the Rayleigh-Ritz quotient and there is no reason that the eigenvector associated with the largest eigenvalue of Ψ should be the optimal source vector. In order

to demonstrate this a counter example is presented. As the data originally used by Serdaroglu was unavailable new data had to be modelled for this purpose.

Shortly the details of a modelling code designed to generate source detector maps for the same slab geometry as used in Serdaroglu's study (one dimensional array of sources opposing a one dimensional array of detectors) are presented (§3.3.4). The source detector maps used for this counter example were generated using this code and are presented without further explanation at this point. Figure 3.1 shows the calculated optimal source distributions, obtained for different positions of the absorbing region, if these are assumed to be the eigenvector associated with the largest eigenvalue of Ψ (Eq. 3.12). The distributions found are the same as those presented in the criticised study.

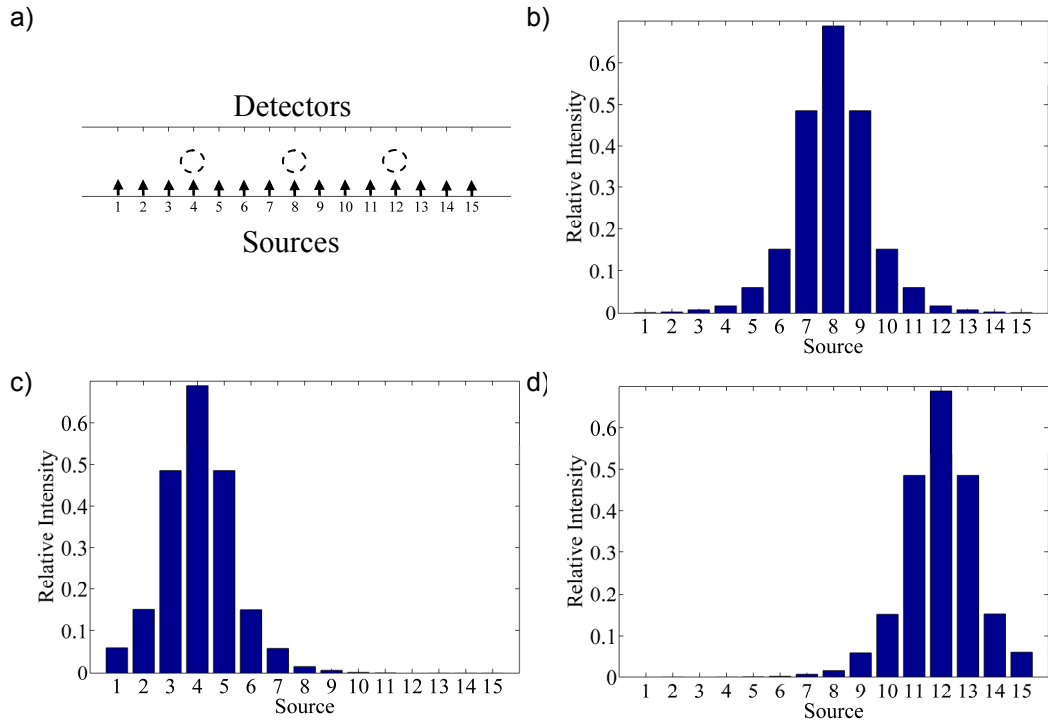


Figure 3.1. a) The modelled slab geometry. The three absorbing inhomogeneity positions simulated are shown. b-d) The optimal source intensity distribution found in each case (central, left and right).

Initially the results appear very plausible. The 'optimal' patterns channel more light through the absorbing region than equally illuminating each source would. This is likely to increase sensitivity to this area. Nonetheless these patterns are not truly optimal. Putting all of the light in at the single source directly above the absorbing region results in a significantly higher value of D . The values of D calculated (using Eq. 3.11) for each of the three cases are all approximately 140 if the optimal patterns shown in figure 3.1 are used whilst putting the same total amount of light in at the appropriate single source results in a value of approximately 210. Whilst this is likely to be the truly optimal

solution it might not make sense to illuminate a single source in practice. If no light is put in at other sources then it is unclear how much information would be gained about the rest of the object. Whilst the sensitivity to changes in a particular region are maximised most information about remaining areas would probably be lost. This limitation does not seem to arise in EIT: the optimal source vector found is generally more complex and does not pass all of the current through one electrode. The circumstances are very different. There is no reason that the size of the voltages generated at different points due to the injection of current at a source should be related to the number of photons detected at these points when the body is illuminated at the same source position as current is injected. In addition the electrodes are typically placed in a ring around the surface of the object to be imaged, for example the chest, instead of on opposing surfaces as in the slab geometry considered here.

Despite the limitations of Serdaroglu's study, defining measures of image quality and determining source power distributions that optimise these remains of interest. Four alternative, quantifiable, measures of image quality (objective functions) are now proposed. The acquisition/generation of the experimental and modelled data used to evaluate their performance is also described.

3.3. Method

3.3.1. Choice and justification of novel objective functions

Before formulating the objective functions, the way in which the intensity data obtained was visualised must be described. For this proof of concept work a simple slab geometry as previously described (figure 3.1a) was used. Data acquired in this geometry does not allow a full reconstruction to be performed but it is still possible to determine the nature and position of inhomogeneities within the source detector plane via a linear profile. All of the detectors are in a row and the total intensity of light detected at each, from all sources, can be found. For each detector the total amount of light detected, from all sources, during a reference measurement (on a homogeneous slab) can be divided by that detected during an object measurement (on a slab containing one or more inhomogeneities). This gives the relative differences between the total detected intensities measured during the object and reference measurements. Plotting the ratio values obtained versus detector position results in a profile displaying the position of any

changes in absorption (figure 3.2). The objective functions chosen were designed to maximise the clarity of profiles of this nature, thus aiding the detection and characterisation of heterogeneities.

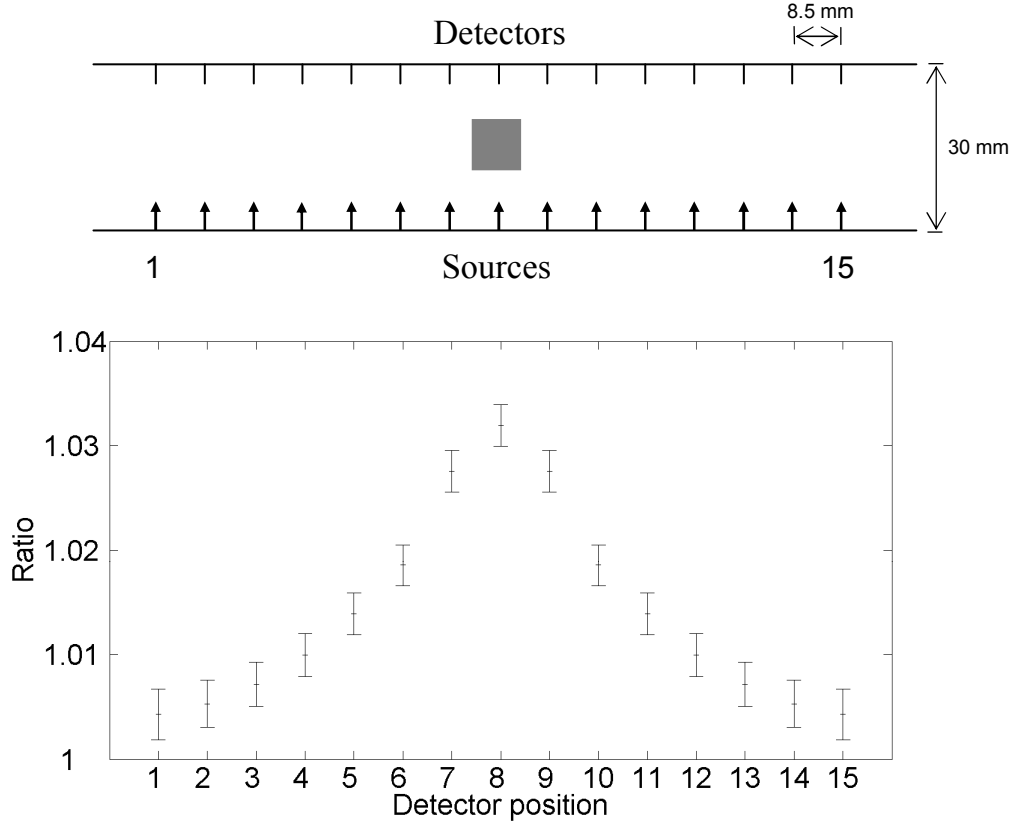


Figure 3.2. Profile obtained simulating a 1 cm^2 absorbing region ($\mu_a = 0.015 \text{ mm}^{-1}$) central to the optode arrays. The background absorption of the slab is 3 times lower, 0.005 mm^{-1} . The modelling code used to generate the reference and object source detector maps which lead to this profile is described in §3.3.4. Even at the extreme detectors, 1 and 15, the ratio value is not 1. Most light detected by these comes from nearby sources, and is thus unaffected by the presence of the central heterogeneity. Nonetheless some travels from distant sources positioned the far side of the heterogeneity and the presence of the heterogeneity does reduce the intensity detected from these sources. The nature of the error bars is discussed in §3.3.1.1.

Regardless of the imaging modality in question there are three parameters that are commonly maximised to enhance image quality. These are signal to noise ratio (SNR), contrast to noise ratio (CNR) and spatial resolution. In the majority of imaging systems spatial resolution is primarily dependent upon source and detector geometry. The placement of source and detector optodes, and the effect this has on spatial resolution, was briefly discussed previously (§3.2) and is not considered further here. The four objective functions chosen were all based on SNR and CNR and these are now described in detail.

3.3.1.1. SNR based objective functions

If the total amount of light detected at a given detector is the same for the reference and object measurements then the ratio calculated for this detector will be one. As such the ‘signal’ can be defined as the modulus of the difference of the calculated ratio from one. The noise on this signal is equal to the error on the determined ratio value. One objective function, SNR_{max} , was designed to find the optimal source power distribution that maximised the total sum of the SNRs, over all detectors. Another, SNR_{equal} , was designed to make the SNR of all of the points as similar to one another as possible. Improving the SNR at points where it is poor, whilst somewhat reducing the SNR at points where it is already very good, will lead to a more even SNR across the whole profile. These functions are now described mathematically.

For simplicity the expressions shown are based on the use of source detector maps for just three sources and three detectors (table 3.1). In practice the data analysed was always for fifteen of each. Whilst the expressions become larger the mathematical operations are identical.

	Detector 1	Detector 2	Detector 3
Source 1	a_{11}	a_{12}	a_{13}
Source 2	a_{21}	a_{22}	a_{23}
Source 3	a_{31}	a_{32}	a_{33}

Table 3.1. The source detector map for three sources and detectors as obtained from a reference measurement is a 3×3 matrix. The map obtained from the object measurement is similar but the terms are denoted b_{ij} as opposed to a_{ij} .

As each of the elements within a source detector map represent the number of photons detected the error on each element is taken to be Poisson, that is to say

$$\Delta a_{ij} = \sqrt{a_{ij}} \quad (3.14)$$

This is discussed further in §3.3.5.3.

In the following calculations two standard error propagations are assumed. Firstly that if $Z = A \pm B$ then

$$\Delta Z = \sqrt{(\Delta A)^2 + (\Delta B)^2} \quad (3.15)$$

and that if $Z = A \times B$ or $Z = A \div B$ then

$$\Delta Z = Z \times \sqrt{\left(\frac{\Delta A}{A}\right)^2 + \left(\frac{\Delta B}{B}\right)^2} \quad (3.16)$$

The only exception to the latter rule occurs when individual elements of a source detector map are scaled, by a factor L_i , to mimic the effect of a variation between source intensities. In this instance a new Poisson error is calculated from the new number of photons rather than propagating the Poisson error of the original value (i.e. the error on $L_i \times a_{ij}$ is taken to be $\sqrt{L_i a_{ij}}$ rather than $L_i \times \sqrt{a_{ij}}$). This is important. Suppose that the original errors are propagated and the total detected intensity, I , reaching a detector from two sources emitting different amounts of light are found such that

$$I = L_1 a_{1j} + L_2 a_{2j} \quad (3.17)$$

And the error on I , ΔI is

$$\Delta I = \sqrt{(L_1 \sqrt{a_{1j}})^2 + (L_2 \sqrt{a_{2j}})^2} \quad (3.18)$$

It can be shown that the percentage error on I is minimised when $L_1 = L_2$ (see appendix one). This is true irrespective of the number of terms (sources). The percentage error on I (and any ratio of ‘reference I ’ to ‘object I ’) is minimised when all sources are illuminated equally. This is not the case if the error on each is taken to be $\sqrt{L_i a_{ij}}$, allowing optimal patterns to be found. The result of the latter approach is realistic. Experimentally the uncertainty on I would reduce the larger I became. If a greater proportion of the light emitted by one source reached the detector than that from another then I would be increased, and its uncertainty decreased, by increasing the power of the first source.

Firstly two vectors are defined, reference total (RT) and object total (OT), representing the total amount of light detected at each detector during the reference and object measurements respectively.

$$RT = \left[\sum_{i=1}^3 a_{i1}, \sum_{i=1}^3 a_{i2}, \sum_{i=1}^3 a_{i3} \right] \quad (3.19)$$

$$OT = \left[\sum_{i=1}^3 b_{i1}, \sum_{i=1}^3 b_{i2}, \sum_{i=1}^3 b_{i3} \right] \quad (3.20)$$

Also define two vectors ΔRT and ΔOT whose elements represent the error on each of the values in RT and OT .

$$\Delta RT = \left[\sqrt{\sum_{i=1}^3 \Delta a_{i1}^2}, \sqrt{\sum_{i=1}^3 \Delta a_{i2}^2}, \sqrt{\sum_{i=1}^3 \Delta a_{i3}^2} \right] = \left[\sqrt{\sum_{i=1}^3 a_{i1}}, \sqrt{\sum_{i=1}^3 a_{i2}}, \sqrt{\sum_{i=1}^3 a_{i3}} \right] \quad (3.21)$$

$$\Delta OT = \left[\sqrt{\sum_{i=1}^3 b_{i1}}, \sqrt{\sum_{i=1}^3 b_{i2}}, \sqrt{\sum_{i=1}^3 b_{i3}} \right] \quad (3.22)$$

Next a source vector, L , is introduced. This represents the factors by which each source's power is varied. The modified versions of the above vectors are denoted RT_M , OT_M , ΔRT_M and ΔOT_M . For clarity only RT_M and ΔRT_M are shown below.

$$RT_M = \left[\sum_{i=1}^3 L_i a_{i1}, \sum_{i=1}^3 L_i a_{i2}, \sum_{i=1}^3 L_i a_{i3} \right] \quad (3.23)$$

$$\Delta RT_M = \left[\sqrt{\sum_{i=1}^3 L_i a_{i1}}, \sqrt{\sum_{i=1}^3 L_i a_{i2}}, \sqrt{\sum_{i=1}^3 L_i a_{i3}} \right] \quad (3.24)$$

Next the originally obtained ratio values at each detector (R) as well as the modified values that would result from a particular pattern of illumination (R_M) are found.

$$R = \frac{RT}{OT} = \left[\frac{\sum_{i=1}^3 a_{i1}}{\sum_{i=1}^3 b_{i1}}, \frac{\sum_{i=1}^3 a_{i2}}{\sum_{i=1}^3 b_{i2}}, \frac{\sum_{i=1}^3 a_{i3}}{\sum_{i=1}^3 b_{i3}} \right] \quad (3.25)$$

$$R_M = \frac{RT_M}{OT_M} = \left[\frac{\sum_{i=1}^3 L_i a_{i1}}{\sum_{i=1}^3 L_i b_{i1}}, \frac{\sum_{i=1}^3 L_i a_{i2}}{\sum_{i=1}^3 L_i b_{i2}}, \frac{\sum_{i=1}^3 L_i a_{i3}}{\sum_{i=1}^3 L_i b_{i3}} \right] \quad (3.26)$$

The error on R_M , ΔR_M , can also be found.

$$\Delta R_M = \left[\frac{\sum_{i=1}^3 L_i a_{i1}}{\sum_{i=1}^3 L_i b_{i1}} \times \sqrt{\frac{1}{\sum_{i=1}^3 L_i a_{i1}} + \frac{1}{\sum_{i=1}^3 L_i b_{i1}}}, \dots, \dots \right] \quad (3.27)$$

Now each of the values of R_M (and associated ΔR_M) must be ‘normalised’ by an appropriate scaling factor, F , to allow for the fact that each source is not illuminated to an equal extent. This restores the modified ratio, R_M , to the original value obtained with equal illumination at each source, R . Without this normalisation the shape of a profile can be arbitrarily distorted. Note that this normalisation is completely different to that discussed in the earlier critique of Serdaroglu’s study (Eq. 3.13). Its purpose is not to constrain the source power but allow for the change in the ratio value seen at each detector due to the uneven illumination of sources.

$$F = \frac{R}{R_M} = \left[\frac{\left(\frac{\sum_{i=1}^3 a_{i1}}{\sum_{i=1}^3 b_{i1}} \right)}{\left(\frac{\sum_{i=1}^3 L_i a_{i1}}{\sum_{i=1}^3 L_i b_{i1}} \right)}, \dots, \dots \right] \quad (3.28)$$

Now the normalised value of ΔR_M , $N\Delta R_M$, is found through element by element multiplication of ΔR_M by F . Following simplification this gives

$$N\Delta R_M = \left[\frac{\sum_{i=1}^3 a_{i1}}{\sum_{i=1}^3 b_{i1}} \times \sqrt{\frac{1}{\sum_{i=1}^3 L_i a_{i1}} + \frac{1}{\sum_{i=1}^3 L_i b_{i1}}}, \dots, \dots \right] \quad (3.29)$$

Note that, unless all $L_i = 1$, this will NOT be equal to the error on R , ΔR . The errors on the ratio values do not return to what they were.

At the beginning of this section the signal at each detector was defined to be the modulus of the difference of its calculated ratio, R , from one. As such the SNR at each point on a profile is given by

$$SNR = \frac{|R-1|}{N\Delta R_M} = \left[\frac{\left| \left(\frac{\sum_{i=1}^3 a_{i1}}{\sum_{i=1}^3 b_{i1}} \right) - 1 \right|}{\left(\frac{\sum_{i=1}^3 a_{i1}}{\sum_{i=1}^3 b_{i1}} \sqrt{\frac{1}{\sum_{i=1}^3 L_i a_{i1}} + \frac{1}{\sum_{i=1}^3 L_i b_{i1}}} \right)}, \dots, \dots \right] \quad (3.30)$$

The objective function, SNR_{max} , whose value must be maximised is

$$SNR_{max} = \sum_{j=1}^3 SNR(j) = SNR(1) + SNR(2) + SNR(3) \quad (3.31)$$

The second objective function, SNR_{equal} , whose value must be minimised is

$$SNR_{equal} = |SNR(1) - SNR(2)| + |SNR(2) - SNR(3)| + |SNR(3) - SNR(1)| \quad (3.32)$$

Clearly the value of the SNR at each point can be made arbitrarily large by increasing the size of the elements of L_i . For this reason these functions must be optimised within the constraint that only a finite total source power can be utilised. Equally the power emitted by each source must be greater than or equal to zero. These restrictions lead to the constraints that

$$L_i \geq 0 \text{ for all } i \quad (3.33)$$

and that

$$\sum_{i=1}^3 L_i = 3 \quad (3.34)$$

3.3.1.2. CNR based objective functions

The CNR between two points or regions with values A and B is commonly defined as

$$CNR = \frac{|A - B|}{\sqrt{\Delta A^2 + \Delta B^2}} \quad (3.35)$$

Continuing to use the notation denoted in the previous section it follows that the CNR between two adjacent points on a profile can be defined as

$$CNR(m) = \frac{|R(m) - R(m+1)|}{\sqrt{(N\Delta R_M(m))^2 + (N\Delta R_M(m+1))^2}} \quad (3.36)$$

where $R(m)$ denotes the m^{th} element of the vector R . Note that m takes values from 1 to one less than the number of detectors. Two objective functions based upon CNR were investigated. The first CNR based objective function, CNR_{\max} , must be maximised. This maximises the sum of the CNRs between adjacent points.

$$CNR_{\max} = \sum_{m=1}^2 CNR(m) \quad (3.37)$$

The second, CNR_{equal} , aims to make adjacent CNR values as similar to one another as possible. This is achieved upon minimisation of the function

$$CNR_{equal} = \sum_{m=1}^x |CNR(m) - CNR(m+1)| \quad (3.38)$$

Note that x is equal to the number of detectors less two in the above sum. Unlike SNR_{equal} , which aimed to make all SNRs more similar to one another, CNR_{equal} only aims to make adjacent CNR values as similar as possible. Imagine several adjacent points. Equalising the CNR between the first and second points with that between the second and third would be of benefit. In this way the positions of the first and third points, relative to the second point, would be known with equal accuracy. Conversely there would be relatively little benefit in equalising the CNR between the first and second points with that between the first and tenth. The clarity of the profile is not as dependent on the position of the tenth point, relative to the first, being known accurately. The values of both objective functions were optimised within the same constraints as the SNR based objective functions (Eqs. 3.33 & 3.34).

3.3.2. Finding optimal solutions of objective functions

It is important to note that all the techniques described below are based on finding a minimum. Finding a maximum simply requires a change of sign. Maximising the value of an objective function $f(L)$ is the same as minimising $-f(L)$.

Finding the minimum value for each of the defined objective functions is not straightforward. Each is a function of 15 dependent variables (the elements of the source vector, L) which are subject to constraints. Due to the number of variables it is not readily possible to plot and visualise these functions in order to find their global minimum.

Initially each of the objective functions were written into a script in Matlab 6.5. The source vector, L , that minimised each of these functions was then found using `fmincon`, an in-built constrained minimisation function within Matlab's optimisation toolbox. This allows the constraints on the values of the elements of L (Eqs. 3.33 & 3.34) to be imposed. `Fmincon` is a gradient-based function and will only find the local minimum. If

a function has several local minima this technique returns different solutions depending upon the initial starting guess for L used. This was sometimes observed when minimising SNR_{equal} or CNR_{equal} . In order to overcome this limitation the objective functions were also defined in Mathematica 7.0. This has in-built minimisation functions capable of finding both local and global minima (`findminimum` and `Nminimize` respectively). Matlab could always be made to return the same minimum values (and optimal source distributions) as Mathematica, though this occasionally required a couple of starting guesses to be tried.

3.3.3. Testing minimisation codes

In addition to verifying that the Matlab and Mathematica codes returned the same minima and source distributions as one another further tests were performed to verify that the minimisation codes worked correctly. These were performed using the modelled data, described in §3.3.4, verifying that the optimal patterns found appeared sensible and had the expected effect on the uncertainty of the profile points.

As a very final check the value of each objective function (for each profile) was calculated for 1000 randomly generated source vectors. Had any of the values calculated been lower than the minimum found then this would have indicated the optimisation had failed. For simplicity each source vector was assumed to consist of 15 integer numbers, each between 0 and 15, whose sum was 15 such that the required constraints were met. Each source vector was selected at random out of all possible configurations. Generating random vectors of this nature is not entirely trivial. The method used is discussed in appendix two. The value of the objective function obtained with each of these source vectors was found but they were not used as starting guesses in the minimisation codes. It can take Matlab or Mathematica a couple of minutes for the functions finding local minima to run and the function finding the global minima in Mathematica even longer. As a result this would have been too time consuming. Even if each minimisation took just one minute then running this 1000 times would have taken in excess of 16 hours per objective function per profile.

3.3.4. Generating modelled data

All modelled data were generated in Matlab. The model assumed the same slab geometry as previously described (figure 3.2). The main purpose of the modelled data was to demonstrate the concept of the profile plots, and the fact that their clarity was dependent upon the source illumination pattern, as well as to test the minimisation codes prepared in Matlab and Mathematica. In this work the emphasis has been placed on changes in absorption within homogeneously scattering media. For these reasons only absorption, not scatter, was modelled. Whilst the contrast of heterogeneities is dependent on the level of scattering this did not need to be realistic in the modelled data. Indeed the contrast of heterogeneities should increase the lower the level of scattering. Using profiles as clear as possible was beneficial for the purposes of demonstration and initial testing. Following this work experimental data were used. These were acquired using a realistically scattering phantom, described shortly in §3.3.5.1.1. In this manner the objective functions were evaluated using realistic experimental data having been tested using the modelled data.

Within the source to detector plane the distribution of absorption coefficients is specified by the user. Firstly a background absorption coefficient is specified. Secondly any number of absorbing heterogeneities can be introduced, their coordinates in the plane and absorption coefficients being specified. In order to calculate the source detector map for the specified absorption distribution the model assumes that

- A one dimensional array of 15 sources opposes 15 detectors on the opposite side of a 30mm thick slab
- The distance between the centres of adjacent sources (or detectors) is 8.5mm. This is as close together as it is physically possible to place the optodes of MONSTIR and the same as was used in the acquisition of experimental data (described shortly in §3.3.5.1.2)
- Each point source emits light isotropically over a hemisphere
- As well as being absorbed according to the specified distribution of absorption coefficients the light reduces in intensity with distance from the source as per the inverse square law
- Each detector has a circular active area 3mm in diameter, as is the case with the optodes of MONSTIR

- The slab is infinite in size (in the plane parallel to opposing surfaces) and no internal/boundary reflections occur

3.3.5. Acquisition of experimental data

3.3.5.1. Design and manufacture of slab phantom/interface

A photograph of the slab phantom and optode interfaces manufactured are shown in figure 3.3. Two main requirements were considered during their design. Firstly the phantom had to contain a removable cylindrical insert. This allowed the absorption in a central region of the phantom to be varied. This was either the same as that of the rest of the phantom (homogeneous) or three times more absorbing. The phantom was designed so as the insert could be moved without disturbing the optode interfaces to avoid different optical coupling conditions between the reference and object measurements. Secondly it was necessary that the position of the absorbing region could be clamped in several different positions relative to the central optodes in the two interface arrays. This was achieved by aligning the interface plates and phantom with one another using four corner bolts placed through one of five possible sets of holes. These were positioned such that the absorbing region aligned with either the central optode of each interface or those 2 or 4 positions to the left or right of the centre (figure 3.4). Acquiring data in these different positions should lead to profiles with different appearances, the maxima of the profile shifting to the left or right. Further details of the design and production of the phantom and interface plates are now given separately.

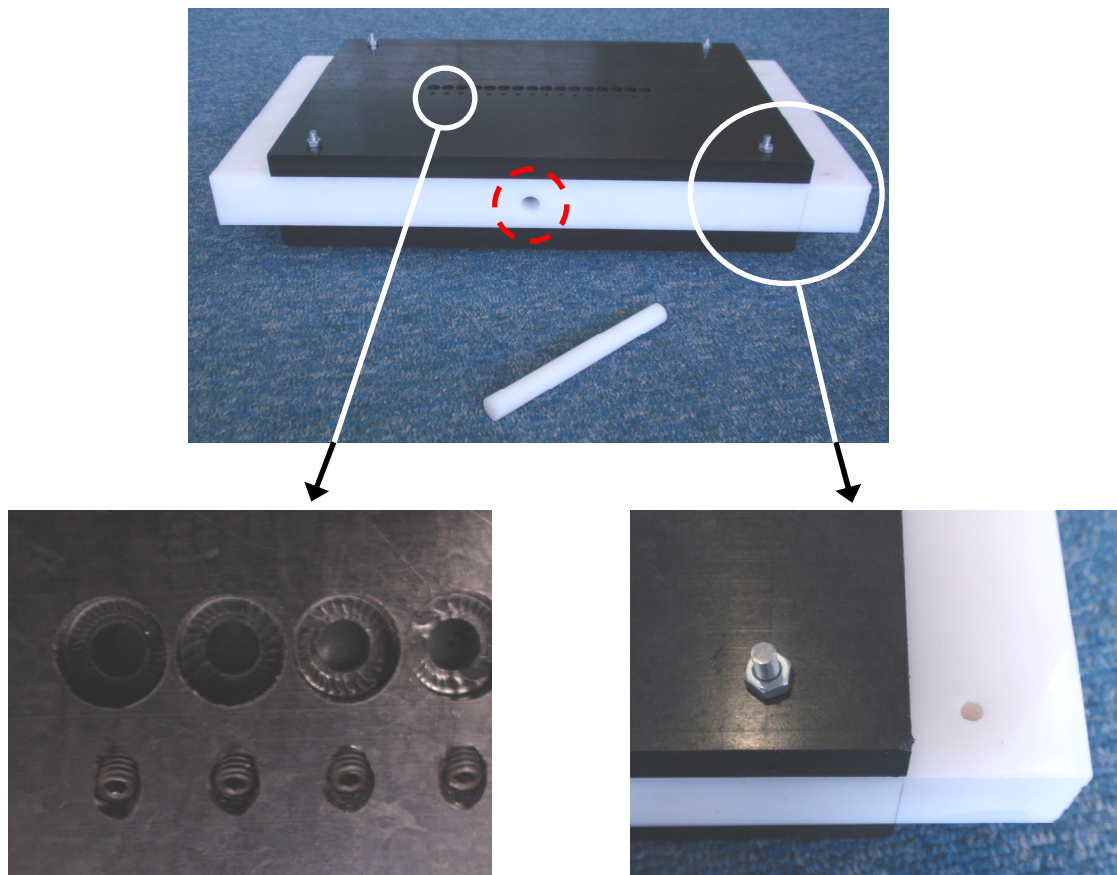


Figure 3.3. The slab phantom sandwiched between the two optode interfaces. The red circle highlights the hole into which the cylindrical insert is placed. The holes in the interface plate into which optodes are clamped are shown (bottom left). Also note that one of the fixing holes used to align the plates with the phantom can be seen (bottom right).

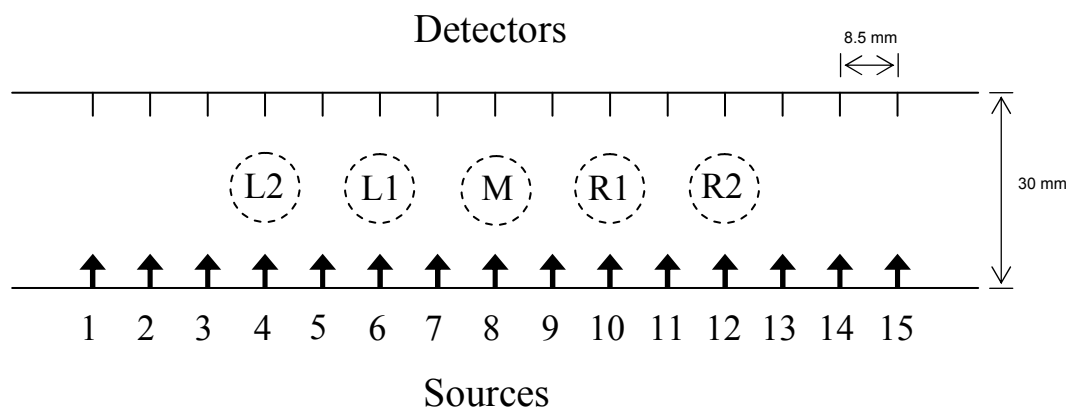


Figure 3.4. The five positions that the absorbing region can assume relative to the source and detector optodes. Both arrays of optodes were numbered sequentially. The centres of adjacent sources and adjacent detectors were spaced 8.5mm apart.

3.3.5.1.1. Slab phantom

The slab phantom was made from clear casting polyester resin (Alec Tiranti Ltd., London). This is a well characterised and widely used optical phantom material (Enfield et al 2007, Firbank and Delpy 1993, Pogue and Patterson 2006). The background optical properties of the slab were chosen so as to be realistic of healthy breast tissue, the transport scatter and absorption coefficients taking values of 0.85 ± 0.05 and $0.005 \pm 0.0005 \text{ mm}^{-1}$ respectively. A detailed discussion of breast tissue's optical properties can be found later in §4.3.2. The transport scatter coefficient of the resin was adjusted by adding Super White pigment (Alec Tiranti Ltd., London). This has previously been measured to have a transport scatter coefficient of 800 mm^{-1} prior to dilution in resin (Hebden 2009). The absorption coefficient is adjusted by adding a near-infrared dye concentrate, a suspension of Pro-jet 900NP (Avecia Inc., USA) in MY753 araldite resin (Aeropia Ltd., Crawley). Unfortunately the old batch of suspension, whose undiluted absorption coefficient had been characterised, had run out. A new batch of concentrate had to be produced and characterised. The details of this characterisation are given in appendix three. The absorption coefficient of the new batch of Pro-jet concentrate was measured to be 21 mm^{-1} at 800 nm.

The slab was produced by casting the resin into a rectangular polypropylene mould (to which the resin does not adhere). The final dimensions of the slab were to be $30 \times 19 \times 3 \text{ cm}$. The mould was slightly larger such that the slab could be machined down to size accurately. The resin cures exothermically on combination with a catalyst. Casting such a large volume in one attempt is not possible. The resin becomes so hot that it boils and many bubbles, that would alter the optical properties of the slab, are introduced. To avoid this the entire volume of resin, Pro-jet concentrate and Super White pigment were first mixed together without any catalyst. Five 500 g batches of this mixture were then mixed with catalyst and poured into the mould at 15 minute intervals to one another. This allows just enough time for heat dissipation that boiling is avoided. If the batches are poured at greater intervals then one batch tends to gel before the next is added. 'Vault lines' can appear between consecutive layers, again adversely affecting the supposed homogeneity of optical properties. Once hardened a radiograph of the slab was acquired to verify that it did not contain any bubbles that could adversely effect its optical properties.

A small amount of leftover resin, Pro-jet concentrate and Super White mixture was used to cast the cylindrical insert for the phantom. This was cast within a boiling tube in two stages. First a little resin was mixed with an appropriate quantity of extra Pro-jet concentrate so as to produce a 3 fold increase in absorption (a modified absorption coefficient of 0.015 mm^{-1}). This mixture was then mixed with catalyst and cast in the base of the tube. The following day the tube was filled with more of the leftover resin/catalyst but without any added Pro-jet concentrate.

Having cured at room temperature for several days the slab and cylindrical insert were placed in an oven at 60°C for 6 hours. This causes further hardening, making them easier to machine. The slab was then machined to size and the holes for the interface bolts as well as the hole for the cylindrical insert were drilled out. The cylindrical insert was machined down to a 10 mm diameter and cut to length such that the first 10 mm of one end of the rod had an absorption 3 times greater than the rest. When fully inserted the absorbing region of the rod lies directly beneath the optode arrays of the interface plates. Whilst I prepared the mould and cast the slab the machining was outsourced. I prepared technical drawings describing my requirements and gave these to the workshop.

3.3.5.1.2. Interface plates

The interface plates were made out of black delrin (RS Components Ltd., Corby). To reduce the level of reflection occurring from the inner surface of each plate these were abraded, to a uniform matt finish, using an air abrasives kit. Sixteen optode holes were drilled into each plate, their centres spaced along a single line at 8.5 mm to one another. This is as close a spacing as can be achieved, maximising the spatial resolution obtained along this line. Spacing the optodes out further would have been pointless. Even spaced this closely the largest source detector separation is sufficient that the detected light signal is very small. Further smaller holes drilled at 45 degrees to the surface of the plates and intersecting the optode holes allowed each optode to be clamped in place using a grub screw. A hole in each corner of the plates aligns with one of the five holes in each corner of the slab phantom. This allows the optodes to be clamped onto the phantom with a known position relative to the cylindrical insert.

3.3.5.2. Data acquisition

MONSTIR was more readily available than the group's CW system and was used for data acquisition. Only source detector intensity maps were required and it made no difference which type of system was used to obtain these. Prior to data acquisition with MONSTIR the appropriate variable optical attenuator (VOA) setting for each source detector pair is normally determined through an automated process (Schmidt et al 2000). The dynamic range of intensities incident upon the detectors is very large, detectors close to a given source being exposed to orders of magnitude more light than those further away. In order to avoid damage to the photomultiplier tubes (PMTs) a VOA is positioned between each detector's fibre bundle and the relevant PMT. The VOA consists of a number of variably sized pinhole apertures mounted on a stepper motor. As sources are illuminated one after the other the appropriate level of attenuation can be selected at each detector for each source illumination. Unfortunately the VOAs can introduce an uncertainty of up to 4% in the intensities measured (Jennions 2008). This is because the VOAs do not return to exactly the same position relative to the fibres within the detector bundle each time. A new VOA design using a circular disc of x-ray film with differently irradiated segments and therefore different optical densities will alleviate this problem in the future but is not yet in use. The chosen objective functions rely on the fact that changes in intensity detected are solely due to changes in absorption within the slab phantom. It was clearly preferable to minimise changes due to any other effects such as error in VOA alignment. For this reason a novel approach was taken to data acquisition allowing the use of the VOAs to be eliminated.

For each source detector pair only one of two VOA settings was allowed – fully closed (no pinhole) or fully open (pinhole diameter greater than that of detector fibre bundle). In these configurations intensity variations due to alignment with the fibre are almost completely eliminated. Instead of relying upon the VOAs for attenuation this was achieved by placing an appropriate optical density filter in the path of the source beam for each source detector pair. The optical density (OD) filter required for each of the 225 source detector pairs was determined manually as shown in figure 3.5.

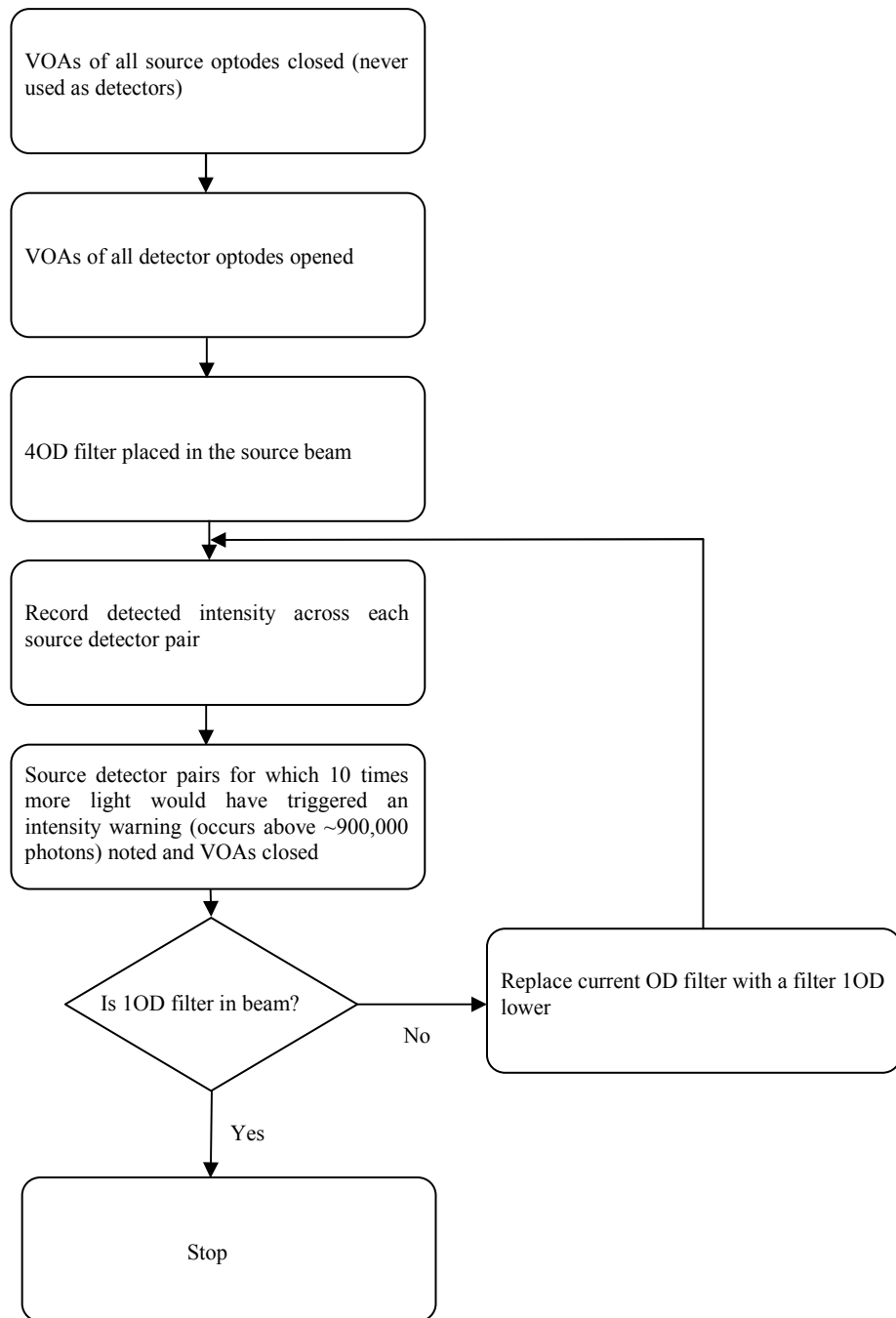


Figure 3.5. The iterative process used to determine the appropriate optical density (OD) filter for each source to detector acquisition

Through this process each source detector pair was assigned a value of either 0, 2 or 4 OD, with which the VOA could safely be opened fully during data acquisition. Note that if 1 or 3 OD was originally deemed to be appropriate then the final level of filtration used was 2 or 4 OD respectively. This is justified in the next paragraph. Three separate pairs of acquisitions were next made as follows:

- 1a) 4 OD filter ‘reference’ (homogeneous absorption)
- 1b) 4 OD filter ‘object’ (cylindrical insert turned around – 3 times absorption)
- 2a) 2 OD filter ‘object’
- 2b) 2 OD filter ‘reference’
- 3a) No filter ‘reference’
- 3b) No filter ‘object’

During each of these acquisition pairs the VOAs were only opened for the detectors assigned the OD in use. Note that the order of acquisition meant that filters were not moved between the acquisition of the reference and object datasets. This is discussed further in §3.3.5.3. The entire set of acquisitions was taken as quickly as possible (within 15 minutes). In this way differences in intensity due to temporal drifts in the laser power, both within and between pairs, were minimised. This is the reason that only 3 pairs of acquisitions were made (rather than five including those using 1 and 3 OD filters). Similar sets of data were acquired for all five of the possible optode to insert alignments.

Ordinarily MONSTIR acquires TPSFs for each source detector pair at both 780 and 815 nm. On this occasion the 815 nm source was blocked off so that all of the photons detected were from the 780 nm source. In this way the signal (number of counts) in the 780 nm TPSF is maximised, double what it would have been had an 815 nm TPSF also been acquired, for a given acquisition period. This is due to the maximum count rate capability of the PMTs.

3.3.5.3. Data processing

Each experimental acquisition results in one TPSF per source detector pair (225 TPSFs in total with 15 sources and 15 detectors). Integrating each of these TPSFs allows the number of photons from each source reaching each detector to be found. Before this integration the average background noise in each temporal bin was calculated for, and then subtracted from, each TPSF (figure 3.6). Following subtraction the baseline fluctuates around 0. Upon integration the small positive and negative values largely cancel one another out so as the number of photons found is truly representative of the signal rather than the signal and background noise. The above subtraction was performed using MONSTIX, a programme developed within the department to process the TPSFs generated by MONSTIR.

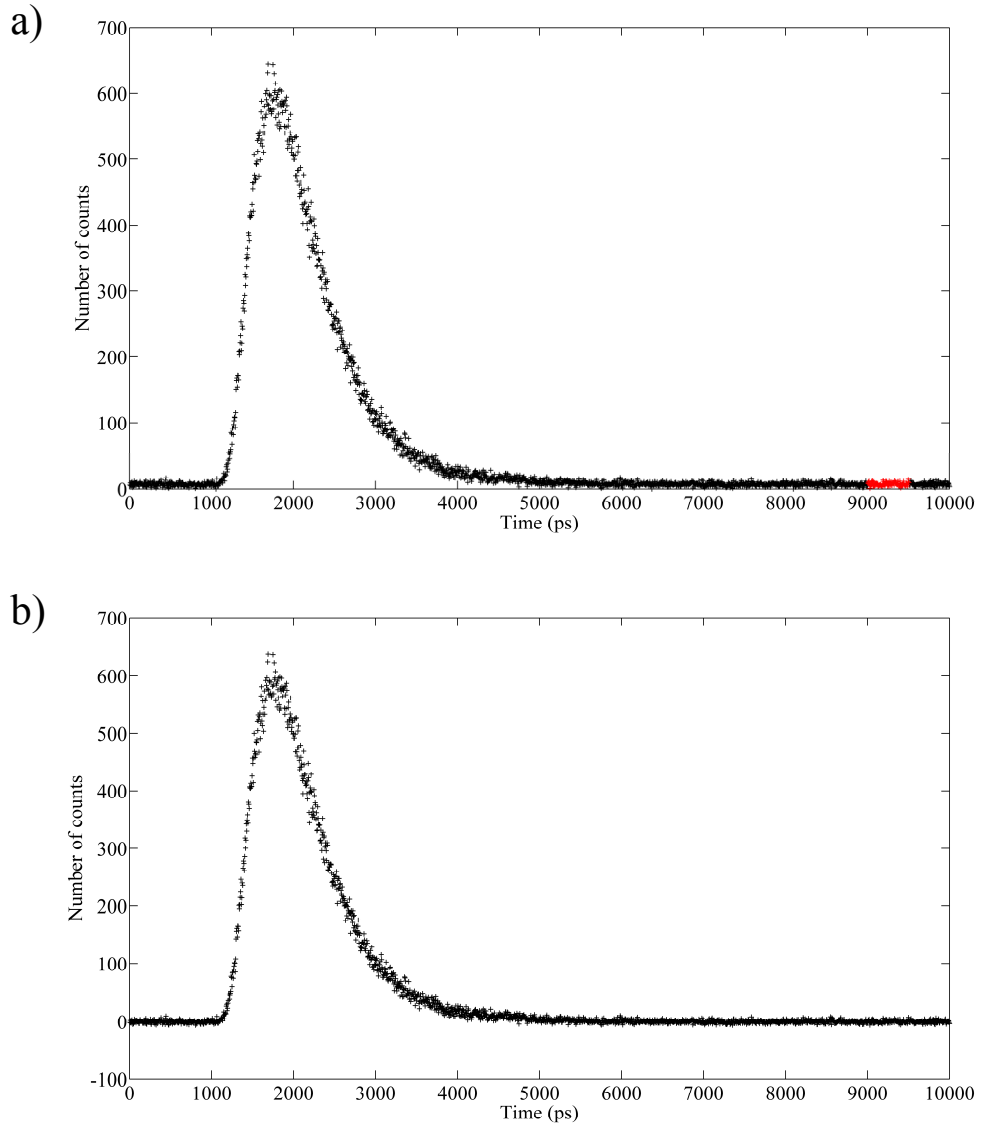


Figure 3.6. a) An example of a TPSF with background noise. The average background noise of each TPSF was calculated over a region in the extreme tail (marked red) b) following subtraction the TPSF has a zero baseline.

Whilst combining all 225 intensity values for a particular acquisition into a single source detector map each of these had to be scaled to account for the level of attenuation used (either 0, 2 or 4 OD) such that all of the intensities became directly comparable. To calculate the scaling factor required for each level of attenuation MONSTIR's source fibre was directed into the aperture of a power meter and ten power measurements made with each filter (level of attenuation) in the beam. For the case without any filter the readings were taken at 5 second intervals. For those with a filter they were taken as quickly as possible in time, the appropriate filter being removed and replaced between each measurement. The mean and standard deviation of the power recorded in each case is displayed in table 3.2. All intensity values acquired using this level of attenuation were corrected through multiplication by the scaling factor shown.

Optical density filter used	Mean Power (μW) (3 s.f.)	Standard deviation (μW) (3 s.f.)	Scaling factor
0 (no filter)	4460	4.71	0.523/4460
2	47.1	.303	0.523/47.1
4	0.523	.015	1

Table 3.2. The scaling factors applied to the measured intensity values as calculated from mean power meter readings at each OD.

It should be noted that the objective functions proposed require that the error on each element of the source detector maps be known (Eq. 3.14). This was taken to be the square root of the intensity value obtained once the relevant scaling factor had been applied. Suppose that 100000 photons were recorded for a source detector pair before the 2 OD scaling factor of 0.011 was applied. In this case the element's final value is $100000 \times 0.011 = 1100$ and its error is $\sqrt{1100}$. Had the Poisson error of the originally detected intensity been propagated, making the error on the final value $0.011 \times \sqrt{100000}$, the optimisation of the objective functions would have been sensitive to the use of the OD filters and this had to be avoided. This filtering was only required due to the use of MONSTIR and intensity data acquired using other systems would not have been scaled in this manner. Note that this is a totally separate consideration from those concerning error propagation made earlier (following Eq. 3.18). It must also be noted that the uncertainties on the scaling factors were ignored. These allowed for variation in filter placement but the filters were not moved between the reference and object measurements for a given source detector pair. The inclusion of these errors leads to a significant over estimation of the overall errors. In any case the error on the scaling factors should largely cancel. Relative intensities are considered and the same scaling factor is applied to a given source detector pair's reference and object measurements.

In a very small number of cases the integrated intensity of a TPSF was calculated to be a small negative number. As this has no physical meaning such values were set to zero. This occurred on a few source detector pairs with very large separation where virtually no light was detected, just background noise.

3.4. Results

3.4.1. Un-optimised simulated and experimental profiles

Each objective function was tested on a variety of simulated and experimental datasets. Three simulated profiles were used. One of these was previously shown in figure 3.2 whilst the other two are shown in figure 3.7. These were produced using the previously described modelling code (§3.3.4). In all cases a source detector map was first calculated assuming the slab to be homogeneously absorbing and that each source was illuminated equally (simulated reference measurement). A second source detector map was then calculated allowing for the introduction of the absorbing region(s) shown (simulated object measurement).

Similar profiles as obtained from the experimental data sets are shown in figure 3.8. A profile is shown for each of the five possible alignments of the absorbing region with the optode array (as earlier illustrated in figure 3.4). Detectors 1, 12 and 15 have larger errors than the remaining detectors in all of the profiles. These detectors were poorer than the others, primarily due to fibre bundle damage, and thus detected fewer photons. Furthermore, because they were poor, two of these three detectors were placed in the end positions, where the least total light is detected due to geometry.

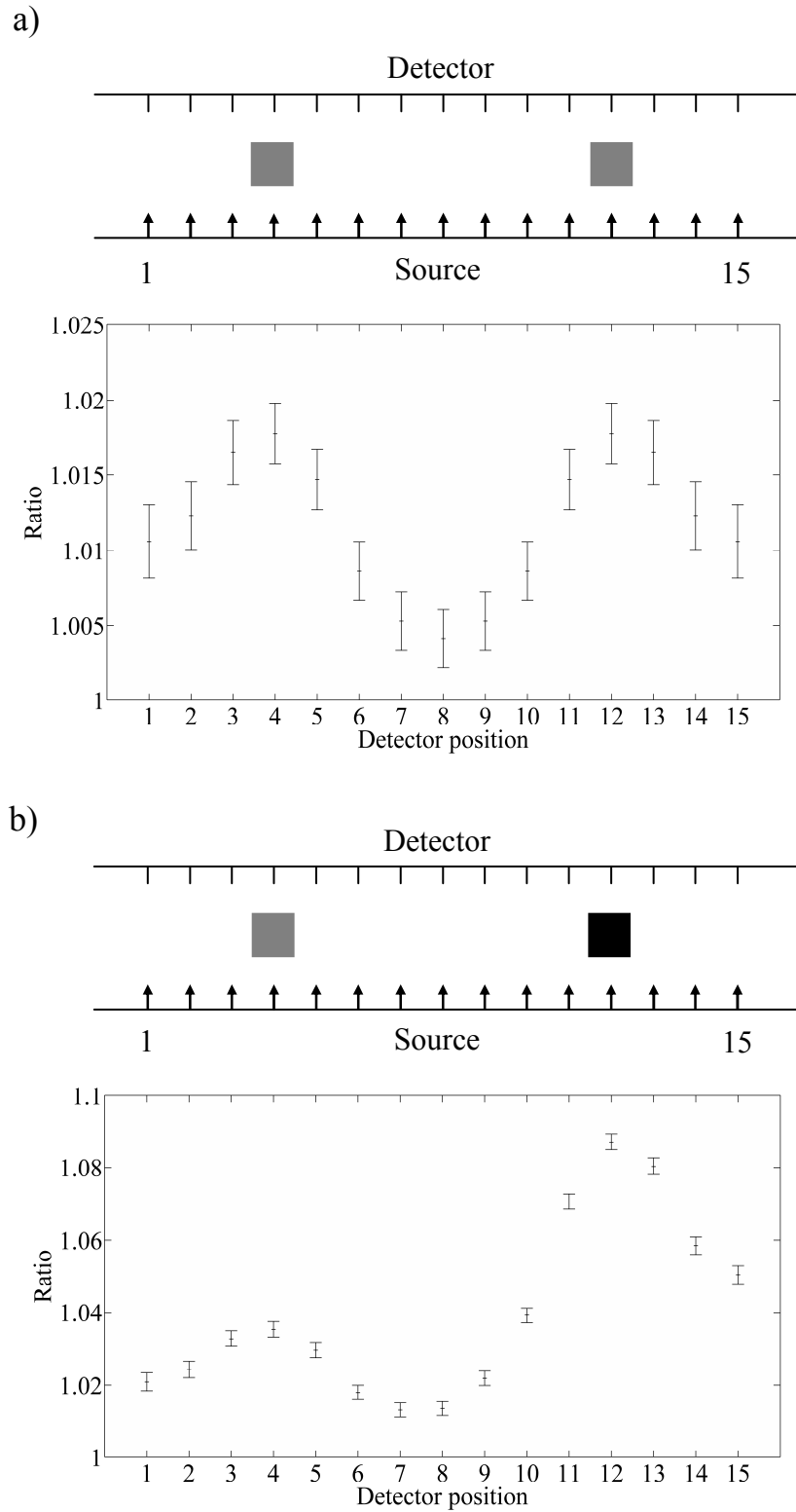


Figure 3.7 a) Profile obtained simulating two 1 cm^2 decentralised heterogeneities of equal absorption ($\mu_a = 0.015 \text{ mm}^{-1}$). b) Profile obtained simulating two heterogeneities of differing absorption to one another. One to the left ($\mu_a = 0.015 \text{ mm}^{-1}$) and one to the right ($\mu_a = 0.03 \text{ mm}^{-1}$). The background absorption coefficient of the slab was taken to be 0.005 mm^{-1} in both simulations. Error bars shown are calculated according to Eq. 3.27, with all $L_i = 1$.

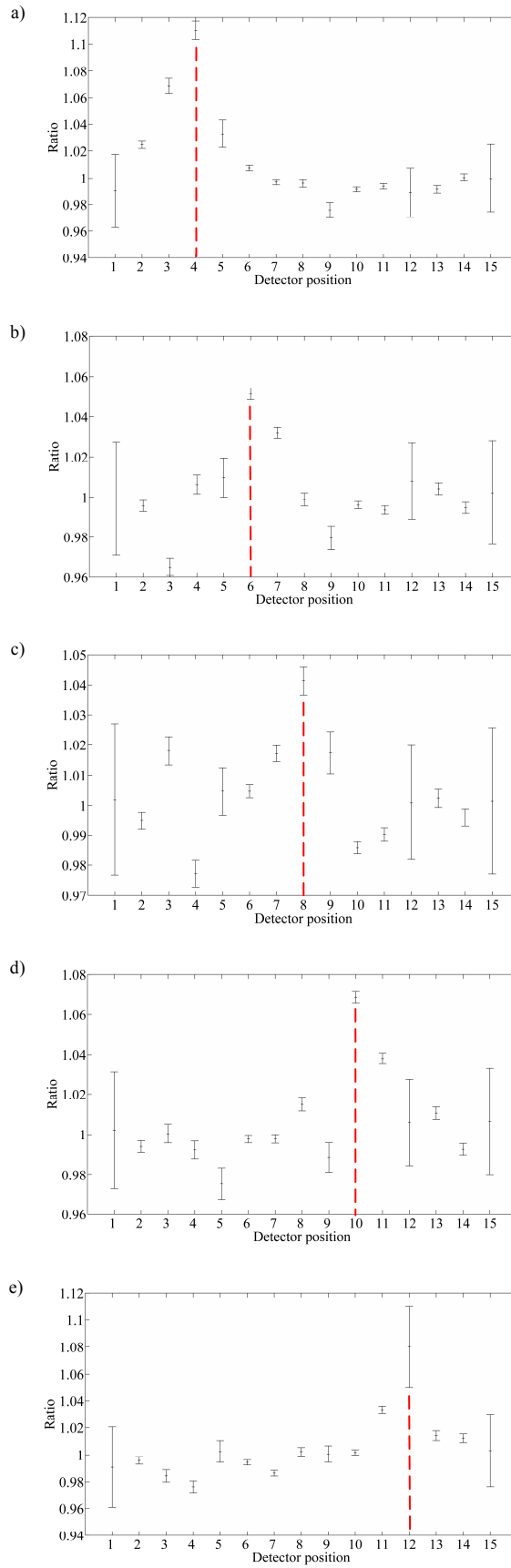


Figure 3.8. a-e) The experimentally obtained profile obtained with the absorbing region in each of the five possible positions (marked by the red dotted line). Note that the maximum of each profile demarks the position of the region as expected. Again error bars are calculated according to Eq. 3.27 with all $L_i = 1$.

3.4.2. SNR_{equal}

SNR_{equal} was designed to make the SNR (as defined in Eq. 3.30) of all of the points in a profile as equal to one another as possible. Though the function achieved this very effectively an unfortunate consequence was a relatively large reduction in the SNR of most points, the SNR increasing just a little at those remaining. Whilst the SNRs became more similar the average SNR was significantly reduced. A typical example, obtained upon optimisation of the simulated profile for the slab containing two regions of differing absorption, can be seen in figure 3.9. The optimal pattern found clearly channels the light into sources close to detectors whose SNR was originally relatively poor.

When run on the experimentally obtained profiles SNR_{equal} performed even more poorly. In the simulated profiles none of the points take a value very close to 1, defined as no signal by Eq. 3.30. However it can be seen that a number of the points in the experimental profiles do (figure 3.8). In this instance the optimal pattern found is to channel virtually all of the light into one source closest to detectors showing a very low signal. As the detectors on either end of the profiles tend to have a low signal (and the largest error bars) the optimal pattern found generally illuminated one of these end sources. Despite a reduction in the error (noise) the signal, and thus SNR, remains very poor. Simultaneously that at many of the other points is very significantly diminished. Due to the poor nature of this objective function it is not considered further.

3.4.3. CNR_{equal}

This objective function calculated the CNR between each pair of adjacent profile points. The illumination pattern that minimised the sum of the differences between adjacent CNR values was then found. In this way it was expected that the CNRs between adjacent points would become more equal to one another. Unfortunately this objective function suffered a similar downfall to that of SNR_{equal} . Whilst the differences between adjacent CNRs were reduced the average CNR between adjacent points was also reduced. This objective function is not considered further.

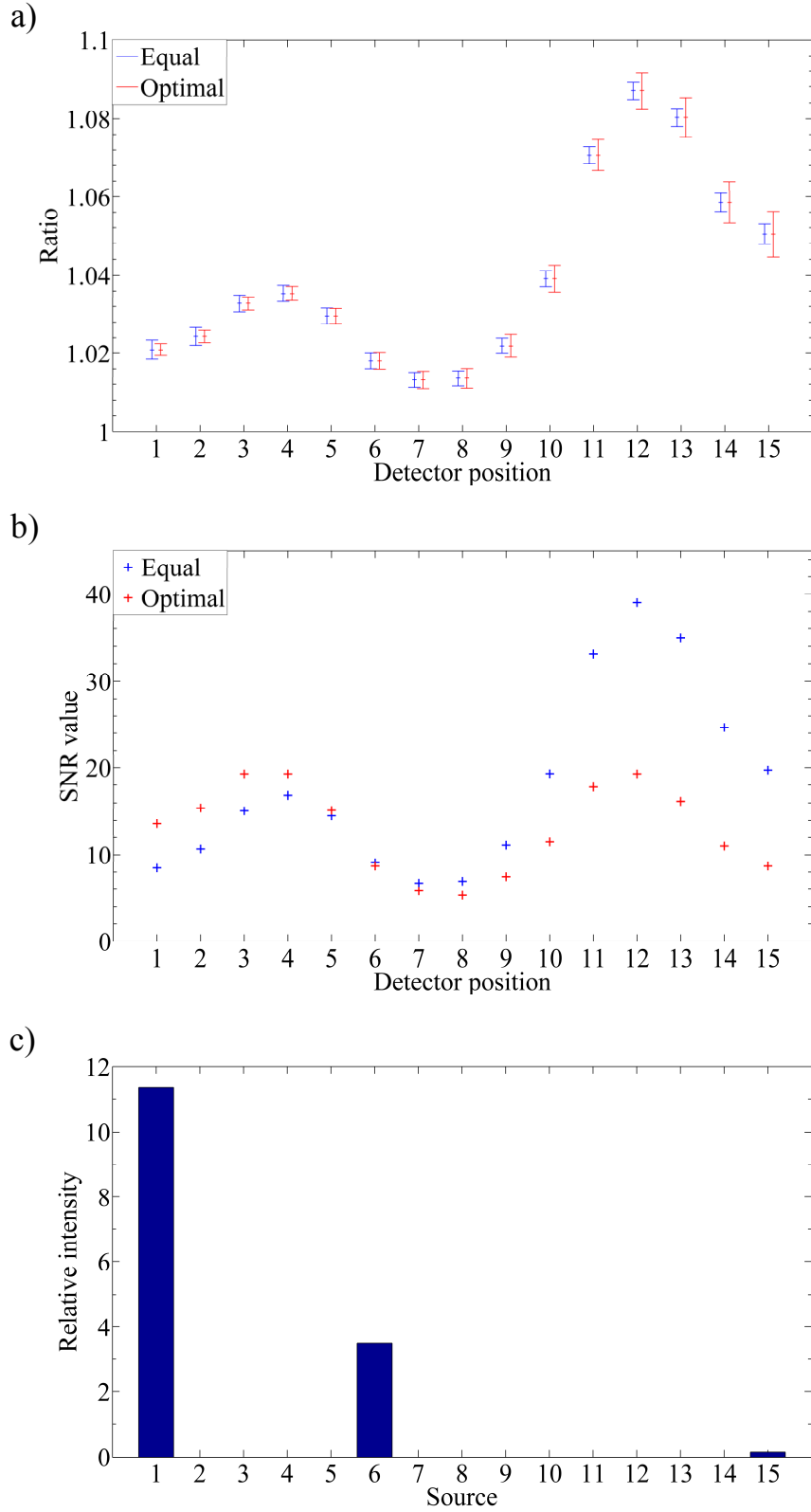


Figure 3.9. An example of the result of optimisation using SNR_{equal} . Simulated slab data for two heterogeneities of differing absorption is used. a) the original profile obtained with equal illumination at all sources (all $L_i = 1$) and that obtained using the optimal illumination pattern found. For clarity the two profiles are offset from one another by a little. b) on optimal illumination the SNRs of the points become more similar to one another but the average SNR also becomes much smaller. c) the optimal pattern of illumination found.

3.4.4. SNR_{max}

This objective function was designed to find the optimal pattern that maximised the sum of the SNRs across all of a profile's points. It appears that using an optimal pattern of illumination as returned by this objective function could significantly improve the average SNR of a profile's points. In contrast to the result obtained using SNR_{equal} the SNR increases at a significant number of points whilst decreasing relatively little at others. A typical result of maximising SNR_{max} can be seen in figure 3.10. Note that the optimal pattern found is asymmetrical even though the heterogeneity was centrally positioned. Recall that the signal at each detector was defined as the modulus of the difference of its calculated ratio value from one (Eq. 3.30). Accordingly detectors 3 and 4, to the left of the profile have a larger signal than those in similar positions to the right. This is the cause of assymetry, a consequence of noise in the experimentally acquired data. Table 3.3 shows the percentage improvement in the value of SNR_{max} upon optimisation, compared to that obtained when each source is illuminated equally, for each of the simulated and experimental data sets. The optimal patterns found are discussed further in §3.5.

Profile	Value of SNR_{max} with equal illumination of each source (0 d.p.)	Value of SNR_{max} upon optimal illumination of sources (0 d.p.)	% Improvement in SNR_{max}
Exp_L2	62	89	44
Exp_L1	54	78	44
Exp_M	45	56	24
Exp_R1	59	86	46
Exp_R2	45	53	18
Sim_S	101	118	17
Sim_Dea	84	87	4
Sim_Dda	270	297	10

Table 3.3. The % improvement in the value of SNR_{max} upon optimal illumination seen for each of the simulated and experimental profiles. Profiles: Exp_ denotes the experimental profile for the position indicated (refer to figure 3.4). Sim_ refers to simulated data (S = single blob, Dea = double equal absorptions, Dda = double different absorptions) (refer to figures 3.2 and 3.7).

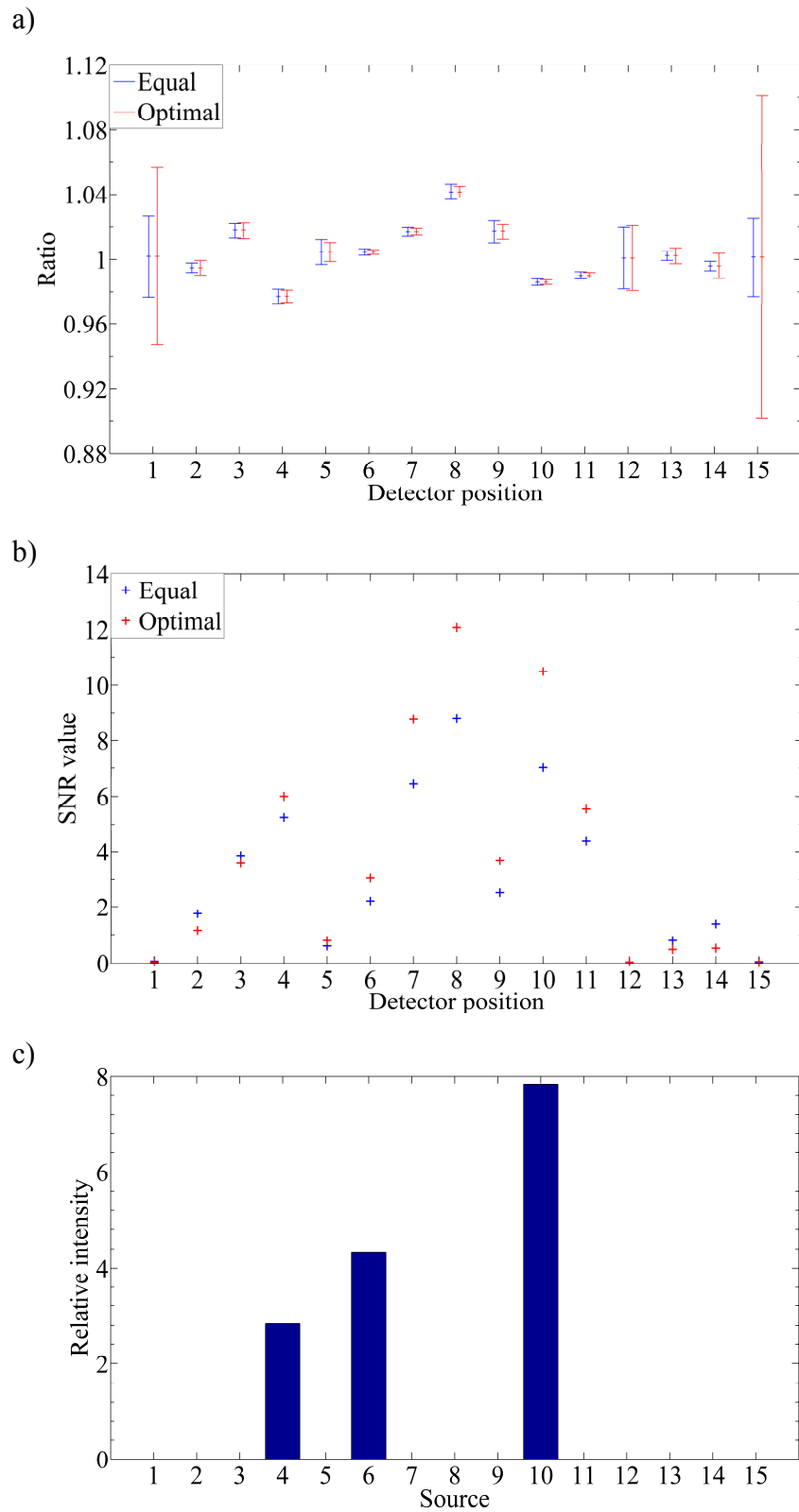


Figure 3.10. A typical example of the result of optimisation using SNR_{max} . The experimentally acquired profile with the centrally positioned heterogeneity is used. a) the original profile obtained with equal illumination of each source and that obtained using the optimal illumination pattern found. For clarity the two profiles are slightly offset from one another. b) on optimal illumination the SNR is substantially increased at detectors located in the centre, close to the heterogeneity. c) the optimal pattern of illumination found.

3.4.5. CNR_{max}

CNR_{max} was intended to maximise the sum of the CNR values between adjacent profile points. This objective function was found to work very effectively, increasing the CNR between adjacent points in the region of the heterogeneity. A typical result of this optimisation can be seen in figure 3.11. Table 3.4 shows the % improvement in CNR_{max} obtained upon optimal illumination, relative to that obtained when each source is illuminated equally, for each of the datasets. The optimal patterns found are discussed in §3.5.

Profile	Value of CNR_{max} with equal illumination of each source (0 d.p.)	Value of CNR_{max} upon optimal illumination of sources (0 d.p.)	% Improvement in CNR_{max}
Exp_L2	34	45	32
Exp_L1	40	54	35
Exp_M	33	42	27
Exp_R1	39	52	33
Exp_R2	29	37	28
Sim_S	19	22	16
Sim_Dea	14	15	7
Sim_Dda	49	56	14

Table 3.4. The % improvement in the value of CNR_{max} seen for each of the simulated and experimental profiles upon optimal illumination. Profiles are named as in table 3.3.

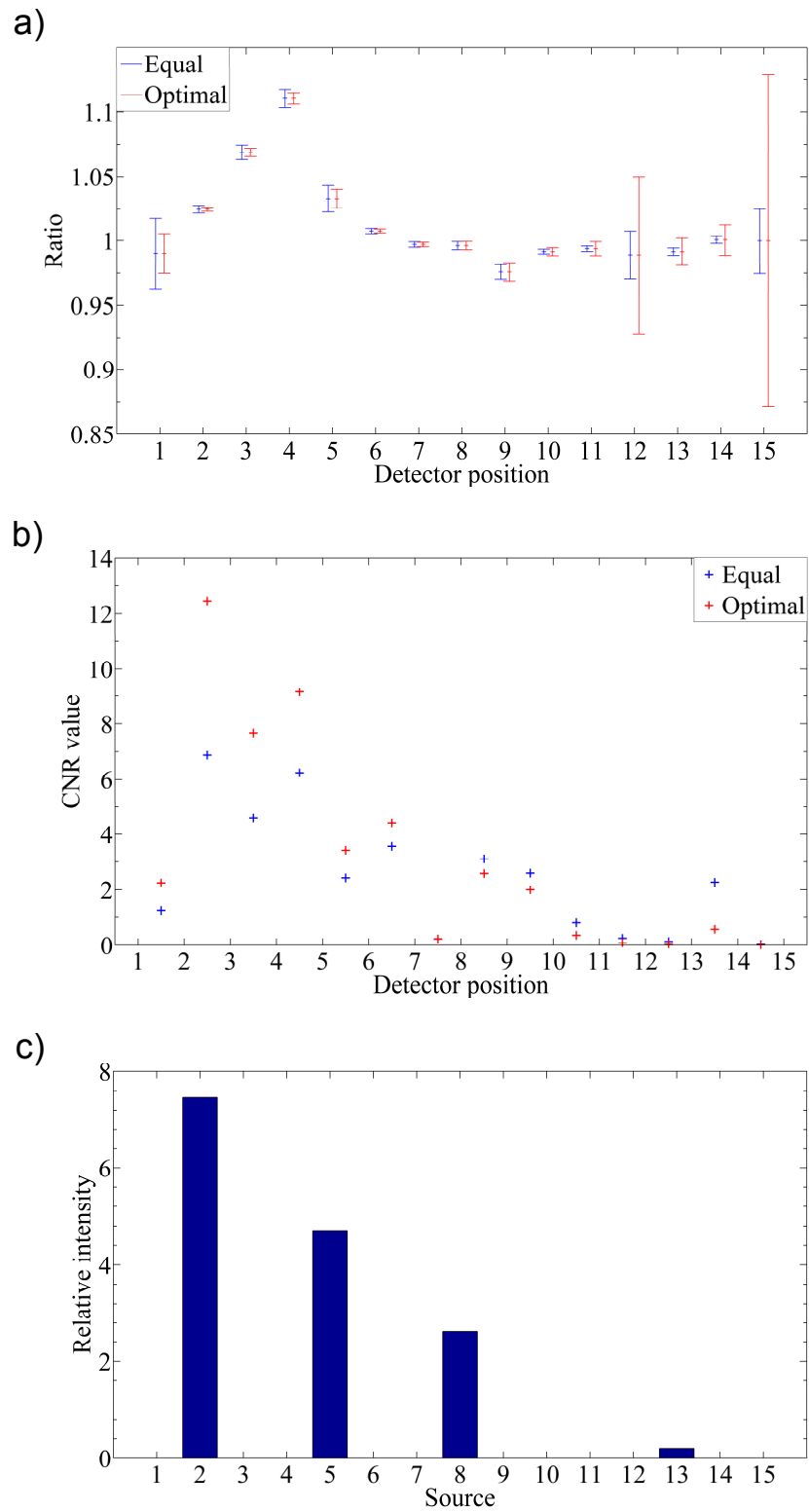


Figure 3.11. A typical example of the result of optimisation using CNR_{max} . The experimentally acquired profile with the heterogeneity positioned to the far left (position L2 in figure 3.4) is used. a) the original profile obtained with equal illumination of each source and that obtained using the optimal illumination pattern found. For clarity the two profiles are slightly offset from one another. b) Upon optimal illumination the CNR between adjacent points improves around the region of the heterogeneity. Note that values are plotted between detector positions as they represent CNR between adjacent detectors. c) the optimal pattern of illumination found.

3.5. Discussion

Of the four objective functions tested two of these, SNR_{max} and CNR_{max} , proved useful. Whilst SNR_{equal} and CNR_{equal} worked as intended the outcome of optimisation using these functions was not satisfactory. In attempting to make the SNR of, or the CNR between, profile points more similar the optimal patterns found tended to direct light toward sources close to detectors where very little signal or contrast was seen in the original profile so as to minimise noise in these areas. As a result very small improvements in SNR or CNR were seen in these regions whilst relatively large reductions were seen in areas of importance where large signals or contrasts had originally been observed.

SNR_{max} and CNR_{max} tended to work in exactly the opposite manner to SNR_{equal} and CNR_{equal} . These directed light toward regions where large signals or contrasts were present, improving the SNR or CNR yet further, whilst allowing the SNR or CNR to become even poorer in regions where it had been very poor before (due to lack of signal or contrast rather than the presence of noise). In circumstances where there is only one heterogeneity this is beneficial but it is important to note that this will have detrimental implications in other instances. If an object contains two regions of heterogeneous absorption, one much weaker than the other, then the detection of the lesser heterogeneity is likely to be sacrificed to improve the clarity of the relatively prominent heterogeneity further. This effect was observed when optimising SNR_{max} and CNR_{max} for the simulated profile containing two heterogeneities of unequal absorption. How best to overcome this limitation is not immediately apparent. In the future it may be necessary to set threshold values, of signal or contrast, to automatically identify points of interest within a profile. The objective functions could then be optimised within the constraint that these point's SNRs or CNRs should only be maintained or increased, never reduced. An alternative approach would be to use multiple optimal patterns, each designed to maximise the clarity of a particular region of interest. This would require the objective functions to be modified so as they could be steered toward optimisation of particular regions of a profile rather than the profile as a whole.

The optimal patterns found by SNR_{max} and CNR_{max} were sometimes relatively similar, though certainly not the same. This is not all that surprising because profile points with the largest signals (ratio value furthest from 1) are also likely to have a relatively large contrast relative to their adjacent points. In an attempt to determine whether one

objective function might be better than the other the size of the error bars on each point of a profile can be compared. Figure 3.12 shows the result of this comparison for one of the experimentally acquired datasets. Similar comparison of the other datasets demonstrated that neither objective function reliably outperformed the other, consistently resulting in smaller errors across the whole of profiles. Furthermore by far the largest differences were always seen on the two end detectors. As none of the datasets had an appreciable signal or contrast in these regions the size of the errorbars at these points, and any difference seen between objective functions in these regions, is probably of very little importance. In theory the two objective functions could be combined, with appropriate weighting, so that an optimal pattern that maximised both SNR and CNR as well as simultaneously possible could be found. In practice it is likely that the parameter of greatest interest would be selected and the appropriate optimal pattern used. Alternatively both patterns could be used, one after the other.

In this work the likely effect of using various source illuminations has been predicted through analysis of the source detector maps acquired when each source was illuminated equally. Whilst the error propagations used to do this were performed as well as possible the predicted outcomes are likely to be slightly different to those obtained experimentally. In future work these would have to be validated experimentally, data being acquired using the optimal patterns and the true outcomes being compared to those predicted. In addition there must be a noise threshold that the original profiles obtained, before optimisation, need to meet before they can be optimised. If the original profiles had been too noisy then the optimisations performed would have failed. The clearer the profile required the longer it would take to acquire. As a result determining the required threshold could prove very important. This would depend upon the object being imaged and it is possible that the threshold might need to be determined during acquisition of the source detector map.

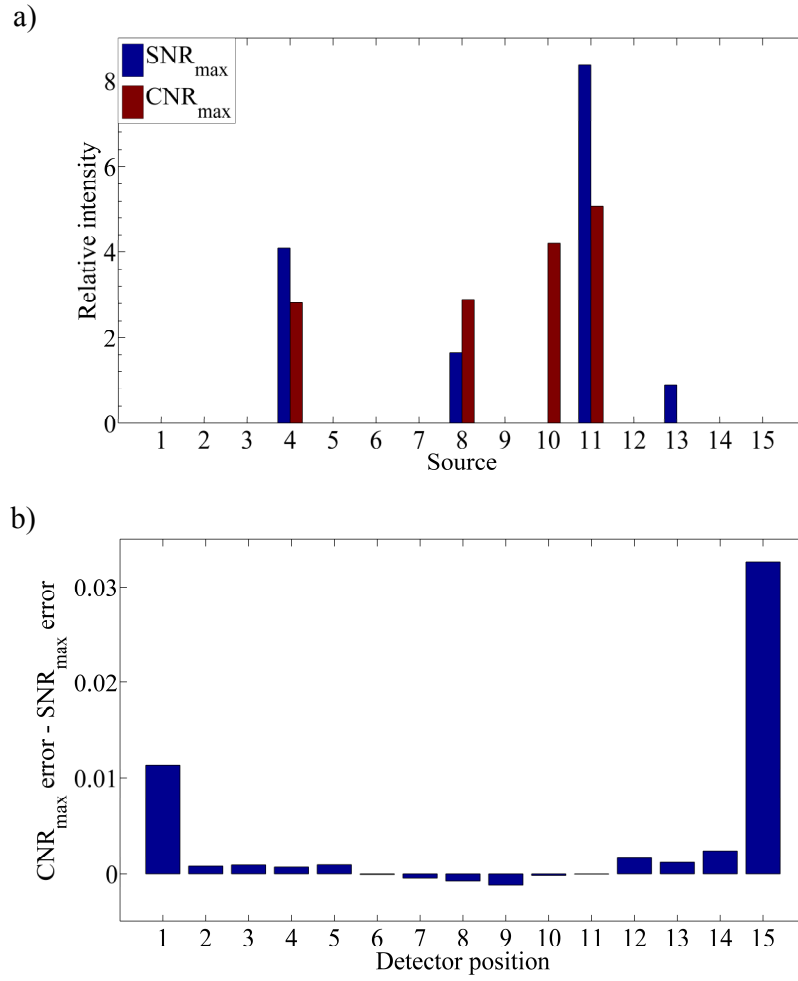


Figure 3.12. Results shown pertain to experimental data acquired with the heterogeneity positioned to the far right (position R2 in figure 3.4). a) The optimal patterns found upon maximisation of SNR_{max} and CNR_{max} . b) The differences between the errors, at each detector, of the optimised profiles obtained using the two optimal patterns shown in a). For this particular dataset most point's errors appear to be larger with CNR_{max} than SNR_{max} .

3.6. Conclusions

When performing combined optical and x-ray mammography the optical acquisition would be subject to a number of practical limitations. These include the need for the acquisition to be performed as quickly as possible and in the parallel plate geometry. Under such limitations it would be preferable to collect only intensity, and no time of flight, information. Purely intensity based measurements can be made more rapidly. For this reason a very simple method of visualising intensity data, in the form of profiles, in order to localise regions of heterogenous absorption has been presented. Furthermore proof of concept work was performed to demonstrate that, subject to certain constraints, optimal source distributions can be found in order to improve the visibility of optical heterogeneities when using this technique.

In this work the values of chosen objective functions, designed to quantify the quality of the profiles, were optimised within the constraint that a fixed total light power could be distributed among a number of sources in any manner. Different results would have been obtained had a different constraint been applied. The appropriate constraint is dependent upon the exact method of acquisition used. The above constraint would not necessarily apply to a traditional CW measurement. In a system illuminating all sources simultaneously each fibre could emit at the maximum permissible exposure for skin at the wavelength in question. Nonetheless limiting the total source power emitted across all fibres allows other modes of intensity data acquisition to be considered. A single source could be time multiplexed between different optodes, the time for which each was illuminated being informed by the above optimal patterns. The total acquisition time could be fixed, at say 5 seconds, and the period of each source's illumination calculated accordingly. Acquisition would still be much faster than that of a time domain measurement but fewer sources would be required. The total integrated intensity, at each detector, could be calculated over the entire acquisition. Such a system could be cheaper to produce than one using multiple sources.

Whilst the objective functions used in this work, and constraints imposed during their minimisation, are not necessarily perfect the potential benefits of optimising source power distribution are clear. Whilst four objective functions were proposed in this work many others could also be used. Notably the objective functions chosen were designed to maximise the acquisition according to the nature of the object. Other objective functions designed to maximise acquisition according to the nature of the system itself might also be found. The objective functions chosen in this work made a number of assumptions, for example that each detector had an unlimited dynamic range. An objective function designed around the system, as opposed to the object being imaged, would have allowed for such factors. Furthermore there is no reason that objective functions taking account of several different constraining factors, and aiming to optimise more than one parameter at a time, could not be designed. It is equally possible that several optimal patterns, each optimising a particular parameter, might be used in turn. As the total acquisition time available would be limited this could be divided up between the number of optimal patterns to be used.

Chapter Four

An elastically compressible phantom material with mechanical, x-ray attenuation and optical properties equivalent to breast tissue

This chapter combines the work described in two previous publications and bears close resemblance to these. The work characterising the mechanical and x-ray attenuation properties of a novel phantom material was first published in *Physics in Medicine and Biology* (Price et al 2010b). Later I wrote and presented a paper at SPIE Medical Imaging (Price et al 2010a). This detailed the characterisation of the phantom material's optical properties.

All the work presented in this chapter was performed solely by me under the guidance of my supervisors. I wrote the entirety of both papers, also under their guidance. The only other person on either author list was Dr L.T. Tan who works in the Department of Civil and Environmental Engineering at UCL. Dr Tan allowed me access to their Instron, the testing device used to characterise the mechanical properties of the phantom material. Whilst Dr Tan showed me how to use this and entered into useful discussions about the results, I acquired and analysed all the data presented.

4.1. Chapter overview

A novel phantom material produced by freezing and thawing a solution of polyvinyl alcohol (PVAL) in ethanol and water to create a solid, yet elastically compressible, gel is described. The x-ray attenuation, mechanical and optical properties of these gels are compared with published measurements of breast tissue. Gels with PVAL concentrations from 5 to 20% w/v were produced. The linear x-ray attenuation coefficients of these gels range from 0.76 to 0.86 cm⁻¹ at 17.5 keV, increasing with PVAL concentration. These values are very similar to the published values of breast tissue at this energy, 0.8 to 0.9 cm⁻¹. Under compression cancerous breast tissue is approximately ten times stiffer

than healthy breast tissue. The Young's moduli of the gels increase with PVAL concentration. Varying the PVAL concentration from 7.5 to 20% w/v produces gels with Young's moduli from 20 to 220 kPa at 15% strain. These values are characteristic of normal and cancerous breast tissue respectively. Adding very small quantities of titanium dioxide powder to the optically non-scattering and colourless gels allows their transport scatter coefficient to be varied within the range 0.6 to 1.5 mm⁻¹. The transport scatter coefficient of both healthy and cancerous tissues fall well within this range, typically having values of 0.85 and 1.16 mm⁻¹ respectively.

4.2. Introduction

Radiographically tissue equivalent phantoms are necessary for the quality control and calibration of diagnostic radiology equipment. Breast compression is critical during x-ray mammography (§1.8.2.2). Despite this none of the mammographic phantoms routinely used to date have been similarly compressible (§1.9). The development of compressible phantoms could also allow the tissue deformations caused by compression to be better understood. Locating a lesion imaged under compression in the later uncompressed breast, during biopsy or surgery, is difficult. The development of breast deformation models, which could be evaluated through comparison of their predicted deformations with the true deformations seen in compressible phantoms, would help to tackle this problem (§1.8.2.3). Deformation models used in the registration of dual-modality images (including optical and x-ray), which may have been acquired under different levels of compression, also require validation (Guo et al 2006). Furthermore it has been proposed that acquiring dynamic optical images of the breast as compression is applied and released may aid the detection of cancerous regions by increasing their contrast (§1.8.2.4). In order to evaluate the full potential of combined x-ray and optical mammography, as well as dynamic techniques, compressible phantoms with optical and x-ray properties simultaneously characteristic of breast tissue are required.

Whilst numerous incompressible phantoms with either optical or x-ray properties characteristic of breast tissue are available very few of these are suitable for dual-modality imaging, possessing characteristic x-ray and optical properties simultaneously. More importantly no such elastically compressible phantoms exist so far as the author is aware. In this work the potential of a novel phantom material, an elastically compressible and reusable polyvinyl alcohol (PVAL) based gel, is evaluated. This gel's properties

have been characterised and modified so as to simultaneously possess optical, x-ray and mechanical properties similar to those of breast tissue. Different types and pathologies of breast tissue can exhibit significantly different properties. As such the properties of the gels can be accurately adjusted within suitable ranges. PVAL based gels have previously been used in Fricke dosimetry (Chu et al 2000). These gels contain ferrous sulphate which oxidises to ferric sulphate upon irradiation. The amount of ferric sulphate produced, which is linearly proportional to the dose absorbed, can be determined through optical spectroscopy or magnetic resonance imaging. It is possible that these gels could be made with tissue equivalent mechanical properties, thus allowing realistic deformations to be more readily accounted for in radiotherapy treatment planning.

Prior to the PhD I had previously investigated the potential of PVAL based 'slime' as an optical phantom material (Hebden et al 2006). This is generated by mixing aqueous solutions of PVAL and sodium tetraborate decahydrate. Whilst possessing ideal optical properties these 'slimes' were not elastically compressible and could not hold their own shape. Very solid and highly elastic gels can be formed by freezing and then thawing solutions of PVAL but purely water based solutions treated in this manner result in highly turbid and optically inhomogeneous gels. This arises because pores of differing refractive index are formed due to ice crystal formation (Hyon and Ikada 1987). Unpredictable baseline optical properties of this nature had to be avoided. If the freezing point of the solution can be suppressed so ice crystals do not form on cooling then transparent and colourless (yet solid and highly elastic) gels can be produced. This can be achieved by dissolving the PVAL in a mixed solvent of water and dimethyl sulphoxide (DMSO) (Hyon et al 1989). Preliminary tests showed that these gels had a linear x-ray attenuation coefficient in excess of 3.4 cm^{-1} at 17.5 keV, approximately four times greater than that typical of breast tissue (Johns and Yaffe 1987), due to the sulphur content of the DMSO (the atomic number of sulphur is 16). As a result the possibility of using a different solvent, ethanol, to suppress the freezing point was investigated. It was found that solutions of PVAL in 50:50 mixtures of ethanol and water also produce highly transparent and non scattering gels whilst having an x-ray attenuation equivalent to breast tissue. A further advantage of using ethanol is that it costs a fraction of the price of DMSO.

The purpose of the work presented in this thesis was to develop a compressible phantom material with breast equivalent x-ray attenuation and optical properties. This allowed the

feasibility of producing compressible phantoms, suitable for use in the characterisation and evaluation of dual-modality imaging systems, to be assessed. It was not felt that the Young's modulus of this material needed to match that of breast tissue as closely as the x-ray attenuation. If necessary the phantom could simply be compressed with a greater or lesser force than typical of mammography to obtain the desired deformation. It was more important that the stiffness of the material could be altered so as the relative, rather than absolute, difference in stiffness seen between cancerous and healthy tissues could be mimicked.

4.3. X-ray, optical and mechanical properties of breast tissue

4.3.1. X-ray attenuation

The linear x-ray attenuation coefficient of breast tissue is relatively well characterised though it varies with composition and therefore age (Carney et al 2003). Fibroglandular tissue is much more attenuating than adipose tissue. The average linear x-ray attenuation coefficients of fibrous and fatty tissue, at a typical mammographic energy of 18 keV, have been measured as 1.03 and 0.56 cm⁻¹ respectively (Johns and Yaffe 1987). As breast tissue is widely viewed as an approximately equal mix of fatty and fibrous tissue (Peart 2005) these values agree with the value of 0.89 cm⁻¹ for 'breast tissue' at 18 keV found on the XCOM database of photon cross sections (Berger et al 2009). At 1.09 cm⁻¹ infiltrating ductal carcinoma has a slightly higher x-ray attenuation than fibrous tissue (Johns and Yaffe 1987).

4.3.2. Optical properties

The optical properties of breast tissue vary significantly between different women as well as with a number of factors such as age, body mass index and menstrual status (Suzuki et al 1996). Whilst a number of *ex-vivo* measurements have been made it is not clear how these might be expected to relate to values *in-vivo* due to the very different circumstances (blood supply etcetera) in each case (Gibson et al 2005). The largest *in-vivo* study of healthy breast tissue to date presented the average bulk optical properties of fifty-two women (Durduran et al 2002). The mean absorption (μ_a) and transport scatter (μ_s') coefficients (at 786 nm) were found to be (\pm standard deviation) 0.0041 ± 0.0025 and 0.85 ± 0.21 mm⁻¹ respectively. These values are in good agreement with those found in a

number of other studies which were recently reviewed (Leff et al 2008). This review calculated the global average values of healthy tissue, across all studies included, to be 0.004 ± 0.002 and $0.8 \pm 0.4 \text{ mm}^{-1}$ for μ_a and μ_s' respectively. The largest *in-vivo* study presenting the properties of diseased tissue took measurements on 87 women who were later confirmed as having a carcinoma histologically (Grosenick et al 2005). The optical properties of surrounding healthy tissue were also determined for each patient. At 785 nm the median μ_a was found to be 0.01 ± 0.006 and $0.0039 \pm 0.0011 \text{ mm}^{-1}$ for carcinoma and healthy tissue respectively. Similarly the median μ_s' was found to be 1.16 ± 0.39 and $0.95 \pm 0.14 \text{ mm}^{-1}$ for carcinoma and healthy tissue respectively. These values for healthy tissue show good agreement with those above. This study found that both μ_a and μ_s' are higher for carcinomas than healthy tissue. This trend has been observed in a number of other very limited studies with just one or two patients (Chernomordik et al 2002, Fantini et al 1998). On the other hand another small study found this to be the case in some patients but the other way round (μ_a and μ_s' lower for carcinomas) for others (van Veen et al 2004).

Whilst the optical properties of breast tissue are clearly variable significant differences can be seen between different types and pathologies of tissue, particularly between those of a given patient. In light of this it was decided that the phantom material should be developed such that its μ_a and μ_s' could be accurately varied over a wide range of values. In this way it will be possible to mimick the properties characteristic of both healthy and cancerous tissues, as well as tissues with intermediate values.

4.3.3. Mechanical properties

Very few attempts have been made to characterise the Young's moduli of different soft tissues, either *ex-vivo* or *in-vivo*, under compression. Here the mechanical properties of breast tissues are reviewed. Whilst it can be difficult to compress other *in-vivo* tissues due to anatomical constraints this is not true of the female breast which is readily compressed during mammography. Surprisingly only one, very limited, *in-vivo* breast compression study has been performed (Williams et al 1999) despite calls for more quantitative control over mammographic compression to ensure optimum performance (Poulos and McLean 2004). Furthermore the few studies that have been performed strongly suggest that tissue stiffness can be related to pathology (Wellman et al 1999). It

is this discovery which fuels interest in elastographic techniques that could aid the non-invasive differentiation of benign from malignant lesions (Greenleaf et al 2003).

There have been numerous studies evaluating the potential of both ultrasound and magnetic resonance elastography (Fatemi et al 2003, Kruse et al 2000, Ophir et al 1999). Ultrasound elastography provides useful qualitative maps of the distribution of Young's modulus within tissue rather than accurate quantitative measurements (Fatemi et al 2003). Several studies have reported initial measurements of Young's modulus, in different types of breast tissue, made by magnetic resonance elastography (McKnight et al 2002, Sinkus et al 2005, Sinkus et al 2000, Van Houten et al 2003). Such measurements are made by analysing very small (up to 500 μm) relatively high frequency (50 to 400 Hz) tissue deformations. Whilst this provides qualitative measurements of Young's modulus at approximately zero strain breast tissue does not obey Hooke's law. Breast tissue demonstrates a non-linear stress-strain relationship within the region of elasticity (Krouskop et al 1998, Wellman et al 1999). Because of this, measurements at much larger deformations are required to determine the mechanical properties typical of breast tissue under mammographic compression. Only the properties of breast tissues as obtained through traditional force-deformation analysis during compression are reviewed here.

The only *in-vivo* study of the mechanical properties of the breast, of which the author is aware, presents results obtained from just four patients (Williams et al 1999). Furthermore the forces applied and resulting deformations are not recorded in such a way that values of Young's moduli can be calculated. To the author's knowledge four *ex-vivo* studies have been performed (Krouskop et al 1998, Samani et al 2007, Sarvazyan et al 1994, Wellman et al 1999). Unfortunately there is an inconsistency within Saravazyan's study, with two of the figures showing contradictory values to one another. All three remaining studies performed punch indentation on small *ex-vivo* tissue samples removed from larger excised masses. This involves compression of a small area, rather than the whole, of the surface of the sample using a small (typically 5mm) diameter cylindrical rod. The Young's modulus values reported between studies, for a given tissue, vary considerably. This is almost certainly due to variations in the method of testing. Despite the large variations seen between studies a number of important observations can be made. Firstly most tissues, with the exception of adipose, demonstrate a highly non-linear stress-strain relationship within the region of elasticity (Krouskop et al 1998,

Wellman et al 1999). Secondly cancerous tissues are generally much stiffer than healthy ones, typically by a factor of ten at 15 to 20% strain (Krouskop et al 1998, Wellman et al 1999). The difference between these tissue types becomes increasingly pronounced with increasing strain because the stress-strain relationship of cancerous tissues is more non-linear than that of healthy tissues (Wellman et al 1999). Two of the studies investigated how the speed with which deformation was applied affected the Young's modulus observed but this was not found to make a very significant, if any, difference (Krouskop et al 1998, Wellman et al 1999).

Because the measurements described above were made by punch indentation on *ex-vivo* tissue it is difficult to determine the likely mechanical properties of the breast as a whole from them. Furthermore the reported values for healthy fibroglandular tissues differ widely, from 3 to 18 kPa at 1% strain (Samani et al 2007 and Wellman et al 1999 respectively), increasing to between 57 and 272 kPa at higher strains of 15 to 20% (Krouskop et al 1998 and Wellman et al 1999 respectively). The reasons for these differences are probably due to differences in experimental method and tissue selection. Regardless of these differences all studies reported increased stiffness in cancerous tissues. In light of this situation it was decided to make measurements on larger materials under parallel plate compression.

4.3.4. Summary of required phantom properties

Having reviewed the x-ray, optical and mechanical properties realistic of breast tissues the properties required of the phantom material are summarised in table 4.1.

	Linear x-ray attenuation coefficient	Optical absorption (μ_a) and transport scatter (μ_s') coefficients	Young's modulus
Essential	Equivalent to healthy breast tissue (0.8 to 0.9 cm^{-1})	Both coefficients should be variable over a range realistic of healthy through to cancerous tissue. μ_a variable from 0.004 to 0.01 mm^{-1} μ_s' variable from 0.85 to 1.16 mm^{-1}	Variable by a factor of ten so that relative difference in stiffness between healthy and cancerous tissues can be mimicked
Preferable	Variable over a range from 0.5 to 1.1 cm^{-1} so that adipose and fibrous/cancerous tissues can be mimicked		Ideally variable from approximately 20 to 220 kPa so as to be quantitatively realistic (Krouskop et al 1998)

Table 4.1. The desired properties of the phantom material.

4.4. Method

4.4.1. Manufacture of gels

4.4.1.1. DMSO based gels

In order to investigate the effect of sample geometry on the measured mechanical properties, cylindrical gel samples of varying dimensions were required. Seven DMSO based 9% w/v (weight-volume percentage) PVAL gels were used. Although their x-ray attenuation was later found to be too high these gels were suitable for investigating the effects of sample geometry. Their dimensions are shown in table 4.2. Samples 1 to 3 were all the same size, allowing reproducibility of the samples and test method to be assessed. The dimensions of the four remaining samples varied such that the effect of sample diameter and height upon the observed mechanical properties could be independently investigated.

	Height (mm)	Diameter (mm)	Height to diameter ratio (2 s.f.)
Sample 1	32	64	0.50
Sample 2	32	64	0.50
Sample 3	32	64	0.50
Sample 4	32	47	0.68
Sample 5	23.5	47	0.50
Sample 6	47	47	1.00
Sample 7	64	64	1.00

Table 4.2. The dimensions of the seven DMSO based 9% w/v PVAL gel samples.

The 9% w/v PVAL samples were all produced from the same batch of PVAL solution. This was made by dissolving 72 g of polyvinyl alcohol (PVAL) (Sigma-Aldrich, catalogue number 363146) in 800 ml of solvent, made from 4 parts DMSO (VWR, catalogue number 802912) to 1 part distilled water. Due to the low solubility of PVAL the solvent was placed on a 200°C hotplate and stirred for 25 minutes, reaching 75 to 85°C, before the PVAL was added. The mixture was then heated and stirred continuously for a further 45 minutes during which time the solution reached a temperature of approximately 95°C and all the PVAL dissolved. The solution was then poured into the prepared moulds, formed by sealing measured lengths of plastic pipe to acetate paper. After being left to cool for one hour these were then placed in the freezer, at -13°C, to gel. After 22 hours the gels were removed from the freezer and submerged in a 4:1 mixture of DMSO and distilled water. This prevents the gels from drying out during storage.

4.4.1.2. Ethanol based gels

Ethanol (VWR, catalogue number 10107) based gels were made by dissolving PVAL in a solvent made from equal parts by volume of ethanol and water. During preliminary experimentation PVAL was found to be largely insoluble in solvents made with more than 65% v/v (volume-volume percentage) ethanol, whilst solvents containing less than 30% v/v ethanol will freeze (Clarke and Mortimer 1919). It was also observed that a gel formed using a 35% v/v ethanol solvent appeared to be less firm than that made using a 50% v/v ethanol solvent containing the same concentration of PVAL. In light of these findings gels with PVAL concentrations of 5 to 20% w/v (in 2.5% increments) were produced using a 50% v/v ethanol solvent. In addition a 10% w/v PVAL sample was

produced using a 35% v/v ethanol solvent so that the effect of ethanol concentration on stiffness could be verified more quantitatively.

To prevent evaporation of ethanol during the prolonged heating and stirring of each mixture Quickfit[®] apparatus was used. The reaction vessel, which stood on a heating mantle, was fitted with a lid containing three access holes. The first of these was fitted with a water cooled condenser. The second was sealed with a thermometer such that the temperature of the mixture could be monitored. The third was fitted with a bung through which the shaft of a stirring rod was placed. Before any heat was applied the water and ethanol were added to the vessel and the stirrer started. The PVAL was then added through the access point normally sealed by the thermometer. Once the thermometer had been replaced the mixture was heated to boiling point. The heat was then reduced such that the solution remained at this temperature (approximately 83°C) but did not boil too vigorously. By following these steps the fusion of PVAL onto the wall of the reaction vessel is avoided and the condenser is not overloaded. The time taken for the PVAL to dissolve increases with the quantity added but ranges from 70 to 135 minutes once boiling point has been reached. After this period each solution was transferred to a mould with a diameter and height of 64 and 32 mm respectively. Each solution was allowed to cool for one hour before being placed in the freezer, at -13°C, to solidify. After 22 hours each gel was removed from the freezer and submerged in a 1:1 mixture of ethanol and distilled water for storage.

4.4.2. Measurement of linear x-ray attenuation coefficient

The x-ray attenuation coefficients of five ethanol based gels were measured. These were the 5, 10 (both 35 and 50% v/v ethanol), 15 and 20% w/v PVAL gels. Each gel was cut, with a razor blade, to produce a minimum of 6 slices of different thickness which were each placed, in turn, in the setup described below. The same setup was used when making the preliminary measurement on a DMSO based 10% w/v PVAL gel.

All attenuation measurements were made using a tungsten target x-ray source, operated at 30 kV and 4.0 mA, whose beam was directed toward a 30 µm molybdenum foil to produce characteristic 17.5 keV photons. To increase the number of characteristic (relative to primary) photons detected, the attenuating sample, collimators and detector were placed at an angle of approximately 30 degrees to the primary beam. A high purity

germanium detector was used to resolve the energy of detected photons and establish the number observed in the 17.5 keV peak. The accuracy of the system was validated by measuring the attenuation coefficient of aluminium, using a set of pure aluminium foils of known thicknesses as samples, and comparing this to the known value. In order to ensure good statistics each sample was irradiated until a minimum of 10,000 counts had been recorded in the 17.5 keV peak. This technique meant that exposure times increased with sample thickness and this was corrected by scaling the counts recorded with the integrated exposure reading, taken on the source side of the sample, of each acquisition. This also acted to correct for any fluctuations in beam intensity that may have occurred. Counts recorded also had to be corrected to account for changes in detector dead time. The attenuation coefficient is given by the gradient of the best fit line when $\log_e(\text{counts})$ is plotted versus sample thickness.

It should be noted that the x-ray emission spectrum of a mammography source is not monochromatic. Nonetheless by far the largest peak in the spectrum occurs at 17.5 keV, along with a smaller peak at 19.5 keV, due to the characteristic emissions of molybdenum (Tucker et al 1991). In mammography filtration of the beam with a molybdenum foil to eliminate significant amounts of bremsstrahlung is common. As a result characterising the attenuation coefficient of the gels at the single, greatly predominant, energy of 17.5 keV is sufficient to indicate their level of tissue equivalence. Furthermore the values obtained for the gels are compared with those obtained for breast tissues using a very similar, energy resolving, technique at a specific and almost identical energy of 18 keV (Johns and Yaffe 1987) .

4.4.3. Characterisation of optical properties

To characterise the relationship between the concentration of titanium dioxide powder (Alec Tiranti Ltd., London) within the gels and their transport scatter coefficient seven cylindrical gel samples 32 mm thick and 64 mm in diameter were produced. Each sample was made using a different concentration of titanium dioxide powder (in the range 0.80 to 2.01 grams per litre) but the same concentration of PVAL, 10% w/v, in a 50% v/v ethanol solvent. The temporal point spread function generated by the transmission of picosecond pulses of light between each sample's parallel faces was then measured using one channel of MONSTIR (§1.7.3.1). The transport scatter coefficient of each gel was found by fitting an analytical solution to the time dependent diffusion equation to each of these

measured temporal point spread functions. The quantities of titanium dioxide added are very small and it was found, experimentally, that these additions did not significantly increase the x-ray attenuation coefficients of the gels (§4.5.1). The optical absorption of the gels is readily adjusted through the addition of a well characterised near-infrared dye, ICI S109564 (Kirkby 1999). In order to ensure that the titanium dioxide and dye mix into the solution homogeneously it is important to add these before the PVAL. In this way they are distributed homogeneously before the solution gains viscosity.

4.4.4. Mechanical testing

An Instron 3345 mechanical testing machine, designed to characterise the mechanical properties of materials under applied loads, was used to perform the compression testing of all samples (figure 4.1).



Figure 4.1. The Instron testing device with one of the gels positioned between the compression plates.

4.4.4.1. Effect of sample geometry and compression speed

To establish the effect of sample geometry on Young's modulus, the DMSO based 9% w/v PVAL gels of varying geometry were tested. Each gel was subjected to eight cycles of compression between two horizontal plates that were much larger than the area of the gels, even when fully compressed. In order to ensure good contact between the upper plate and each sample these were slowly brought together until no air gap could be seen between them. Care was taken not to compress the sample during this operation and once in position the load and plate position (equivalent to sample deformation) were reset to zero before compression commenced. Each three stage cycle consisted of i) the sample being compressed at a rate of 60 mm/min until a force of 200 N had been applied, ii) the sample being held at this level of deformation for 1 minute and iii) compression being released at a rate of 60 mm/min until the compression plate had moved back to its original position. The samples were not tested beyond 200 N as this is the maximum force applied in mammography (Lawinski and Dunne 2003). Between each cycle of compression, samples were removed from the Instron and allowed to stand for a minimum of 15 minutes. Compressing each gel a number of times allowed verification as to whether each compression in any way altered or damaged the gels such that their mechanical properties altered with each compression.

To verify whether the speed of compression affected the measured Young's modulus, a DMSO based 10% w/v PVAL sample was subjected to four compressions, each applied at a different rate. These compressions were performed identically to those previously except that the rate of compression (and release) was modified. The speeds utilised were 15, 30, 60 and 120 mm/min. Only one compression was performed at each speed.

4.4.4.2. Testing of pork tissue

In order to evaluate the method on a biological sample some pork was tested. One piece of pork steak was purchased from a butcher and carefully cut into four cylindrical samples the same size as the ethanol based gels (64 mm diameter and 32 mm high). Each sample was compressed to a maximum of 200 N at a rate of 60 mm/min. Each sample was only compressed once as they were almost completely inelastic.

The pork samples used consisted almost entirely of muscular tissue. The muscular fibres within these samples ran parallel to the direction of compression. Whilst the orientation of the musculature can affect the measured mechanical properties (Kruse et al 2000, Sinkus et al 2005) this was not of concern because the purpose of this testing was purely to evaluate the test method. This pork proved a reasonable material to test as it was found to have a value for Young's modulus similar to those published by Krouskop for fibrous tissue or ductal carcinoma in situ (Krouskop et al 1998).

4.4.4.3. Testing ethanol based gels of varying PVAL concentration

The ethanol based gels were all tested in exactly the same manner as the DMSO based gels of varying geometry. Each was subjected to the same eight cycles of compression, each cycle separated by at least 15 minutes (§4.4.4.1). Critically each individual compression cycle was identical to that applied to the pork tissue.

4.5. Results

4.5.1. Linear x-ray attenuation coefficients

The relationship between PVAL concentration and linear x-ray attenuation coefficient for gels made with a 50% v/v ethanol solvent are shown in figure 4.2. All the gels have a linear x-ray attenuation coefficient very similar to that typical of healthy breast tissue, $0.8\text{--}0.9\text{ cm}^{-1}$ (§4.3.1). The x-ray attenuation coefficient of the 10% w/v PVAL gel made with a 35% v/v ethanol solvent was $0.83 \pm 0.01\text{ cm}^{-1}$, higher than that of its 50% v/v ethanol solvent counterpart. This is to be expected as ethanol is less attenuating than water (Berger et al 2009). The x-ray attenuation coefficient of the 10% w/v PVAL gel containing the highest concentration of titanium dioxide (2.2 g l^{-1}) was also measured and found to be 0.79 cm^{-1} . This is the same, within measurement error, as that of the 10% w/v PVAL gel which did not contain any titanium dioxide.

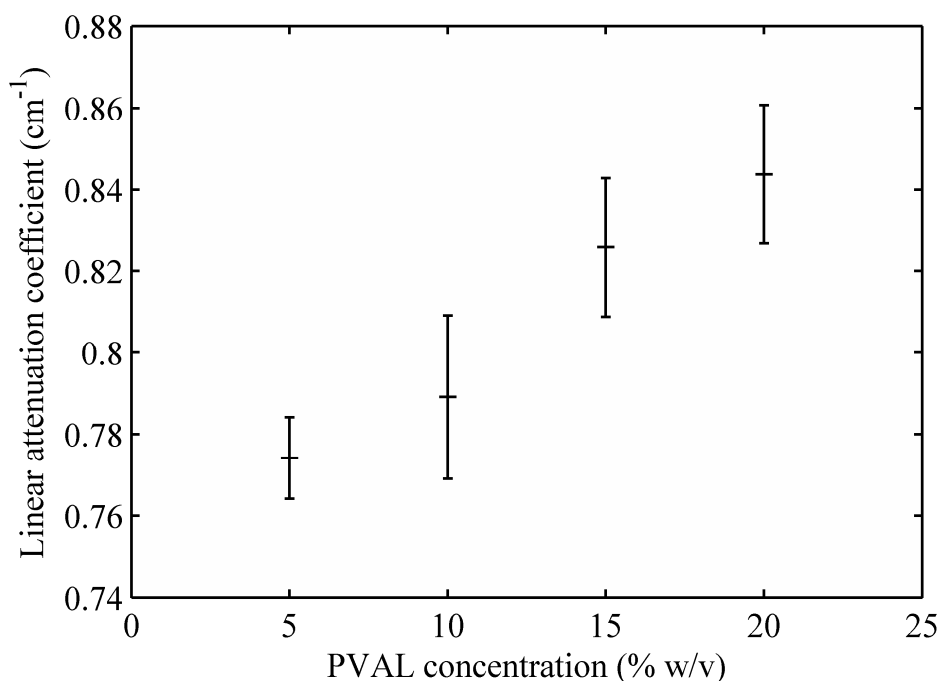


Figure 4.2. Linear x-ray attenuation coefficient increases with PVAL concentration. Error bars represent the square root of the variance on the gradient of each sample's total least squares regression line.

4.5.2. Optical Properties

The relationship between the concentration of titanium dioxide powder contained and the transport scatter coefficient of the gel produced is shown in figure 4.3. Healthy and cancerous breast tissues typically have transport scatter coefficients of 0.85 and 1.16 mm⁻¹ respectively (§4.3.2). Equivalence to either is readily achieved. The absorption coefficient of the gel is adjusted through the addition of near infra-red dye, ICI S109564, which has previously been characterised (Kirkby 1999) and used in a number of optical phantoms (Cooper et al 2009, Matcher et al 1997)

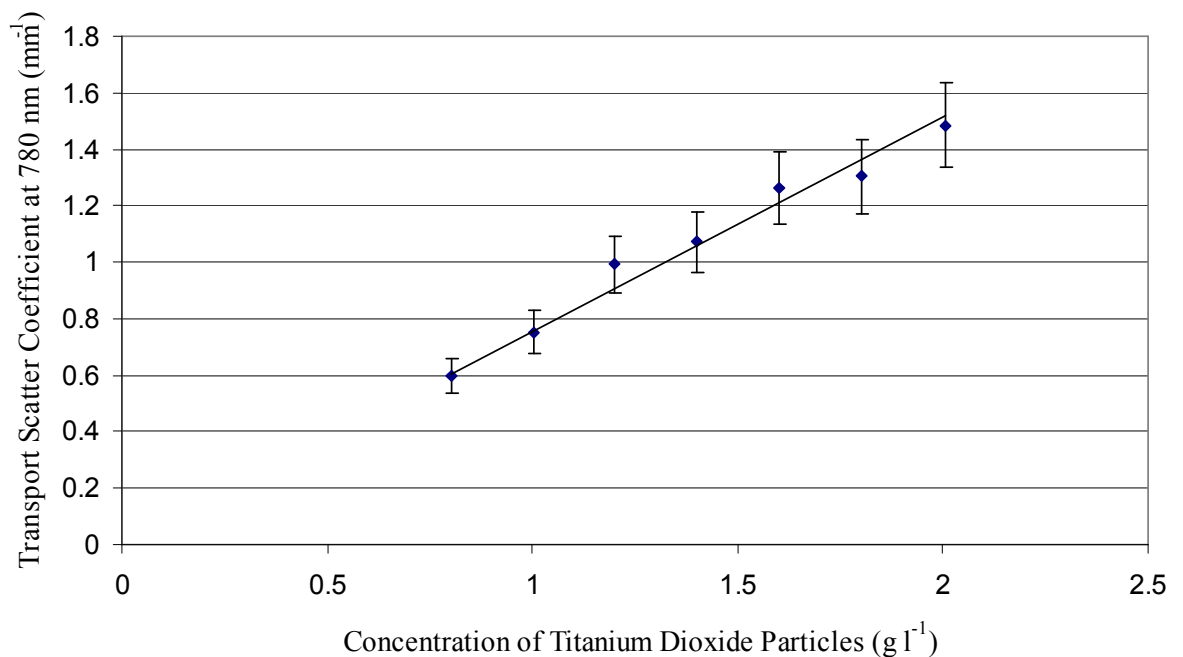


Figure 4.3. Transport scatter coefficient of the initially non-scattering gels can be increased through the addition of titanium dioxide. Error bars shown represent a 10% error. Previous experience of similar phantom measurements made within the research group suggest that these are realistic.

4.5.3. Mechanical testing

4.5.3.1. Effect of sample geometry and speed of compression

For each DMSO based sample tested the Young's modulus curve obtained was found to be independent of the number of previous compressions, up to the eight times tested, demonstrating good repeatability. The repeated compressions did not visibly damage any of the samples. The average Young's modulus curve obtained for each sample is shown in figure 4.4. The mean Young's modulus curves of the three samples with identical

dimensions lay within one standard deviation of one another. For this reason no difference could be distinguished between their mechanical properties under compression. The eight curves obtained for sample three appear to have a larger spread than those of samples one and two and this is represented by the larger error bars for this sample. The reason for this remains unclear. Whilst the spread of these curves was greater none were clear outliers and all were included in the average. It can be seen by comparing the other curves to those of samples one to three that Young's modulus does depend on the sample geometry. This is discussed further in §4.6.3.1, as is the initial 'kink' seen in the curves at low strain.

Within the range tested (between 15 and 120 mm/min) the effect of compression speed upon the Young's modulus lay within experimental error and so could not be distinguished.

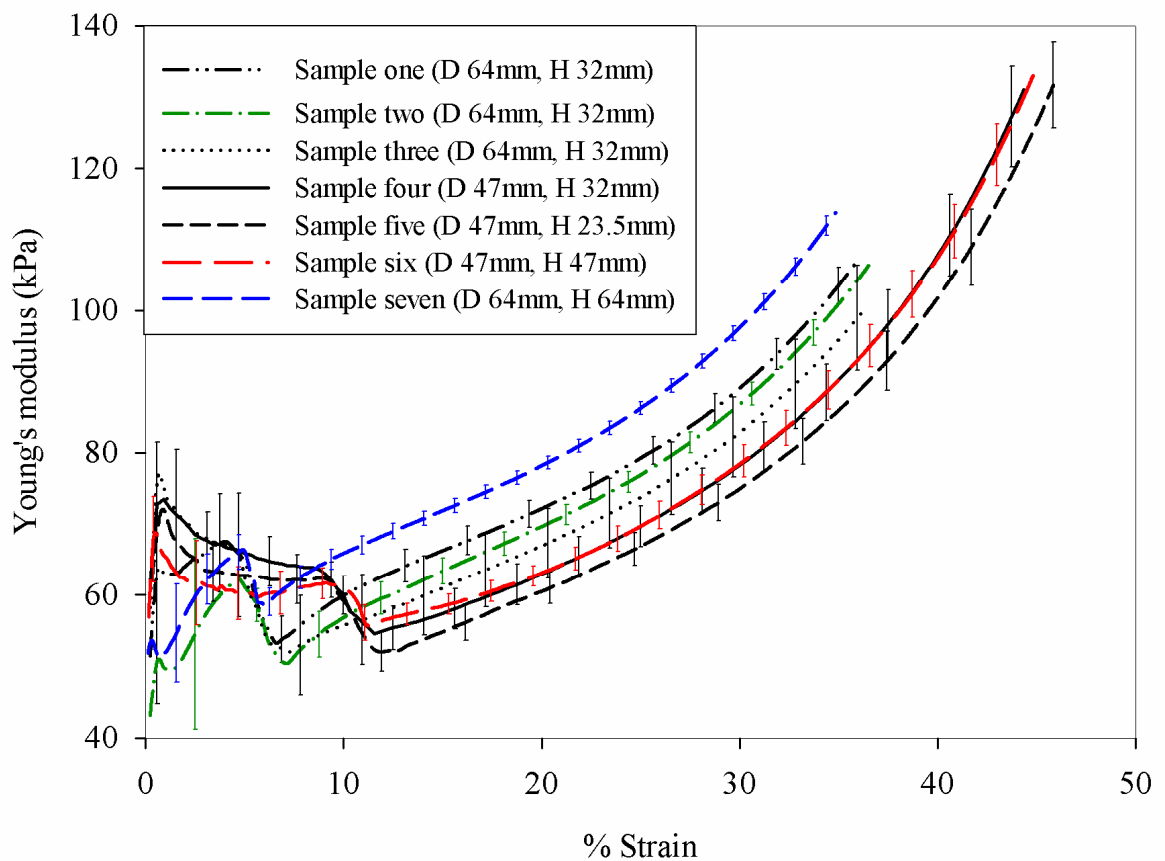


Figure 4.4. Young's modulus shows some dependence on sample geometry. Error bars show the standard error on mean values and are only displayed at every tenth data point to preserve clarity.

4.5.3.2. Pork tissue

The Young's modulus curves obtained from the four pork samples are shown in figure 4.5. Whilst some variation is seen between these samples, as is to be expected due to natural differences between them, all display similar mechanical properties.

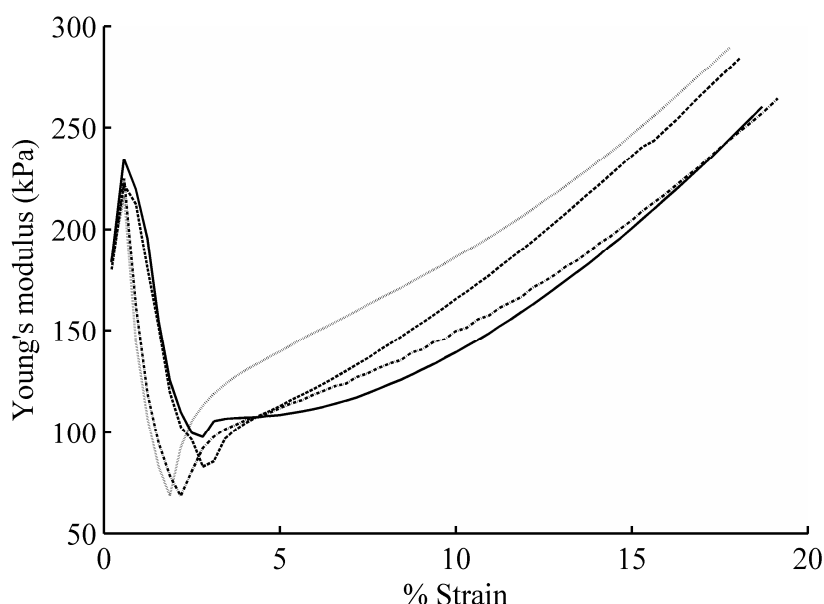


Figure 4.5. Four different samples of pork tissue demonstrate similar mechanical properties under compression. Errors are not shown because these could not be characterised; each pork sample could only be compressed once.

4.5.3.3. Effect of PVAL concentration in ethanol based gels

The 5% w/v PVAL ethanol based gel was very weak and tore during the second cycle of compression. With this exception no discernable dependency upon the number of previous compressions applied, up to the eight times tested, could be seen in the Young's modulus curves of the other gels. The repeated compressions did not visibly damage these samples. The average Young's modulus curve, over all eight compressions, for each of the undamaged samples is shown in figure 4.6. The Young's modulus, at given strain, increases with PVAL concentration. The maximum strain reached reduces with increasing concentration. This is expected as the same maximum force of 200 N was applied to all gels, causing less deformation in the stiffer samples. The Young's modulus curve of the 10% w/v PVAL gel made using the 35% v/v ethanol solvent (as opposed to 50% v/v ethanol solvent as used to produce all the other gels) is also shown. This gel had the lowest Young's modulus of all the gels.

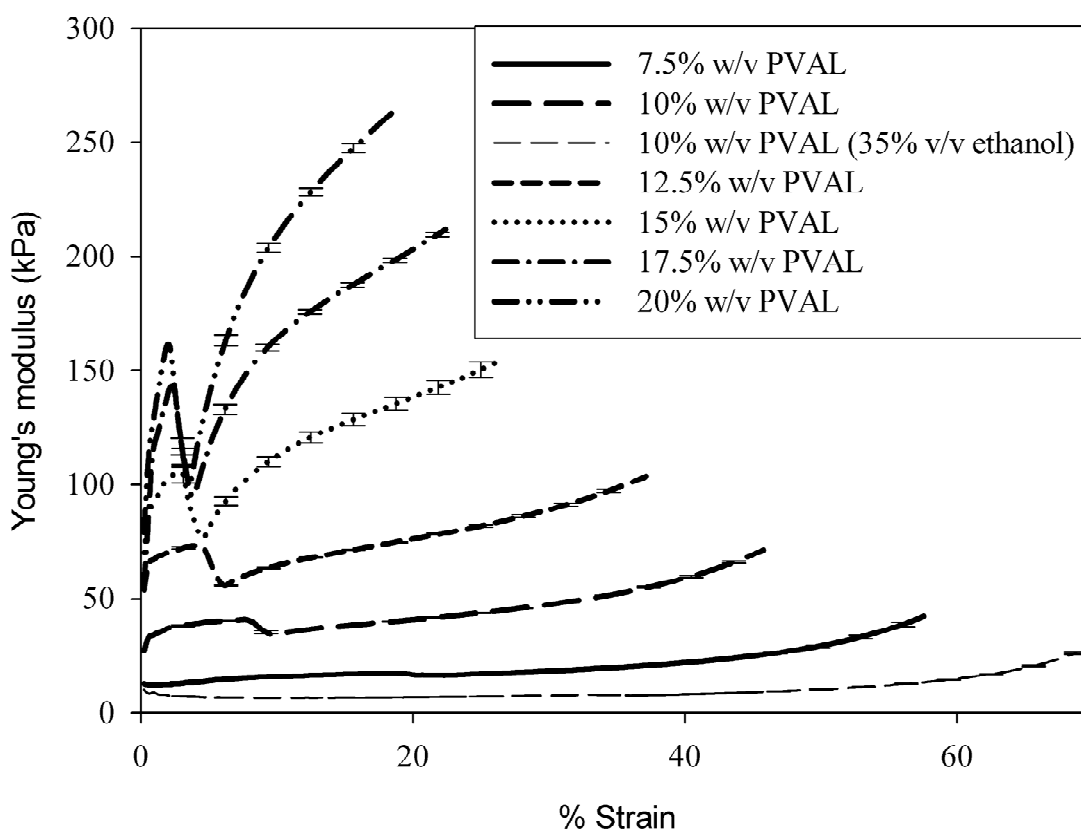


Figure 4.6. At a given strain Young's modulus increases with PVAL concentration. Error bars show the standard error on mean values and are only shown on every tenth data point to preserve clarity.

4.6. Discussion

4.6.1. X-ray attenuation of gels

The x-ray attenuation coefficients of ethanol based gels with PVAL concentrations of 5 to 20% w/v were in the range of $0.76\text{-}0.86\text{cm}^{-1}$ at 17.5 keV, increasing with PVAL concentration. These values are very similar to those typical of breast tissue, $0.8\text{-}0.9\text{cm}^{-1}$ (§4.3.1). For further comparison Lucite, a plastic commonly taken to be tissue equivalent and used in mammography phantoms (Faulkner and Law 1994), has an x-ray attenuation coefficient of 0.91cm^{-1} at 17.5 keV (Berger et al 2009). The addition of small quantities of titanium dioxide powder to the gels did not increase their x-ray attenuation significantly.

Increasing the x-ray attenuation to obtain gels with coefficients similar to those of fibrous or cancerous tissue would readily be achieved by adding small quantities of DMSO or a heavy metal salt, such as barium chloride, to the PVAL solution before freezing.

Similarly gels with a lower density and linear x-ray attenuation coefficient, similar to adipose tissues, would sometimes be desirable. This could be achieved through the addition of low density, hollow, phenolic resin microspheres. The use of such microspheres to reduce the density of resin based phantoms is relatively common (Bolotin et al 2001, Jones et al 2003, White et al 1977). Though the gel with a lower, 35% v/v, ethanol content had a higher x-ray attenuation, increasing the ethanol content to reduce the x-ray attenuation is not viable as the PVAL becomes insoluble. It should be noted that the additions suggested here may require the phantom to be handled and stored with much more care. The above additions have not been performed, nor the possible risks associated considered.

4.6.2. Optical properties

The transport scatter coefficient of the gels increases linearly with the concentration of titanium dioxide powder contained. Transport scatter coefficients from 0.6 to 1.5 mm⁻¹ can readily be achieved. This range of values covers those characteristic of all types of breast tissue (typically 0.85 mm⁻¹ for healthy tissue increasing to 1.16 mm⁻¹ for cancerous as discussed in §4.3.2). Because the optical properties of breast tissue vary between women as well as with a number of other factors it was important that the optical properties of the gels produced could be varied accurately over the whole of this range. The absorption coefficient of the gels is just as readily adjusted through the addition of the well characterised near infra-red dye, ICI S109564.

4.6.3. Mechanical measurements

4.6.3.1. Effects of sample dimensions and rate of compression

Sample dimensions were found to have a moderate effect on the Young's modulus measured at a given strain (figure 4.4) but the differences seen between samples of different PVAL concentration, but with identical dimensions, are much larger. The small error bars show that repeated testing of each sample yielded very similar results, indicating that the test was reliable. All the pork samples and gels whose Young's modulus values are compared were as similar in size as reasonably achievable. Because of this the differences seen between these samples can be taken as truly mechanical, not due to very small variations in size or a poor method of testing.

The initial ‘kink’ seen in the Young’s modulus curves at low percentage strain appears not only in the PVAL measurements (figures 4.4 and 4.6) but also in those of pork tissue (figure 4.5). This is hypothesised to be an elastic buckling effect. The gels are known to have a porous structure (Hyon and Ikada 1987), suggesting that the ‘scaffold’ of PVAL, rather than the pores, offer much of the resistance to compression at very low strains. Once the force applied becomes large enough, this structure may buckle. Beyond this point increasing force is required to further deform both the PVAL structure and the pores within. A similar analogy can be applied to the structure of pork tissue built around a collagen matrix.

4.6.3.2. Pork tissue

Each pork sample was tested to 200 N, the maximum force allowed in mammography, and this led to a maximum strain of approximately 18% in all four samples (figure 4.5). Benchmarking against human tissue suggests this pork sample is stiffer than healthy breast tissue but comparable with fibrous tissue or ductal carcinoma, thereby proving to be a reasonable test object for this purpose. At 15% strain the average Young’s modulus of the pork tissue is approximately 220 kPa. In comparison the Young’s moduli for fibrous tissue and ductal carcinoma *in situ* have been reported as being approximately 230 and 300 kPa, at 20% strain, respectively (Krouskop et al 1998). On the grounds that healthy tissue is approximately ten times less stiff than this (§4.3.3) its Young’s modulus can be taken to be approximately 20 kPa at 15% strain.

4.6.3.3. PVAL gels

The Young’s modulus of the gels can be adjusted by changing the PVAL concentration. The gel with a PVAL concentration of 20% w/v has similar Young’s moduli to pork tissue at high percentage strains. Such a gel can therefore be used to mimic cancerous or very fibrous lesions. Similarly a gel equivalent to healthy tissue would have a PVAL concentration of 7.5 to 10% w/v. These observations agree well with perception: high concentration PVAL gels seem much stiffer to the touch than normal breast tissue. Gels made with lower PVAL concentrations are much more breast like.

The 10% w/v PVAL gel made using a 35% v/v ethanol solvent had a Young’s modulus four or five times lower, at any given strain, than the 10% w/v PVAL gel made with

50% v/v ethanol solvent. It has previously been shown, using DMSO, that the size of pores formed within the gels increases with water content (Hyon and Ikada 1987). This phenomenon almost certainly applies to ethanol based gels too. A gel containing large pores and a less regular structure of PVAL would be expected to have a lower Young's modulus.

4.6.4. Summary of properties achieved

A summary of the phantom material's properties, in comparison with those originally desired, is given in table 4.3.

	Linear x-ray attenuation coefficient	Optical absorption (μ_a) and transport scatter (μ_s') coefficients	Young's modulus
Essential	Very similar to healthy breast tissue (0.8 to 0.9 cm^{-1})	Both coefficients should be variable over a range realistic of healthy through to cancerous tissue. μ_a variable from 0.004 to 0.01 mm^{-1} μ_s' variable from 0.85 to 1.16 mm^{-1}	Variable by a factor of ten so that relative difference in stiffness between healthy and cancerous tissues can be mimicked
Preferable	Variable over a range from 0.5 to 1.1 cm^{-1} so that adipose and fibrous/cancerous tissues can be mimicked		Ideally variable from approximately 20 to 220 kPa so as to be quantitatively realistic (Krouskop et al 1998)
Achieved	All gels in the range 0.76-0.86 cm^{-1} , very similar to that of healthy breast tissue. Attenuation could readily be increased through addition of DMSO. Similarly low density filler could reduce it.	μ_s' variable over a wide range (0.6 to 1.5 mm^{-1}). Though not performed in this work μ_a could readily be varied over the necessary range through addition of a near infra-red dye (as performed in the production of numerous phantoms within the biomedical optics group)	Readily varied over required range, from 20 kPa to in excess of 220 kPa at 20% strain, by altering PVAL concentration.

Table 4.3. The properties of the characterised PVAL gels in comparison with those originally desired.

4.7. Conclusion

The x-ray, optical and mechanical properties of a novel ethanol based PVAL gel which is readily and cheaply produced through freeze-thawing have been characterised. In their unmodified form these gels have an x-ray attenuation virtually identical to that of healthy breast tissue. Their x-ray attenuation could readily be increased to match that of cancerous or very fibrous breast tissue by adding a heavy metal salt to the PVAL solution prior to freezing. The optical transport scatter coefficient of the gels can be accurately adjusted to tissue equivalent values through the addition of titanium dioxide powder. This does not significantly alter their measured x-ray attenuation coefficient. Whilst published literature on the mechanical properties of breast tissue under compression is very limited a firm argument that these gels possess similar properties has been presented through careful observation and comparison to pork tissue. The stiffness of these gels can be varied tenfold in order to accurately mimic the properties of both healthy and cancerous tissues.

The availability of the phantom material developed leads to numerous opportunities for further work. In the future phantoms made from this material should be developed to give a better understanding of the tissue deformation that occurs during compression and to aid the registration of optical and x-ray images. Phantoms containing compressible fluid filled regions, filled with optically blood equivalent dyes, could be used to assess the potential of dynamic optical imaging. This will largely depend upon the sensitivity of optical tomography to changes in blood flow, volume and oxygenation. As well as developing dynamic phantoms, entirely gel based phantoms would also be useful when displacement of blood did not need to be mimicked. These would contain a region of gel with 'cancerous' properties, embedded in a much larger volume of gel with optical properties equivalent to those of 'healthy' tissue. A further possibility is the incorporation of a layer of material that would give radiographs of the gels a less homogeneous, and therefore more realistic, structural appearance.

Chapter Five

Summary of key contributions and suggestions for further work

5.1. Key contributions made to field

Three pieces of work relevant to the development of a combined x-ray and optical system have been presented. All of these were concerned with the characterisation or assessment of image quality. The key contributions made by this thesis are now summarised.

5.1.1. Investigating the effects of slot scanning on spatial resolution in radiography

Advances in digital radiography have led to a number of advanced acquisition techniques. A number of systems now rely upon scanning one or more relatively small sensors, and aligning the images obtained, in order to acquire a larger overall image. The I-Imas developed at UCL as well as commercially available systems such as the SenoScan® by Fischer operate in this manner. In this thesis the effects of scanned acquisition on spatial resolution were considered using the I-Imas. Whilst the resolution of overall scanned images was found to be slightly poorer than that of their constituent images these effects were small. With careful engineering and image alignment there is no reason that these effects should prevent the use of scanned imaging systems.

5.1.2. Optimisation of illumination in optical imaging

In this thesis it was argued that a dual modality system would necessitate any optical acquisition being made in the parallel plate transmission geometry. Furthermore it was suggested that acquiring purely intensity based, as opposed to temporal, measurements would allow faster acquisition. As such the feasibility of detecting regions of heterogenous absorption, using intensity data acquired in the parallel plate geometry, was investigated. It was demonstrated, using experimentally acquired data, that the positions

of absorbing heterogeneities could successfully be found by processing the data in order to obtain ‘profiles’. More importantly it was shown that the accuracy of the profiles obtained was dependent upon the way in which source power was distributed amongst the available optodes. Optimal source patterns designed to maximise the clarity of the profiles obtained can thus be found.

5.1.3. Development of a compressible dual-modality phantom material

In order to evaluate the potential of combined x-ray and optical mammography, as well as dynamic imaging techniques, compressible phantoms with x-ray and optical properties equivalent to breast tissue will be required. A phantom material with mechanical, x-ray and optical properties simultaneously equivalent to breast tissue has been developed. This material is a solid, yet elastically compressible, gel produced by freezing and thawing a solution of PVAL in ethanol and water. The x-ray attenuation of these gels, at mammographic energies, is already very similar to that of healthy breast tissue. This could be increased to mimic cancerous tissue through addition of a heavy metal salt. The Young’s modulus of the gels increases with PVAL concentration and it can be adjusted to be equivalent to either healthy or stiffer cancerous tissue. The optical absorption and transport scatter coefficients can be adjusted over a wide range of values through the addition of small quantities of near infra-red dye and titanium dioxide powder respectively. Having been characterised, this material is now available for use in the production of a diverse range of phantoms.

5.2. Future work

Whilst it appears promising much work remains to fully assess the potential of dual-modality breast screening. If this was deemed clinically viable then yet more work would be needed to develop a clinically acceptable system. Nonetheless several possibilities for future work arise directly from the work presented in this thesis.

Both the I-Imas and the optimisation of optical source illumination relied upon the use of preliminary information gained by means of an initial ‘scout’ scan. In both cases this scout scan was performed using the same modality. It would be interesting to investigate the possibility of informing one modality’s acquisition using data from the other. Imagine if a region of interest was detected during an optical acquisition made whilst the

breast was being compressed or held under compression. In such a situation it is possible that the x-ray exposure of this area could be increased. Similarly it is possible that a region of interest identified in the x-ray could be used to inform the optical acquisition. It is possible that such an approach would help to increase the visibility and detection of lesions. A lesion with very low radiographic contrast could have a significant optical contrast and this would cause optimisation of the x-ray acquisition. The chance of visualising the lesion in the x-ray would thus be maximised. The potential of this technique would initially need to be investigated through proof of concept work performed on an appropriately designed dual-modality phantom.

A dual-modality system would almost certainly require the optical acquisition to be performed in the parallel plate geometry as this would aid image registration. This is the geometry employed by Boas' system in which the optical interface plates are detached from the compression plates for the duration of the x-ray acquisition (§1.8.1). In this way the interface plates do not interfere with the x-ray acquisition. In a clinical system detaching the plates in this manner would be too time consuming. Whilst the interface plates could be motorised so as to slide outside of the field of view for the x-ray acquisition this might prevent the continuous monitoring of the tissue dynamics as has been proposed to increase lesion contrast (§1.8.2.4). Ideally the interface plates would be very low attenuating and digitally subtracted from the final mammogram. This would require polymer, as opposed to more attenuating glass, fibres to be used. These would have to be oriented parallel to, and ideally embedded within, a very thin interface plate so as to present a minimal pathlength to the x-rays. Unless it could be demonstrated that the quality of the radiographic image was unaffected then this approach would not be clinically acceptable. Proof of concept work needs to be performed to determine whether this approach is feasible. A relatively simple prototype of the interface plate needs to be designed. This could then be imaged in conjunction with standard mammography phantoms to assess its impact on image quality.

The final suggestion for future work departs from the performance of combined optical and x-ray imaging. Some time ago I gave a presentation to a group of medical physicists and radiologists at the Queen Alexandra Hospital in Portsmouth. It was suggested that the compressible phantom material developed as part of this thesis could be used in the production of needle biopsy phantoms. A collaboration between the radiation physics group at UCL and the group at Portsmouth is now being setup to investigate the

feasibility of this idea. Currently there are relatively few means by which trainee radiologists can practice performing stereotactic needle biopsies and many perform their first ever on a patient. A number of biopsy phantoms made by injecting attenuating powders, in order to simulate microcalcifications, into aubergines (Fischmann and Siegmann 2010, Larrison et al 2006) or dough (Quinn et al 1997) have been proposed. Unfortunately these phantoms are of limited use as they fail to mimic the anatomical shape or mechanical properties of the female breast. A more anatomically realistic phantom containing lesions of Technetium-99m has been developed, for use when teaching sentinel node biopsy, but this did not contain microcalcifications (Keshtgar et al 2005). Though a couple of compressible biopsy phantoms, with a similar x-ray attenuation to breast tissue, have also been produced commercially (Fluke Biomedical, Cleveland USA) it is not clear how mechanically realistic of breast tissue these are. Furthermore these phantoms were also designed for use in ultrasound guided biopsy. As a result the lesions embedded are unrealistically large (upwards of 2 mm in diameter). In order to be realistic a biopsy phantom would need to contain clusters of microcalcifications, as well as larger lesions, that could be subject to biopsy. The phantom material developed in this work, cast into an appropriate mould, would be anatomically and mechanically realistic. In addition there is no reason that clusters, representing microcalcifications, should not be incorporated into these gels. Ideally the phantom would produce a realistic mammogram and methods of incorporating a stromal structure to achieve this also need to be considered. Once an appropriate phantom had been developed this would have to be evaluated through field tests involving a number of qualified radiologists and their students.

Appendix One

Proof of percentage error minimisation

This appendix provides a proof that the function

$$f(L_1, L_2) = \frac{\Delta I}{I} = \frac{\sqrt{a_1 L_1^2 + a_2 L_2^2}}{a_1 L_1 + a_2 L_2} \quad (\text{A1.1})$$

is minimised when $L_1 = L_2$ within the constraints that a_1 , a_2 , L_1 and L_2 are all greater than or equal to zero. As each of these terms represent a physically meaningful (i.e. non-negative) intensity of light these constraints must be true. In the case that any of these terms equal zero f is a constant with no dependence upon the value of L_1 or L_2 . As a result it can be assumed that all of the terms are in fact positive real numbers.

Without loss of generality consider minimising f with respect to L_1 . L_2 is taken to be constant though this can take any positive real value. First local minima within the constraint $0 < L_1 < \infty$ must be found. After this it must be established that lesser minima do not occur at these limiting values.

Firstly the value(s) of L_1 at which the derivative of f with respect to L_1 equals zero are found.

$$\frac{\partial f}{\partial L_1} = \frac{a_1 a_2 (L_1 - L_2) L_2}{(a_1 L_1 + a_2 L_2)^2 \sqrt{a_1 L_1^2 + a_2 L_2^2}} = 0 \quad (\text{A1.2})$$

Solving for L_1 the only solution to the above expression is $L_1 = L_2$. To demonstrate that this represents the location of a local minimum (rather than a maximum) the second derivative with respect to L_1 must be found. Following substitution of L_2 for L_1 (as $L_1 = L_2$ at the point of interest) this is

$$\frac{\partial^2 f}{\partial L_1^2} = \frac{a_1 a_2 L_2^3}{((a_1 + a_2) L_2^2)^{5/2}} \quad (\text{A1.3})$$

Due to the nature of the terms this expression must be positive, demonstrating the presence of a local minimum. All that remains to be shown is that a lesser minimum does not occur at either of the boundary conditions, when $L_1 = 0$ or $\rightarrow \infty$

$$f(L_1 = 0) = \frac{\sqrt{L_2^2 a_2}}{L_2 a_2} = \frac{1}{\sqrt{a_2}} \quad (\text{A1.4})$$

and

$$\lim_{L_1 \rightarrow \infty} (f) = \frac{\sqrt{L_1^2 a_1}}{L_1 a_1} = \frac{1}{\sqrt{a_1}} \quad (\text{A1.5})$$

Both of these values are in general larger than the value obtained when $L_1 = L_2$

$$f(L_1, L_1) = \frac{1}{\sqrt{a_1 + a_2}} \quad (\text{A1.6})$$

Whilst a general proof that this holds for a greater number of sources, i.e. that

$$f(L_1, L_2, \dots, L_n) = \frac{\Delta I}{I} = \frac{\sqrt{\sum_{i=1}^n a_i L_i^2}}{\sum_{i=1}^n a_i L_i} \quad (\text{A1.7})$$

is minimised when $L_1 = L_2 = \dots = L_n$, is not provided this was readily confirmed using Mathematica.

Appendix Two

Generating N random integers whose sum is N

The objective of this work was to randomly select a set of 15 integers, that summed to 15, from all other possible sets. Each integer within the sets was required to take a value between 0 and 15. Importantly the order of the integers was significant. Two different permutations of the same group of integers were considered to represent separate sets.

The obvious solution is to generate all of the possible sets and then select one of these at random. In reality the computing power and storage that would be required to do this makes it impractical if not impossible. One approach would be to populate the elements of a 15 dimensional matrix, each dimension having a length of 16 elements (co-ordinates 0 to 15). Each element could be set to 1 if the sum of its co-ordinates was equal to 15 and 0 if not. Selecting a random element of the matrix, out of those with value 1, and taking its coordinates would generate a randomly selected set of integers as required. However this matrix has 15^{16} elements and is far too large to compute.

Pre-calculating each element of such a matrix could be avoided by defining the order in which elements would be stepped through and then randomly selecting a number between 1 and 15^{16} . The corresponding element could then be found and tested to see whether or not its value should be 1. This is still incredibly inefficient. From the work described below it can be shown that 77558760 of the 15^{16} elements would have co-ordinates summing to 15. As such the probability of selecting a satisfactory element is

$$\frac{77558760}{15^{16}} \approx 1.2 \times 10^{-11} \quad (\text{A2.1})$$

To overcome these problems a different approach had to be taken. Firstly all possible combinations were found, irrespective of their order. This can readily be achieved in Mathematica by finding all possible vectors A for which

$$\sum_{n=1}^{15} n \times A_n = 15 \quad (\text{A2.2})$$

where A_n denotes the n^{th} element of A. As an example A_5 will be equal to the number of fives within the combination. The number of zeros, N_{zeros} , included in the combination can be calculated retrospectively as

$$N_{\text{zeros}} = 15 - \sum_{n=1}^{15} A_n \quad (\text{A2.3})$$

Having found all possible combinations these were loaded into Matlab and the number of possible permutations, N_{perm} , for each combination was found. Note that these permutations were not calculated or stored, purely the number that existed. This is found by

$$N_{\text{perm}} = \frac{15!}{N_{\text{zeros}}! A_1! A_2! A_3! \dots A_{15}!} \quad (\text{A2.4})$$

Having found the number of possible permutations for each combination these can be summed together to find the total number of permutations across all combinations. This was found to be 77558760. As such the probability of a given combination occurring can be found - its number of permutations divided by the total number of permutations for all combinations. Once these probabilities have been calculated a combination can be selected at random, but with the chance of selection appropriately weighted by the probability found. Having established the combination to be used a random permutation is calculated. Using this method all possible sets of numbers do not have to be calculated or stored.

As a brief aside it is worth noting that simpler methods initially tested failed. An obvious approach is to randomly select an integer between 0 and 15, say A, and a second between 0 and 15-A, say B. Next calculate a value between 0 and 15-A-B etcetera until 14 numbers have been selected. Select the 15th such that the sum of all 15 numbers is 15. Such an approach does not work as the first few numbers selected tend to add to 15, forcing the remainder to be zeros.

An extreme example. The probability of selecting 15 for the first number, A, is 1/16 at which point all of the remaining numbers are certain to be zeros. The probability of obtaining this set is therefore 1/16. On the other hand the probability of selecting 14 zeros and then a 15, P(0s15), is given by

$$P(0s15) = \left(\frac{1}{16}\right)^{14} \times 1 \approx 1.4 \times 10^{-17} \quad (\text{A2.5})$$

because the probability of selecting zero each time is 1/16 and the final value must then be 15. These two permutations clearly do not have equal probability of occurring as was required.

Appendix Three

Production and characterisation of Pro-jet concentrate

The Pro-jet concentrate was produced by suspending approximately 2 g of Pro-jet (Avecia Inc., USA) in 380 g of MY753 araldite resin (Aeropia Ltd., Crawley). In order to ensure homogeneity the suspension was agitated in an ultrasound bath and stirred regularly for several hours. The exact concentration of Pro-jet used did not matter as the absorption coefficient of the suspension is characterised accurately below. Ideally the concentration should be high enough that the volume of suspension made is sufficient to make a large number of phantoms, yet low enough that the quantity to be added to each phantom is sufficiently large to be accurately measured.

In order to characterise the absorption coefficient of the concentrate six cylindrical polyester resin discs containing different concentrations of the suspension were cast. These were machined down to a thickness of 10 mm and the faces polished with lapping paper to remove any small surface defects. Each sample's average absorbance spectrum was calculated from six separate spectra acquired using a Perkin Elmer UV/Vis spectrometer (Precisely Lambda 25). Each sample was removed from the spectrometer and rotated through 180 degrees between each of the six acquisitions. In this way any variability due to positioning was accounted for. The average spectra were used to find each sample's absorbance at 780 and 815 nm (the two wavelengths utilised by MONSTIR) as well as at 800 nm (approximately halfway between).

Absorbance is given by

$$A = -\log_{10}\left(\frac{I}{I_0}\right) \quad (\text{A3.1})$$

where I is the intensity of light, at a given wavelength, transmitted through the sample and I_0 is the original (unattenuated) intensity as detected in the empty reference arm of the spectrometer. The ratio I_0/I is given by

$$\frac{I_0}{I} = 10^A \quad (\text{A3.2})$$

From this ratio the absorption coefficient of each sample can be calculated, at each wavelength, from the Beer-Lambert law

$$\mu_a = \frac{\ln\left(\frac{I_0}{I}\right)}{d} \quad (\text{A3.3})$$

where d is the optical pathlength. Furthermore

$$\mu_a = \varepsilon C \quad (\text{A3.4})$$

where ε is the extinction coefficient and C is the concentration of absorber (Pro-jet suspension). Figure A3.1 shows the plots of μ_a versus C at each of the three wavelengths. The gradients of these plots are equal to the extinction coefficients of the suspension at the different wavelengths. Least-squares fitting found these to be approximately 18, 21 and 28 mm^{-1} at 780, 800 and 815 nm respectively. The extinction coefficient is equal to the absorption coefficient of the undiluted concentrate. Though the absorption coefficient of the concentrate increases with wavelength its concentration within phantoms is sufficiently small that their absorption coefficient will be very similar regardless of the value assumed for the concentrate. It should be noted that the absorption coefficient of the resin without any dye appears to be significantly greater than zero, though equal at all wavelengths. In fact the absorption coefficient of polyester resin is very low at these wavelengths (Firbank and Delpy 1993). The apparent absorption is likely due to back-reflections from the sample's surface. This represents an offset in absorption that applies equally to all of the samples and thus does not effect the values of the extinction coefficients found.

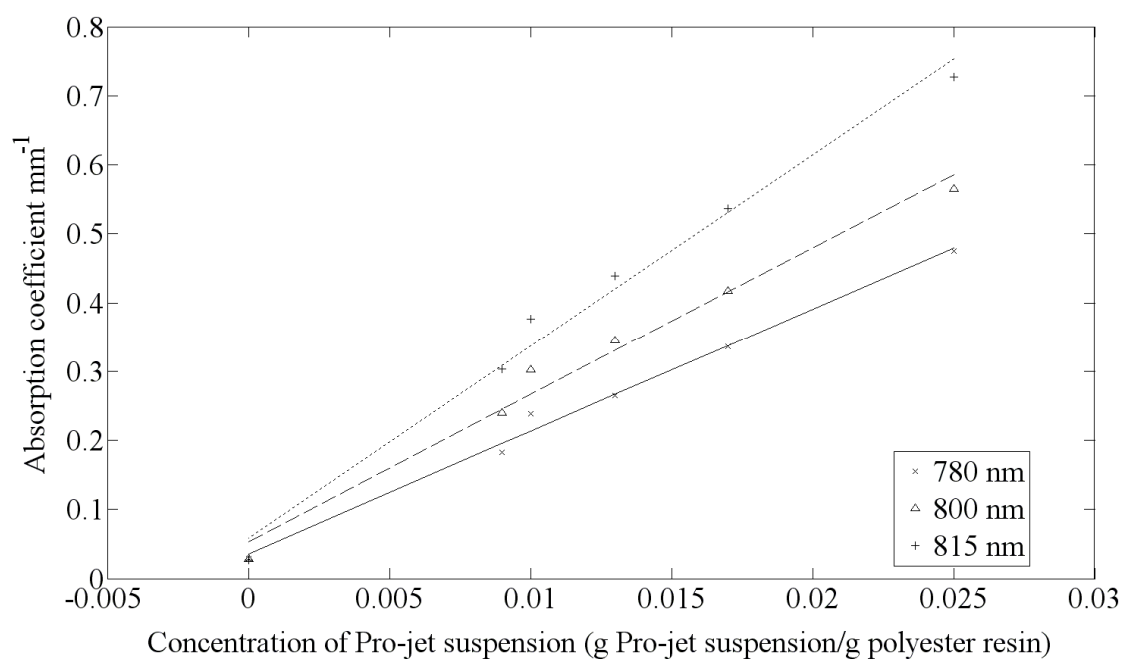


Figure A3.1. The dependence of absorption coefficient upon the concentration of Pro-jet suspension at 780, 800 and 815 nm. Least-squares best fit lines are shown.

References

- Abookasis D, Lay C C, Mathews M S, Linskey M E, Frostig R D and Tromberg B J. 2009. Imaging cortical absorption, scattering, and hemodynamic response during ischemic stroke using spatially modulated near-infrared illumination. *Journal of Biomedical Optics*, **14** (2): 024033(1)-(9)
- Arridge S R and Lionheart W R B. 1998. Nonuniqueness in diffusion-based optical tomography. *Optics Letters*, **23** (11): 882-884
- Azar F S, Metaxas D N and Schnall M D. 2002. Methods for modeling and predicting mechanical deformations of the breast under external perturbations. *Medical Image Analysis*, **6** (1): 1-27
- Banks E, Reeves G, Beral V, Bull D, Crossley B, Simmonds M, Hilton E, Bailey S, Barrett N, Briers P, English R, Jackson A, Kutt E, Lavelle J, Rockall L, Wallis M G, Wilson M and Patnick J. 2004. Influence of personal characteristics of individual women on sensitivity and specificity of mammography in the million women study: cohort study. *British Medical Journal*, **329** (7464): 477-482
- Barbour R. 2006. Electronically modulated dynamic optical phantoms for biomedical imaging. U.S. Pat. WO/2006/135850
- Bassi A, D'Andrea C, Valentini G, Cubeddu R and Arridge S. 2008. Temporal propagation of spatial information in turbid media. *Optics Letters*, **33** (23): 2836-2838
- Bassi A, D'Andrea C, Valentini G, Cubeddu R and Arridge S. 2009. Detection of inhomogeneities in diffusive media using spatially modulated light. *Optics Letters*, **34** (14): 2156-2158
- Beam C A, Conant E F, Sickles E A and Weinstein S P. 2003. Evaluation of prescriptive health care policy implementation in screening mammography. *Radiology*, **229** (2): 534-540

- Bentzen S M. 1983. Evaluation of the spatial resolution of a CT scanner by direct analysis of the edge response function. *Medical Physics*, **10** (5): 579-581
- Beral V, Cush S, Ellis I O, Emery J, Faulkner K, Given-Wilson R, Law M, Loughlin J, Michell M J, Moss S M, Noblet M, Patnick J, Reed M, Rubin C, Toward K and Winstone D. 2006. Screening for breast cancer in England: past and future. Sheffield: NHS cancer screening programmes. Publication number 61
- Berger M J, Hubbell J H, Seltzer S M, Chang J, Coursey J S, Sukumar R, and Zucker D S. 2009. XCOM: Photon Cross Sections Database (Version 1.4). [Online] Available: <http://physics.nist.gov/xcom>. National Institute of Standards and Technology, Gaithersburg, MD
- Besson G M, Koch A, Tesic M, Sottoriva R, Prieur-Drevron P, Munier B, Calais E and DeGroot P. 2002. Design and evaluation of a slot-scanning full-field digital mammography system. *Proceedings of SPIE. Medical Imaging 2002: Physics of Medical Imaging*, **4682**: 457-468
- Boas D A, Brooks D H, Miller E L, DiMarzio C A, Kilmer M, Gaudette R J and Zhang Q. 2001. Imaging the body with diffuse optical tomography. *IEEE Signal Processing Magazine*, **18** (6): 57-75
- Bolotin H H, Sievänen H, Grashuis J L, Kuiper J W and Järvinen T L N. 2001. Inaccuracies inherent in patient-specific dual-energy x-ray absorptiometry bone mineral density measurements: comprehensive phantom-based evaluation. *Journal of Bone and Mineral Research*, **16** (2): 417-426
- Boone J M, Nelson T R, Lindfors K K and Seibert J A. 2001. Dedicated breast CT: radiation dose and image quality evaluation. *Radiology*, **221**: 657-667
- Boone J M and Seibert J A. 1994. An analytical edge spread function model for computer fitting and subsequent calculation of the LSF and MTF. *Medical Physics*, **21** (10): 1541-1545
- Boverman G, Fang Q, Carp S A, Miller E L, Brooks D H, Selb J, Moore R H, Kopans D B and Boas D A. 2007. Spatio-temporal imaging of the hemoglobin in the compressed

breast with diffuse optical tomography. *Physics in Medicine and Biology*, **52** (12): 3619-3641

Buhr E, Gunther-Kohfahl S and Neitzel U. 2003. Accuracy of a simple method for deriving the presampled modulation transfer function of a digital radiographic system from an edge image. *Medical Physics*, **30** (9): 2323-2331

Burnside E, Belkora J and Esserman L. 2001. The impact of alternative practices on the cost and quality of mammographic screening in the United States. *Clinical Breast Cancer*, **2** (2): 145-152

Carney P A, Miglioretti D L, Yankaskas B C, Kerlikowske K, Rosenberg R, Rutter C, Geller B M, Abraham L A, Taplin S H, Digan M, Cutter G and Ballard-Barbash R. 2003. Individual and combined effects of age, breast density, and hormone replacement therapy use on the accuracy of screening mammography. *Annals of Internal Medicine*, **138** (3): 168-175

Carp S A, Kauffman T, Fang Q, Rafferty E, Moore R, Kopans D and Boas D. 2006. Compression-induced changes in the physiological state of the breast as observed through frequency domain photon migration measurements. *Journal of Biomedical Optics*, **11** (6): 064016(1)-(6)

Cerussi A E, Berger A J, Bevilacqua F, Shah N, Jakubowski D, Butler J, Holcombe R F and Tromberg B J. 2001. Sources of absorption and scattering contrast for near-infrared optical mammography. *Academic Radiology*, **8** (3): 211-218

Chapman J D, Engelhardt E L, Stobbe C C, Schneider R F and Hanks G E. 1998. Measuring hypoxia and predicting tumour radioresistance with nuclear medicine assays. *Radiotherapy and Oncology*, **46** (3): 229-237

Cheney M, Isaacson D and Newell J C. 1999. Electrical impedance tomography. *SIAM Review*, **41** (1): 85-101

Chernomordik V, Hattery D W, Grosenick D, Wabnitz H, Rinneberg H, Moesta K T, Schlag P M and Gandjbakhche A. 2002. Quantification of optical properties of a breast tumour using random walk theory. *Journal of Biomedical Optics*, **7** (1): 80-87

- Choe R, Konecky S D, Corlu A, Lee K, Durduran T, Busch D R, Pathak S, Czerniecki B J, Tchou J, Fraker D L, DeMichele A, Chance B, Arridge S R, Schweiger M, Culver J P, Schnall M D, Putt M E, Rosen M A and Yodh A G. 2009. Differentiation of benign and malignant breast tumors by in-vivo three-dimensional parallel-plate diffuse optical tomography. *Journal of Biomedical Optics*, **14** (2): 024020(1)-(18)
- Chu K C, Jordan K J, Battista J J, Van Dyk J and Rutt B K. 2000. Polyvinyl alcohol-Fricke hydrogel and cryogel: two new gel dosimetry systems with low Fe^{3+} diffusion. *Physics in Medicine and Biology*, **45** (4): 955-969
- Clarke E D and Mortimer T H. 1919. The determination of the freezing-point curves and densities of denatured alcohol-water mixtures. *The Journal of Industrial and Engineering Chemistry*, **11** (5): 443-48
- Cooper R J, Everdell N L, Enfield L C, Gibson A P, Worley A and Hebden J C. 2009. Design and evaluation of a probe for simultaneous EEG and near-infrared imaging of cortical activation. *Physics in Medicine and Biology*, **54**: 2093-2102
- Cope M. 1991. The application of near infrared spectroscopy to non invasive monitoring of cerebral oxygenation in the newborn infant. PhD Thesis, University College London, UK
- Cuccia D J, Bevilacqua F, Durkin A J, Ayers F R and Tromberg B J. 2009. Quantitation and mapping of tissue optical properties using modulated imaging. *Journal of Biomedical Optics*, **14** (2): 024012(1)-(13)
- Cuccia D J, Bevilacqua F, Durkin A J and Tromberg B J. 2005. Modulated imaging: quantitative analysis and tomography of turbid media in the spatial-frequency domain. *Optics Letters*, **30** (11): 1354-1356
- Culver J P, Ntziachristos V, Holboke M J and Yodh A G. 2001. Optimization of optode arrangements for diffuse optical tomography: A singular-value analysis. *Optics Letters*, **26** (10): 701-703

- Cunningham I A and Reid B K. 1992. Signal and noise in modulation transfer function determinations using the slit, wire and edge techniques. *Medical Physics*, **19** (4): 1037-1044
- Cunningham I A and Fenster A. 1987. A method for modulation transfer function determination from edge profiles with correction for finite-element differentiation. *Medical Physics*, **14** (4): 533-537
- Cush S, Burch A, Whelehan P and Young K. 2007. Routine quality control tests for full field digital mammography systems. Sheffield: NHS Cancer Screening Programmes. Equipment report 0702
- Cush S, Johnson S, Jones S, Passmore D, Deogun K and Vegnuti Z. 2006. Quality assurance guidelines for mammography including radiographic quality control. Sheffield: NHS cancer screening programmes. Publication number 63
- Cutrone J A, Khalkhali I, Yospur L S, Diggles L, Weinberg I, Pong E M, Tolmos J, Vargas M P and Vargas H I. 1999. Tc-99m Sestamibi Scintimammography for the Evaluation of Breast Masses in Patients with Radiographically Dense Breasts. *The Breast Journal*, **5** (6): 383-388
- D'Andrea C, Bassi A, Valentini G, Cubeddu R and Arridge S. 2009. Structured illumination and time gated detection for diffuse optical imaging. *Proceedings of SPIE. Diffuse Optical Imaging II*, **7369**: 73690Q
- Department of Health. 2007. Cancer Reform Strategy. Report number 283524
- Dobbins J T. 1995. Effects of undersampling on the proper interpretation of modulation transfer function, noise power spectra, and noise equivalent quanta of digital imaging systems. *Medical Physics*, **22** (2): 171-181
- Dobbins J T, Ergun D L, Rutz L, Hinshaw D A, Blume H and Clark D C. 1995. DQE(f) of four generations of computed radiography acquisition devices. *Medical Physics*, **22** (10): 1581-1593

Duffy S W, Tabar L, Chen H, Holmqvist M, Yen M, Abdsalah S, Epstein B, Frodis E, Ljungberg E, Hedborg-Melander C, Sundborn A, Tholin M, Wiege M, Akerlund A, Wu H, Tung T, Chiu Y, Chiu C, Huang C, Smith R A, Rosen M, Stenbeck M and Holmberg L. 2002. The impact of organized mammography service screening on breast carcinoma mortality in seven swedish counties. *Cancer*, **95** (3): 458-469

Durduran T, Choe R, Culver J P, Zubkov L, Holboke M J, Giammarco J, Chance B and Yodh A G. 2002. Bulk optical properties of healthy female breast tissue. *Physics in Medicine and Biology*, **47**: 2847-2861

Elmore J G, Taplin S H, Barlow W E, Cutter G R, D'Orsi C J, Hendrick R E, Abraham L A, Fosse J S and Carney P A. 2005. Does litigation influence medical practice? The influence of community radiologists' medical malpractice perceptions and experience on screening mammography. *Radiology*, **236** (1): 37-46

Elwood M, McNoe B, Smith T, Bandaranayake M and Doyle T C. 1998. Once is enough - why some women do not continue to participate in a breast cancer screening programme. *The New Zealand Medical Journal*, **111** (1066): 180-183

Enfield L C, Gibson A P, Everdell N L, Delpy D T, Schweiger M, Arridge S R, Richardson C, Keshtgar M, Douek M and Hebden J C. 2007. Three-dimensional time-resolved optical mammography of the uncompressed breast. *Applied Optics*, **46** (17): 3628-3638

Esbrand C. 2009. Feature analysis methods for intelligent breast imaging parameter optimisation using CMOS active pixel sensors. PhD Thesis, University College London, UK

Esserman L, Cowley H, Eberle C, Kirkpatrick A, Chang S, Berbaum K and Gale A. 2002. Improving the accuracy of mammography: volume and outcome relationships. *Journal of the National Cancer Institute*, **94** (5): 369-375

Evans S M and Koch C J. 2003. Prognostic significance of tumour oxygenation in humans. *Cancer Letters*, **195** (1): 1-16

- Everdell N L, Gibson A P, Tullis I D C, Vaithiananthan T, Hebden J C and Delpy D T. 2005. A frequency multiplexed near-infrared topography system for imaging functional activation in the brain. *Review of Scientific Instruments*, **76**: 093705(1)-(5)
- Fang Q, Carp S A, Selb J, Boverman G, Zhang Q, Kopans D B, Moore R H, Miller E L, Brooks D H and Boas D A. 2009. Combined optical imaging and mammography of the healthy breast: optical contrast derived from breast structure and compression. *IEEE Transactions on Medical Imaging*, **28** (1): 30-42
- Fang Q, Carp S A, Selb J, Moore R, Kopans D B, Miller E L, Brooks D H and Boas D A. 2008. Spectrally constrained optical breast imaging with co-registered x-ray tomosynthesis. *OSA Biomedical Optics: Optical imaging of breast cancer*, Paper BSub2
- Fantini S, Walker S A, Franceschini M A, Kaschke M, Schlag P M and Moesta K T. 1998. Assessment of the size, position, and optical properties of breast tumors *in vivo* by noninvasive optical methods. *Applied Optics*, **37** (10): 1982-1989
- Fatemi M, Manduca A and Greenleaf J F. 2003. Imaging elastic properties of biological tissues by low-frequency harmonic vibration. *Proceedings of the IEEE*, **91** (10): 1503-1519
- Faulkner K and Law J. 1994. A comparison of mammographic phantoms. *British Journal of Radiology*, **67**: 174-180
- Fetterly K A, Hangiandreou N J, Schueler B A and Ritenour E R. 2002. Measurement of the presampled two-dimensional modulation transfer function of digital imaging systems. *Medical Physics*, **29** (5): 913-921
- Firbank M and Delpy D T. 1993. A design for a stable and reproducible phantom for use in near infra-red imaging and spectroscopy. *Physics in Medicine and Biology*, **38**: 847-853
- Firbank M, Oda M and Delpy D T. 1995. An improved design for a stable and reproducible phantom material for use in near-infrared spectroscopy and imaging. *Physics in Medicine and Biology*, **40**: 955-961

Fischmann A and Siegmann K C. 2010. Low-cost phantoms for training of stereotactic vacuum-assisted biopsy of the breast. *Clinical Imaging*, **34** (2): 97-99

Forrest P. 1986. Breast cancer screening. London: Her Majesty's Stationery Office.

Franceschini M A, Moesta K T, Fantini S, Gaida G, Gratton E, Jess H, Mantulin W W, Seeber M, Schlag P M and Kaschke M. 1997. Frequency-domain techniques enhance optical mammography: Initial clinical results. *Proceedings of the National Academy of Sciences of the United States of America*, **94** (12): 6468-6473

Franceschini M A, Toronov V, Filiaci M E, Gratton E and Fantini S. 2000. On-line optical imaging of the human brain with 160-ms temporal resolution. *Optics Express*, **6** (3): 49-57

Fujita H, Tsai D-Y, Itoh T, Doi K, Morishita J, Ueda K and Ohtsuka A. 1992. A simple method for determining the modulation transfer function in digital radiography. *IEEE Transactions on Medical Imaging*, **11** (1): 34-39

Gibson A P, Austin T, Everdell N L, Schweiger M, Arridge S R, Meek J H, Wyatt J S, Delpy D T and Hebden J C. 2006. Three-dimensional whole-head optical tomography of passive motor evoked responses in the neonate. *Neuroimage*, **30** (2): 521-528

Gibson A P, Hebden J C and Arridge S R. 2005. Recent advances in diffuse optical imaging. *Physics in Medicine and Biology*, **50** (4): R1-R43

Gisser D G, Isaacson D and Newell J C. 1988. Theory and performance of an adaptive current tomography system. *Clinical Physics and Physiological Measurement*, **9** (Supplement A): 35-41

Greenleaf J F, Fatemi M and Insana M. 2003. Selected methods for imaging elastic properties of biological tissues. *Annual Review of Biomedical Engineering*, **5**: 57-78

Greer P B and van Doorn T. 2000. Evaluation of an algorithm for the assesment of the MTF using an edge method. *Medical Physics*, **27** (9): 2048-2059

Griffiths J A, Metaxas M G, Pani S, Schulerud H, Esbrand C, Royle G J, Price B D, Rokvic T, Longo R, Asimidis A, Bletsas E, Cavouras D, Fant A, Gasiorek P, Georgiou H,

Hall G, Jones J, Leaver J, Li G, Machin D, Manthos N, Matheson J, Noy M, Ostby J M, Psomadellis F, van der Stelt P F, Theodoridis S, Triantis F, Turchetta R, Venanzi C and Speller R D. 2008. Preliminary images from an adaptive imaging system. *Physica Medica*, **24**: 117-121

Griffiths J A, Metaxas M G, Royle G J, Venanzi C, Esbrand C, van der Stelt P F, Verheij H, Li G, Turchetta R, Fant A, Gasiorsek P, Theodoridis S, Georgiou H, Cavouras D, Hall G, Noy M, Jones J, Leaver J, Machin D, Greenwood S, Khaleeq M, Schulerud H, Ostby J M, Triantis F, Asimidis A, Bolanakis D, Manthos N, Longo R, Bergamaschi A and Speller R D. 2006. A multi-element detector system for intelligent imaging: I-Imas. *IEEE Nuclear science symposium conference record*, **4**: 2554-2558.

Grosenick D, Moesta K T, Wabnitz H, Mucke J, Stroszczynski C, Macdonald R, Schlag P M and Rinneberg H. 2003. Time-domain optical mammography: Initial clinical results on detection and characterization of breast tumours. *Applied Optics*, **42** (16): 3170-3186

Grosenick D, Wabnitz H, Moesta K T, Mucke J, Schlag P M and Rinneberg H. 2005. Time-domain scanning optical mammography: II. Optical properties and tissue parameters of 87 carcinomas. *Physics in Medicine and Biology*, **50** (11): 2451-2468

Grosenick D, Wabnitz H, Rinneberg H H, Moesta K T and Schlag P M. 1999. Development of a time-domain optical mammograph and first in vivo applications. *Applied Optics*, **38** (13): 2927-2943

Guo Y, Sivaramakrishna R, Lu C, Suri J S and Laxminarayan S. 2006. Breast image registration techniques: a survey. *Medical and Biological Engineering and Computing*, **44**: 15-26

Gupta A K, Hutchinson P J, Fryer T, Al-Rawi P G, Parry D A, Minhas P S, Kett-White R, Kirkpatrick P J, Mathews J C, Downey S, Aigbirhio F, Clark J, Pickard J D and Menon D K. 2002. Measurement of brain tissue oxygenation performed using positron emission tomography scanning to validate a novel monitoring method. *Journal of Neurosurgery*, **96** (2): 263-268

Harrison L and Blackwell K. 2004. Hypoxia and anemia: factors in decreased sensitivity to radiation therapy and chemotherapy? *The Oncologist*, **9** (Supplement 5): 31-40

Hebden J C. 2009. *Personal Communication*. University College London, UK

Hebden J C, Brunner J, Correia T, Price B D, Gibson A P and Everdell N L. 2008. An electrically-activated dynamic tissue-equivalent phantom for assesment of diffuse optical imaging systems. *Physics in Medicine and Biology*, **53** (2): 329-337

Hebden J C, Gibson A, Austin T, Yusof R M, Everdell N, Delpy D T, Arridge S R, Meek J H and Wyatt J S. 2004. Imaging changes in blood volume and oxygenation in the newborn infant brain using three-dimensional optical tomography. *Physics in Medicine and Biology*, **49** (7): 1117-1130

Hebden J C, Price B D, Gibson A P and Royle G. 2006. A soft deformable tissue-equivalent phantom for diffuse optical tomography. *Physics in Medicine and Biology*, **51** (21): 5581-5590

Heywang-Kobrunner S H, Viehweg P, Heinig A and Kuchler C. 1997. Contrast-enhanced MRI of the breast: accuracy, value, controversies, solutions. *European Journal of Radiology*, **24** (2): 94-108

Hipwell J H, Tanner C, Crum W R, Schnabel J A and Hawkes D J. 2007. A new validation method for x-ray mammogram registration algorithms using a projection model of breast x-ray compression. *IEEE Transactions on Medical Imaging*, **26** (9): 1190-1200

Hyon S, Cha W and Ikada Y. 1989. Preparation of transparent poly(vinyl alcohol) hydrogel. *Polymer Bulletin*, **22** (2): 119-122

Hyon S and Ikada Y. 1987. Biomaterials Universe Inc., Osaka Japan. Porous and transparent poly(vinyl alcohol) gel and method of manufacturing the same. U.S. Pat. 4,663,358

Isobe K, Kusaka T, Nagano K, Okubo K, Yasuda S, Kondo M, Itoh S and Onishi S. 2001. Functional imaging of the brain in sedated newborn infants using near infrared topography during passive knee movement. *Neuroscience Letters*, **299** (3): 221-224

Jennions D.K. 2008. Time-resolved optical tomography instrumentation for fast 3D functional imaging. PhD Thesis, University College London, UK

- Jiang S, Pogue B W, Carpenter C M, Kaufman P and Paulsen K D. 2010. Near-infrared spectral tomography system for measuring dynamic vascular changes in breast. *OSA Biomedical Optics: Breast Cancer Imaging and Monitoring*, Paper BSub6
- Jiang S, Pogue B W, Laughney A M, Kogel C A and Paulsen K D. 2009. Measurement of pressure-displacement kinetics of hemoglobin in normal breast tissue with near-infrared spectral imaging. *Applied Optics*, **48** (10): D130-D136
- Jiang S, Pogue B W, McBride T O and Paulsen K D. 2003a. Quantitative analysis of near-infrared tomography: sensitivity to the tissue simulating precalibration phantom. *Journal of Biomedical Optics*, **8** (2): 308-315
- Jiang S, Pogue B W, Paulsen K D, Kogel C and Poplack S P. 2003b. In vivo near-infrared spectral detection of pressure-induced changes in breast tissue. *Optics Letters*, **28** (14): 1212-1214
- Johns P C and Yaffe M J. 1987. X-ray characterisation of normal and neoplastic breast tissues. *Physics in Medicine and Biology*, **32** (6): 675-695
- Jones A K, Hintenlang D E and Bolch W E. 2003. Tissue-equivalent materials for construction of tomographic dosimetry phantoms in pediatric radiology. *Medical Physics*, **30** (8): 2072-2081
- Kellner A L, Nelson T R, Cervino L I and Boone J M. 2007. Simulation of mechanical compression of breast tissue. *IEEE Transactions on Biomedical Engineering*, **54** (10): 1885-1891
- Keshtgar M R S, Chicken D W, Waddington W A, Raven W and Ell P J. 2005. A training simulator for sentinel node biopsy in breast cancer: a new standard. *European Journal of Surgical Oncology*, **31** (2): 134-140
- Kirkby D.R. 1999. A picosecond optoelectronic cross correlator using a gain modulated avalanche photodiode for measuring the impulse response of tissue. PhD Thesis, University College London, UK

- Krohn K A, Link J M and Mason R P. 2008. Molecular imaging of hypoxia. *The Journal of Nuclear Medicine*, **49** (6): 129S-148S
- Krouskop T A, Wheeler T M, Kallel F, Garra B S and Hall T. 1998. Elastic moduli of breast and prostate tissues under compression. *Ultrasonic Imaging*, **20** (4): 260-274
- Kruse S A, Smith J A, Lawrence A J, Dresner M A, Manduca A, Greenleaf J F and Ehman R L. 2000. Tissue characterization using magnetic resonance elastography: preliminary results. *Physics in Medicine and Biology*, **45** (6): 1579-1590
- Lai C, Shaw C C, Geiser W, Kappadath S C, Liu X, Wang T, Tu S and Altunbus M C. 2004. Slot scanning versus anti-scatter grid in digital mammography - comparison of low contrast performance using contrast-detail measurement. *Proceedings of SPIE. Medical Imaging 2004: Physics of Medical Imaging*, **5368**: 734-742
- Larrison M, DiBona A and Hogg D E. 2006. Low-cost phantom for stereotactic breast biopsy training. *American Journal of Roentgenology*, **187**: 972-974
- Lawinski C P and Dunne J. 2003. Guidance on the electrical and mechanical safety testing of mammographic x-ray equipment. Sheffield: NHS Cancer Screening Programme. Report 03/01
- Leff D R, Warren O J, Enfield L C, Gibson A, Athanasiou T, Patten D K, Hebden J, Yang G Z and Darzi A. 2008. Diffuse optical imaging of the healthy and diseased breast: A systematic review. *Breast Cancer Research and Treatment*, **108**: 9-22
- Li A, Miller E L, Kilmer M E, Brukilacchio T J, Chaves T, Stott J, Zhang Q, Wu T, Chorlton M, Moore R H, Kopans D B and Boas D A. 2003. Tomographic optical breast imaging guided by three-dimensional mammography. *Applied Optics*, **42** (25): 5181-5190
- Matcher S J, Cope M and Delpy D T. 1997. *In vivo* measurements of the wavelength dependence of tissue-scattering coefficients between 760 and 900 nm measured with time-resolved spectroscopy. *Applied Optics*, **36** (1): 386-396
- McBride T O, Pogue B W, Gerety E D, Poplack S B, Osterberg U L and Paulsen K D. 1999. Spectroscopic diffuse optical tomography for the quantitative assessment of

hemoglobin concentration and oxygen saturation in breast tissue. *Applied Optics*, **38** (25): 5480-5490

McKnight A L, Kugel J L, Rossman P J, Manduca A, Hartmann L C and Ehman R L. 2002. MR elastography of breast cancer: preliminary results. *American Journal of Roentgenology*, **178** (6): 1411-1417

McRobbie D.W., Moore E.A., Graves M.J. and Prince M.R. 2007. MRI from picture to proton. 2nd Edition. Cambridge: Cambridge University Press

Miller D, Livingstone V and Herbison G P. 2008. Interventions for relieving the pain and discomfort of screening mammography (review). *Cochrane Database of Systematic Reviews*, (Issue 1)

Neitzel U, Buhr E, Hilgers G and Granfors P. 2004. Determination of modulation transfer function using the edge method: Influence of scattered radiation. *Medical Physics*, **31** (12): 3485-3491

Niklason L T, Christian B T, Niklason L E, Kopans D B, Castleberry D E, Opsahl-Ong B H, Landberg C E, Slanetz P J, Giardino A A, Moore R, Albagli D, DeJule M C, Fitzgerald P F, Fobare D F, Giambattista B W, Kwasnick R F, Liu J, Lubowski S J, Possin G E, Richotte J F, Wei C and Wirth R F. 1997. Digital tomosynthesis in breast imaging. *Radiology*, **205**: 399-406

Nissilä I, Hebden J C, Jennions D, Heino J, Schweiger M, Kotilahti K, Noponen T, Gibson A, Järvenpää S, Lipiäinen L and Katila T. 2006. Comparison between a time-domain and a frequency-domain system for optical tomography. *Journal of Biomedical Optics*, **11** (6): 064015(1)-(18)

Olivo A, Rigon L, Arfelli F, Cantatore G, Longo R, Menk R H, Pani S, Prest M, Poropat P, Tromba G, Vallazza E and Castelli E. 2000. Experimental evaluation of a simple algorithm to enhance the spatial resolution in scanned radiographic systems. *Medical Physics*, **27** (11): 2609-2616

Olivo A and Speller R. 2007. Modelling of a novel x-ray phase contrast imaging technique based on coded apertures. *Physics in Medicine and Biology*, **52** (22): 6555-6573

Ophir J, Alam S K, Garra B, Kallel F, Konofagou E, Krouskop T and Varghese T. 1999. Elastography: ultrasonic estimation and imaging of the elastic properties of tissues. *Proceedings of the Institution of Mechanical Engineers, Part H: Journal of Engineering in Medicine*, **213** (3): 203-233

Pathmanathan P, Gavaghan D, Whiteley J, Brady M, Nash M, Nielsen P and Rajagopal V. 2004. Predicting tumour location by simulating large deformations of the breast using a 3D finite element model and nonlinear elasticity. *Proceedings of Miccai 2004: Medical Image Computing and Computer-Assisted Intervention*, **3217**: 217-224

Patnick J. 2009. Expanding our reach. NHS Breast Screening Programme annual review 2009. Sheffield: NHS Breast Screening Programme.

Peart O.J. 2005. Mammography and breast imaging: just the facts. The McGraw-Hill Companies Inc

Phillips K, Glendon G and Knight J A. 1999. Putting the risk of breast cancer in perspective. *The New England Journal of Medicine*, **340** (2): 141-144

Pisano E D, Gatsonis C, Hendrick E, Yaffe M, Baum J K, Acharyya S, Conant E F, Fajardo L L, Bassett L, D'Orsi C, Jong R and Rebner M. 2005. Diagnostic performance of digital versus film mammography for breast-cancer screening. *The New England Journal of Medicine*, **353** (17): 1773-1783

Pogue B W, Jiang S, Song X, Srinivasan S, Dehghani H, Paulsen K D, Tosteson T D, Kogel C, Soho S and Poplack S P. 2004. Near-infrared scattering spectrum differences between benign and malignant breast tumors measured in vivo with diffuse tomography. *OSA Biomedical Topical Meeting*, Paper ThB1

Pogue B W and Patterson M S. 2006. Review of tissue simulating phantoms for optical spectroscopy, imaging and dosimetry. *Journal of Biomedical Optics*, **11** (4): 041102(1)-(16)

- Poulos A and McLean D. 2004. The application of breast compression in mammography: a new perspective. *Radiography*, **10** (2): 131-137
- Poulos A, McLean D, Rickard M and Heard R. 2003. Breast compression in mammography: how much is enough? *Australasian Radiology*, **47** (2): 121-126
- Price B D, Esbrand C J, Olivo A, Gibson A P, Hebden J C, Speller R and Royle G J. 2008. Assessing the validity of modulation transfer function evaluation techniques with application to small area and scanned digital detectors. *Review of Scientific Instruments*, **79** (11): 113103(1)-(6)
- Price B D, Gibson A P and Royle G J. 2010a. Dual-modality imaging of a compressible breast phantom with realistic optical and x-ray properties. *Proceedings of SPIE. Medical Imaging 2010: Physics of Medical Imaging*, **7622**: 762207(1)-(8)
- Price B D, Gibson A P, Tan L T and Royle G J. 2010b. An elastically compressible phantom material with mechanical and x-ray attenuation properties equivalent to breast tissue. *Physics in Medicine and Biology*, **55** (4): 1177-1188
- Quinn A D, Smiddy P F, Duggan M, Murphy J and Molloy M. 1997. Technical report: a training phantom for stereotactic breast biopsies. *Clinical Radiology*, **52** (2): 149-150
- Reddy M and Given-Wilson R. 2004. Screening for breast cancer. *Surgery*, **22** (7): 155-160
- Ruiter N V, Stotzka R, Müller T O, Gemmeke H, Reichenbach J R and Kaiser W A. 2006. Model-Based Registration of x-ray mammograms and MR images of the female breast. *IEEE Transactions on Nuclear Science*, **53** (1): 204-211
- Samani A, Zubovits J and Plewes D. 2007. Elastic moduli of normal and pathological human breast tissues: an inversion-technique-based investigation of 169 samples. *Physics in Medicine and Biology*, **52** (6): 1565-1576
- Samei E, Buhr E, Granfors P, Vandenbroucke D and Wang X. 2005. Comparison of edge analysis techniques for the determination of the MTF of digital radiographic systems. *Physics in Medicine and Biology*, **50** (15): 3613-3625

Samei E, Ranger N T, Dobbins J T and Chen Y. 2006. Intercomparison of methods for image quality characterization. I. Modulation transfer function. *Medical Physics*, **33** (5): 1454-1465

Samei E, Flynn M J and Reimann D A. 1998. A method for measuring the presampled MTF of digital radiographic systems using an edge test device. *Medical Physics*, **25** (1): 102-113

Sarntinoranont M, Rooney F and Ferrari M. 2003. Interstitial stress and fluid pressure within a growing tumour. *Annals of Biomedical Engineering*, **31** (3): 327-335

Sarvazyan A, Goukassian E, Maevsky G, Oranskaja, Skovoroda A, Emelianov S, Klishko A, Mironova G, Sholokhov V and Ermilova V. 1994. Elasticity imaging as a new modality of medical imaging for cancer detection. *Proc.Int.Workshop on Interaction of Ultrasound with Biological Media*. 69-81

Schmidt F E W, Fry M E, Hillman E M C, Hebden J C and Delpy D T. 2000. A 32-channel time-resolved instrument for medical optical tomography. *Review of Scientific Instruments*, **71** (1): 256-265

Schmitz C H, Klemer D P, Hardin R, Katz M S, Pei Y, Graber H L, Levin M B, Levina R D, Franco N A, Solomon W B and Barbour R L. 2005. Design and implementation of dynamic near-infrared optical tomographic imaging instrumentation for simultaneous dual-breast measurements. *Applied Optics*, **44** (11): 2140-2153

Schmitz C H, Locker M, Lasker J M, Hielscher A H and Barbour R L. 2002. Instrumentation for fast functional optical tomography. *Review of Scientific Instruments*, **73** (2): 429-439

Schulerud H, Thielemann J, Kirkhus T, Kaspersen K, Ostby J M, Metaxas M G, Royle G J, Griffiths J, Cooke E, Esbrand C, Pani S, Venanzi C, van der Stelt P F, Li G, Turchetta R, Fant A, Theodoridis S, Georgiou H, Hall G, Noy M, Jones J, Leaver J, Triantis F, Asimidis A, Manthos N, Longo R, Bergamaschi A and Speller R D. 2007. Adaptive image content-based exposure control for scanning applications in radiography. *Advanced concepts for intelligent vision systems*, **4678**: 543-552.

- Scopinaro F and Massa R. 2003. Role and perspectives of scintimammography. *Nuclear Instruments and Methods in Physics Research Section A*, **497** (1): 14-20
- Serdaroglu A, Yazici B and Kwon K. 2006. Optimum source design for detection of heterogeneities in diffuse optical imaging. *Proceedings of SPIE. Optical methods for tumor treatment and detection: mechanisms and techniques in photodynamic therapy XV*, **6139**: 61391A(1)-(11)
- Sinkus R, Lorenzen J, Schrader D, Lorenzen M, Dargatz M and Holz D. 2000. High-resolution tensor MR elastography for breast tumour detection. *Physics in Medicine and Biology*, **45** (6): 1649-1664
- Sinkus R, Tanter M, Catheline S, Lorenzen J, Kuhl C, Sondermann E and Fink M. 2005. Imaging anisotropic and viscous properties of breast tissue by magnetic resonance-elastography. *Magnetic Resonance in Medicine*, **53** (2): 372-387
- Sullivan D C, Beam C A, Goodman S M and Watt D L. 1991. Measurement of force applied during mammography. *Radiology*, **181** (2): 355-357
- Suzuki K, Yamashita Y, Ohta K, Kaneko M, Yoshida M and Chance B. 1996. Quantitative measurement of optical parameters in normal breasts using time-resolved spectroscopy: In vivo results of 30 Japanese women. *Journal of Biomedical Optics*, **1** (3): 330-334
- Taroni P, Torricelli A, Spinelli L, Pifferi A, Arpaia F, Danesini G and Cubeddu R. 2005. Time-resolved optical mammography between 637 and 985nm: clinical study on the detection and identification of breast lesions. *Physics in Medicine and Biology*, **50** (11): 2469-2488
- Trefethen L.N. and Bau D. 1997. Numerical linear algebra. Philadelphia: Society for Industrial and Applied Mathematics
- Tucker D M, Barnes G T and Wu X. 1991. Molybdenum target x-ray spectra: A semiempirical model. *Medical Physics*, **18** (3): 402-07

- Van Houten E E W, Doyley M M, Kennedy F E, Weaver J B and Paulsen K D. 2003. Initial in-vivo experience with steady-state subzone based MR elastography of the human breast. *Journal of Magnetic Resonance Imaging*, **17** (1): 72-85
- van Veen R L P, Sterenborg H J C M, Marinelli A W K S and Menke-Pluymers M. 2004. Intraoperatively assessed optical properties of malignant and healthy breast tissue used to determine the optimum wavelength of contrast for optical mammography. *Journal of Biomedical Optics*, **9** (6): 1129-1136
- Vaupel P, Briest S and Hockel M. 2002. Hypoxia in breast cancer: pathogenesis, characterization and biological/therapeutic implications. *Wiener Medizinische Wochenschrift*, **152** (13-14): 334-342
- Vaupel P and Mayer A. 2007. Hypoxia in cancer: significance and impact on clinical outcome. *Cancer and Metastasis Reviews*, **26** (2): 225-239
- Waldron J. 2010. Breast Screening Programme, England 2008-09. The NHS Information Centre for health and social care.
- Wellman P S, Howe R D, Dalton E and Kern K A. 1999. Breast tissue stiffness in compression is correlated to histological diagnosis. Harvard: Technical Report, Harvard BioRobotics Laboratory, Division of Engineering and Applied Sciences, Harvard University.
- Westlake S and Cooper N. 2008. Cancer incidence and mortality: trends in the United Kingdom and constituent countries, 1993 to 2004. Basingstoke: Palgrave Macmillan.
- White D R, Martin R J and Darlison R. 1977. Epoxy resin based tissue substitutes. *British Journal of Radiology*, **50** (599): 814-821
- Williams C, Clymer B and Schmalbrock P. 1999. Biomechanics of breast tissue: preliminary study of force-deformation relationship. *Proc. Intl. Soc. Magn. Reson. Med.*, **7**: 524-524

- Wolf M, Keel M, Dietz V, von Siebenthal K, Bucher H U and Baenziger O. 1999. The influence of a clear layer on near-infrared spectrophotometry measurements using a liquid neonatal head phantom. *Physics in Medicine and Biology*, **44** (7): 1743-1753
- Wouters B G and Brown J M. 1997. Cells at intermediate oxygen levels can be more important than the "hypoxic fraction" in determining tumour response to fractionated radiotherapy. *Radiation Research*, **147** (5): 541-550
- Wu T, Stewart A, Stanton M, McCauley T, Phillips W, Kopans D B, Moore R H, Eberhard J W, Opsahl-Ong B, Niklason L and Williams M B. 2003. Tomographic mammography using a limited number of low-dose cone-beam projection images. *Medical Physics*, **30** (3): 365-380
- Yamashita Y, Maki A and Koizumi H. 2001. Wavelength dependence of the precision of noninvasive optical measurement of oxy-, deoxy-, and total hemoglobin concentration. *Medical Physics*, **28** (6): 1108-1114
- Yamashita Y, Maki A and Koizumi H. 1999. Measurement system for noninvasive dynamic optical topography. *Journal of Biomedical Optics*, **4** (4): 414-417
- Yates T, Hebden J C, Gibson A, Everdell N, Arridge S R and Douek M. 2005. Optical tomography of the breast using a multi-channel time-resolved imager. *Physics in Medicine and Biology*, **50** (11): 2503-2517
- Zhang Q, Brukilacchio T J, Li A, Stott J J, Chaves T, Hillman E, Wu T, Chorlton M, Rafferty E, Moore R H, Kopans D B and Boas D A. 2005. Coregistered tomographic x-ray and optical breast imaging: initial results. *Journal of Biomedical Optics*, **10** (2): 024033(1)-(9)